Tunable Synthesis of Metal-Rich and Phosphorus-Rich Nickel Phosphides and Their Comparative Evaluation as Hydrogen Evolution Electrocatalysts

Ishanka A. Liyanage, Ashley Flores, Edward G. Gillan*

University of Iowa, Department of Chemistry, Iowa City, Iowa 52242 USA

E-mail: edward-gillan@uiowa.edu

ORCID (Edward G. Gillan): 0000-0002-2047-0929
ORCID (Ishanka A. Liyanage) 0000-0003-4814-0099

Abstract

Flexible synthetic routes to crystalline metal-rich to phosphorus-rich nickel phosphides are highly desired for comparable electrocatalytic HER studies. This report details solvent-free, direct and tin-flux assisted synthesis of five different nickel phosphides from $NiCl_2$ and phosphorus at moderate temperatures (500 °C). Direct reactions are thermodynamically driven via PCl_3 formation and tuned through reaction stoichiometry to produce crystalline Ni-P materials from metal-rich (Ni_2P, Ni_5P_4) to phosphorus-rich (cubic NiP_2) compositions. A tin flux in $NiCl_2$/P reactions allows access to monoclinic NiP_2 and NiP_3. Intermediates in tin flux reactions were isolated to help identify phosphorus-rich Ni-P formation mechanisms. These crystalline micrometer-sized nickel phosphide powders were affixed to carbon-wax electrodes and investigated as HER electrocatalysts in acidic electrolyte. All nickel phosphides show moderate HER activity in a potential range of -160 mV to -260 mV to achieve 10 mA/cm^2 current densities ordered as *c*-$NiP_2 \geq Ni_5P_4 > NiP_3 >$ *m*-$NiP_2 > Ni_2P$, with NiP_3 activity showing some particle size influence. Phosphorus-rich *c/m*-NiP_2 appear most stable in acidic conditions during extended reactions. The HER activity of these different nickel phosphides appears influenced by a combination of factors such as particle size, phosphorous content, polyphosphide anions, and surface charge.

Introduction

Hydrogen is widely recognized as a promising fuel source in sustainable and green energy applications with the merits of its high energy density and lower carbon footprint. Eco-friendly and cost-effective technologies for the routine generation of hydrogen in non-fossil fuel processes remains an important challenge.[1, 2] Water is an abundant and renewable source of hydrogen through water splitting reactions ($2H_2O \rightarrow 2H_2 + O_2$) that are comprised of H^+ reduction (hydrogen evolution reaction, HER) and O^{2-} oxidation (oxygen evolution reaction, OER). The HER component of water splitting has attracted a diverse range of electrocatalytic and photocatalytic strategies targeting feasible and efficient approaches for future hydrogen production.[3, 4] Precious metal-based catalysts such as platinum are well known as efficient and effective for electrochemical and photochemical water splitting reactions, but these are expensive and scarce materials. There are significant efforts focused on the development of more earth abundant, non-precious metal based HER catalysts that provide high catalytic efficiency, high stability, and low cost.[5, 6] A wide range of earth-abundant transition metals in compounds as borides, carbides, nitrides, oxides, sulfides, selenides, and phosphides have shown catalytic activity for water splitting hydrogen gas production in electrocatalytic HER processes.[7-12]

Metal phosphides have recently emerged as intriguing metal non-oxide alternatives for HER electrocatalysis. Earth-abundant first row transition metal phosphides (*e.g.*, Fe, Co, Ni, Cu), depending on phase and composition have sometimes shown impressive HER activity approaching that of benchmark expensive platinum catalysts.[13-16] Nickel phosphides have shown promising activity as robust HER electrocatalysts owing several useful compositional, structural, physiochemical, and electronic features.[15, 17-19] The nickel phosphides exist with wide compositional and structural variation from metal-rich and monophosphide phases (Ni_3P, Ni_5P_2, $Ni_{12}P_5$, Ni_2P, Ni_5P_4, NiP) to phosphorus-rich phases (NiP_2, NiP_3). Metal-rich phosphide structures have significant metal-metal bonding and exhibit metallic properties. Phosphorus-rich phosphides possess distinct structures with metal centers encapsulated in extended P-P bonded polyphosphide anion arrays and they are often semimetallic or small band gap semiconductors.[17, 20]

Metal-rich nickel phosphides, including faceted Ni_2P nanostructures are active hydrodesulfurization (HDS) catalysts and were evaluated for HER catalysis in view of mechanistic similarities between HDS and HER catalytic processes.[21] Highly active HER behavior of Ni_2P surfaces are proposed to involve dilution of active surface nickel sites in the presence of adjacent phosphorus sites. Nanostructured Ni_2P surfaces resembling hydrogenase enzyme active sites are catalytically HER active under acidic conditions.[22, 23] Numerous studies of metal-rich Ni_2P, including various nanostructures, films, bulk

powders, and some grown on conducting supports, show similar electrocatalytic HER activities and stabilities in aqueous 0.5 M H_2SO_4 with applied potentials to achieve a 10 mA/cm^2 current density in the range of about -140 to -240 mV (vs. RHE).[24, 25] Other metal-rich nickel phosphides such as $Ni_{12}P_5$ and Ni_5P_4 have also been explored as HER electrocatalysts. For example, $Ni_{12}P_5$ supported on Ti foil and $Ni_{12}P_5$ on carbon nanotubes achieve a 10 mA/cm^2 current density in 0.5 M H_2SO_4 at applied potentials as low as -107 mV and -129 mV, respectively.[26-29] Various Ni_5P_4 materials such as Ni_5P_4 nanosheets grown on Ni foam, Ni_5P_4 nanocrystals on glassy carbon, and Ni_5P_4 on reduced graphene oxide have low HER applied potentials to achieve 10 mA/cm^2 (range of -65 to -140 mV).[30, 31] Metal-rich nickel phosphide nanocrystals ($Ni_{12}P_5$, Ni_2P and Ni_5P_4) obtained via a surfactant-aided solvothermal route show an HER activity trend of $Ni_5P_4 > Ni_2P > Ni_{12}P_5$ suggesting that HER performance may be enhanced in more phosphorus-rich structures.[28] HER activity and acid corrosion resistance positively correlates with phosphorus-to-metal content that increases from $Ni_{12}P_5$ to Ni_2P.[29]

The potentially advantageous role of negatively charged surface phosphorus sites for HER activity and acid stability was theoretically investigated for Ni_2P and Ni_5P_4[32, 33] and comparisons of $Ni_{12}P_5$, Ni_2P, Ni_5P_4 and P-terminated NiP_2 surfaces suggest that phosphorus-rich surfaces possess energetically favorable hydrogen adsorption sites.[34] Appreciable HER electrocatalytic activity is observed for phosphorus-rich NiP_2 nanocomposites and bulk materials, despite their low nickel content.[35] Crystalline cubic NiP_2 (*c*-NiP_2) outperformed its monoclinic polymorph (*m*-NiP_2) in both acidic and alkaline HER electrocatalysis.[36, 37] We demonstrated that cubic and monoclinic NiP_2 polymorphs from exchange reactions at 500 °C show acidic HER activity comparable to previous reports.[38] There are few syntheses or electrocatalytic HER/OER activity reports for the highest phosphorus content NiP_3, but NiP_3 supported on CeO_2 was identified as an OER catalyst.[39] Both *c*-NiP_2 and NiP_3 have been examined as redox active anode materials in battery electrochemistry.[40-43]

Most previous synthetic and electrocatalytic studies on compounds in the Ni-P structural family report HER activity for metal-rich phosphides due to their preferred growth using solution and solid-gas phase reactions. Common synthesis methods of nickel phosphides include high-temperature elemental solid-state reactions[44-46] and surfactant-aided, metal-precursor based solvothermal reactions.[47-53] A popular metal phosphide synthesis strategy uses toxic PH_3 gas (often produced via the *in-situ* thermal decomposition of NaH_2PO_2) that is reacted with metal compounds.[24, 54, 55] Solvothermal and gaseous reactions run at moderate temperatures (≤350 °C) often produce nanostructured, sometimes poorly crystallized, metal-rich phosphides and monophosphides. Syntheses of phosphorus-rich phases are less

readily achieved via solvothermal and toxic PH_3 reaction strategies and instead, these are usually produced in elemental reactions at temperatures near 1000 °C.[43, 56]

Different synthetic preparations can produce significant variations in crystallinity, morphologies, and nanostructures that make it challenging to compare relative HER electrocatalytic activities for metal-rich and phosphorus-rich nickel phosphides from different synthetic studies.[13, 55] Recently observed discrepancies in HER activity trends for phosphorus-rich metal phosphide structures highlight the need for further understanding of the influence of different stoichiometric compositions and structures on HER electrocatalysis using nickel phosphides.[14, 55, 57] It is desirable to develop a facile, and tunable synthetic approach that can produce different of nickel phosphide structures and compositions for HER catalytic activity and stability comparisons.

We recently demonstrated that anhydrous metal chlorides react with elemental phosphorus at moderate 500 °C temperatures to produce a volatile PCl_3 and grow a range of crystalline, phosphorus-rich MP_2 or MP_3 structures (FeP_2, CoP_3, NiP_2, CuP_2, PdP_2).[38, 58] This solvent-free synthesis provides facile access to metastable *c*-NiP_2 and has been used by others for high quality *c*-NiP_2.[36] A low melting tin flux modifies the MCl_x/P reactions, leading to the formation of the stable *m*-NiP_2 polymorph along with a sublimed $SnCl_2$ byproduct. Isolation of phosphorus-rich metal phosphides from tin fluxes was achieved with 6 M HCl dissolution, which highlights the chemical robustness of these phosphorus-rich metal phosphides that contain potentially redox active polyphosphide anions.[38]

In this current study, we demonstrate that the solvent-free, moderate temperature (500 °C), direct $NiCl_2$/P and tin-flux assisted synthetic strategies successfully produce five crystalline compositions in the Ni-P system ranging from metal-rich to phosphorous rich phases. Rational changes in reaction stoichiometry enable a wide range of nickel phosphide phases to be produced from direct (Ni_2P, Ni_5P_4, *c*-NiP_2) and tin-flux assisted (*m*-NiP_2, NiP_3) reactions. Several intermediate reactions were studied to better understand the phosphorus-rich nickel phosphide growth process assisted by molten tin. The synthesis of these crystalline micrometer-sized nickel phosphides allows for improved comparisons of their relative HER electrocatalysts in acidic conditions using a flexible conducting carbon-wax electrode.

Experimental Procedures

Starting materials. The nickel phosphides were synthesized using sealed Pyrex ampoules (I.D. ~ 9 mm, O.D. ~13 mm). The reagents used as received were: $NiCl_2$ (anhydrous, vacuum dried at 250 °C, 4 hours, ~ 250 mTorr, Alfa Aesar, 99%), red phosphorus (vacuum dried, Aldrich, 99%), granular tin (Cerac -

100/+325 mesh, 99.8%), 12 M HCl (Fisher Scientific, ACS 36.5-38 %), and methanol (Fisher Scientific, 99.9%). Deionized water (18 MΩ) was obtained from a Photronix MiniQuad system. For electrochemical studies, the following materials were used: synthetic graphite powder (<20 μm, Sigma-Aldrich), paraffin wax (mp ≥ 65 °C, Sigma-Aldrich), concentrated H_2SO_4 (Certified ACS Plus 95-98%, Fisher Scientific), and 10% Pt on Vulcan XC-72 carbon (C1-10 fuel cell grade, E-Tek).

Reaction safety considerations. The reactions described here utilize red phosphorus that converts to pyrophoric molecular white phosphorus (P_4) vapor above ~400 °C. Ideal gas law pressure estimates must be performed prior to each reaction. Careful attention must be paid to transported materials from these ampoule reactions as flammable white phosphorus and air reactive liquid PCl_3 may be present, thus ampoules should be heated and carefully handled in a well-ventilated fume hood. After reaction, the oxidation of P_4 or PCl_3 should be accomplished using aqueous bleach or an equivalent oxidant. The hazardous use of concentrated acids (HCl and H_2SO_4) for tin flux removal, chemical analysis, and electrochemistry must be carefully performed in a fume hood with proper protective gear. Careful attention to personal safety must be also performed for carbon-wax electrode preparation that utilizes razor blades and hot wax injection into Teflon tubing.

Synthesis of nickel phosphides from direct $NiCl_2$ and red phosphorus reactions. Nickel phosphides were synthesized in sealed ampoules using anhydrous $NiCl_2$ and red phosphorus. These reactions are based on our recent work on P-rich metal phosphide growth (MP_2 or MP_3).[38, 58] In general, $NiCl_2$ was reacted with a stoichiometric amount of red phosphorus to produce either metal-rich or phosphorus-rich nickel phosphides and PCl_3 (mp/bp = -94/76 °C). Typical reagent amounts used are cubic NiP_2 (*c*-NiP_2) reaction with 0.133 g (1.0 mmol) of $NiCl_2$ and 0.085 g (2.7 mmol) of red phosphorus, Ni_5P_4 reaction with 0.259 g (2.0 mmol) of $NiCl_2$ and 0.097 g (3.1 mmol) of red phosphorus, and Ni_2P reaction with 0.261 g (2.0 mmol) of $NiCl_2$ and 0.074 g (2.4 mmol) of red phosphorus. The starting materials were ground together in an argon filled glove box with an agate mortar and pestle and loaded into a medium wall borosilicate glass ampule, which was then closed with a Cajon fitting and Teflon valve and removed from the glove box. Each tube was evacuated on a Schlenk line for ~15 minutes, and then the tube was flame sealed. The Ni-P reactions were heated in a horizontal Linberg Blue M-clamshell tube furnace to 500 °C at 100 °C/hr. All reactions were held at their reaction temperature for 48 hours.

To isolate the reaction product, the end of the tube without solid was pulled out of the furnace and cooled to near room temperature and a colorless PCl_3 liquid condensed on the cooled glass walls. When no further liquid condensed, the entire tube was cooled to room temperature. The cooled tube was cracked

open in air in the hood, carefully keeping the liquid by-product away from the solid. Once the tube was opened, some smoking was typically observed from PCl_3 that reacts with air/moisture. The solids were allowed to sit in air for several minutes before further isolation. The metal-rich Ni_2P and Ni_5P_4 products were isolated by washing with methanol for 3 hours followed by 6 M HCl for 1 hour. Phosphorus rich *c*-NiP_2 was isolated from 3 hours of 6 M HCl washing. The solids were rinsed several times in DI water until the pH of the wash solution was neutral. All solids were dried in air at room temperature, weighed, and then stored in vials. Note that once washed, all samples show long-term stability in air.

Synthesis of monoclinic NiP_2 and cubic NiP_3 in a tin flux. In our recent work, monoclinic NiP_2 (*m*-NiP_2) was produced from a $NiCl_2$/P reaction at 500 °C in the presence of a tin flux (mp = 232 °C) where the flux was high (fifteen times the mass of Ni/P reagents).[38] In this work, monoclinic NiP_2 was produced with much less tin flux, using a $NiCl_2$/P/Sn = 1/2/5 molar ratio with 0.132 g (1.0 mmol) of $NiCl_2$, 0.062 g (2.0 mmol) of red phosphorus and 0.595 g (5.0 mmol) of granular tin. Several attempts at NiP_3 synthesis were made using varying amounts of tin flux and phosphorus. NiP_3 reactions ranged from stoichiometric $NiCl_2$/P to excess P reactions with and without Sn. Two examples of successful NiP_3 reactions are: [$NiCl_2$/P/Sn = 1/5/5] using 0.131 g (1 mmol) $NiCl_2$, 0.155 g (4.9 mmol) red phosphorus, and 0.595 g (5 mmol) tin and [$NiCl_2$/P/Sn = 1/7/5] using 0.132 g (1 mmol) $NiCl_2$, 0.217 g (7 mmol) red phosphorus, 0.594 g (5 mmol) tin. The $NiCl_2$ and red phosphorus were first ground together in the glovebox, then mixed with granular tin, and added to a Pyrex ampule. Closed reagent-loaded ampules were removed from the glovebox, sealed as described above, and placed in the tube furnace at a slight angle to keep liquid tin flux at one end, heated to 500 °C at 100 °C/h, and held at 500 °C for 48 hours. At this point, one end of the tube is pulled out of the furnace to condense volatiles. In contrast to the direct M-P reactions, tin flux reactions generally transport a white solid that was identified as $SnCl_2$, consistent with our prior work.[38] Once transport was complete, the ampule was cooled to room temperature and carefully opened in the fume hood. The products were isolated from the tin flux using ~50 mL aliquots of 6 M HCl under magnetic stirring for about one day to dissolve the tin. The solids were rinsed several times in DI water until the solution pH was neutral and then dried in air at room temperature and weighed.

Mechanistic reaction studies. Several sequential reactions were performed to investigate possible mechanisms for tin-flux assisted nickel phosphide formation at 500 °C. Reaction of 0.027 g (0.22 mmol) of *c*-NiP_2 with 0.133 g (1.12 mmol) of granular tin was performed at 500 °C to target *m*-NiP_2 formation. Targeted NiP_3 reactions were conducted using *c/m*-NiP_2 in tin flux with excess phosphorus. Typical reagent amounts used in *c*-NiP_2/P/Sn reaction are 0.046 g (0.38 mmol) of *c*-NiP_2, 0.035 g (1.12 mmol) of red phosphorus and 0.181 g (1.52 mmol) of granular tin while in *m*-NiP_2/P/Sn reaction are 0.043 g (0.37

mmol) of *m*-NiP_2, 0.033 g (1.06 mmol) of red phosphorus and 0.169 g (1.42 mmol) of granular tin. A tin-rich phosphide, Sn_4P_3 was produced using 0.188 g (6.07 mmol) of red phosphorus and 0.949 g (7.99 mmol) of granular tin. In a subsequent experiment, 0.344 g (0.61 mmol) of Sn_4P_3 product was reacted with 0.081 g (0.62 mmol) of $NiCl_2$ targeting phosphorus rich NiP_3. In another experiment, 0.132 g (1.0 mmol) of $NiCl_2$ was reacted with different amounts of granular tin such as 0.240 g (2.0 mmol) and 0.595 g (5.0 mmol) targeting different Ni-Sn alloys. These as-synthesized Ni-Sn alloys were subsequently reacted with 0.155 g (5.0 mmol) of red phosphorus in sealed ampoules at 500 °C. Starting materials for each of above specified reactions were ground together in the glove box and proceeded to react under same reaction conditions as described in tin-flux assisted reactions. The products were isolated using ~50 mL aliquots of aqueous HCl, followed by DI water rinsing until pH of the wash solution was neutral. These isolated nickel phosphides were then air dried at room temperature and weighed.

Sample characterization. Powder X-ray diffraction (XRD) was performed using a Bruker D8 DaVinci diffractometer with nickel filtered Cu Kα radiation, (40kV, 40mA, 0.05° step size). Samples were ground to fine powders using a mortar and pestle and affixed to glass slides using a thin layer of vacuum grease. Reference XRD patterns and structural representations were generated using Crystal Maker (http://www.crystalmaker.com/index.html) and literature data for known Ni-P phases. ICP-OES data was collected on either a PerkinElmer Optima 7000 DV or Varian 720-ES system. Samples were dissolved in heated mixtures of 5-8 mL of concentrated HNO_3 and 1-2 mL of concentrated H_2SO_4 and diluted in 50 mL volumetric flasks with 5% (v/v) HNO_3. Linear calibration curves were generated using commercial standards. The surface analysis of nickel phosphide products was investigated using X-ray photoelectron spectroscopy (XPS) on Kratos Axis Ultra DLD photoelectron spectrometer using monochromated Al Kα X-rays and charge neutralization. Powders were embedded in indium foil and peak positions were referenced to adventitious carbon at 285 eV. XPS peak analysis (fwhm limit < 3 eV) was performed using CasaXPS software (www.casaxps.com). The morphology and elemental analysis of the samples were investigated using scanning electron microscopy (SEM) and energy dispersive spectroscopy (EDS) on a Hitachi S3400 (15 kV) or S4800 (3 kV or 5 kV) system. Samples were prepared by pressing pre-ground samples onto carbon tape on aluminum stubs.

Electrode preparation. The nickel phosphides and Pt/C powder reference catalyst were evaluated using a graphite powder/paraffin wax composite electrode similar to that described in our recent work.[38, 59, 60] Solid conducting graphite/carbon wax electrodes have been used in electrochemical analysis and are stable and inert with excellent reproducibility and negligible background current.[61-63] Relative to our prior work, slight modifications were made to the working electrode's graphite powder/paraffin wax

composition, tip connections, and process of catalyst particle deposition (**Figure S1**). A 50% graphite: 50% paraffin wax composition (by mass) for working electrode tips was identified as having better conductivity and retaining good adhesion for catalyst particles. The custom electrode tips were coned at the working end to reduce the PTFE lining at the electrode surface so that gas bubbles adherence to the electrode was diminished. The custom electrode tips were formed by placing melted graphite-wax into threaded and coned PTFE tubing (1.4 cm length, 3.2 mm ID, 6.4 mm OD) that provided working electrode tips with a 0.080 cm^2 geometric surface area.[38] Prior to sample loading, 50% graphite powder/paraffin wax (C_{wax}) electrode tips connected to brass current collectors were independently submerged for ~10 minutes in a preheated (55 °C) water bath to soften the wax for sample embedment. About ~1-2 mg of each catalyst sample was briefly sonicated with 20 µL of methanol to obtain a homogenous suspension of particles and ~5-10 µL aliquot of suspension was placed in an aluminum weigh boat to air dry. The aluminum weigh boat with air-dried catalyst was tared in the CAHN C-33 200 mg microbalance and then was placed in a preheated hot plate (55 °C) for ~ 5 minutes. The coned surface of the warmed blank tips was gently pressed onto the sample on the hot plate and excess powder on the PTFE lining of the loaded tips were carefully returned to the aluminum boat. The tip was pressed several times on a clear space on the weigh boat to assure sample embedment. The aluminum boat was weighed after catalyst loading and the catalyst mass loaded on the electrode tip was recorded; typical sample mass loadings ranged from about 0.5 to 1.0 mg.

Electrochemical measurements. Electrochemical experiments utilized a three-electrode, single compartment cell, a Bioanalytical Systems (BASi) 100b potentiostat, and were guided by literature best practices.[13, 64, 65] The cell consisted of a PTFE covered Pyrex beaker, the 50% C_{wax} working electrode-tip assembly described above, a single junction saturated calomel reference electrode (SCE; Pine Research), a platinum wire or graphite rod counter electrode (CE), and a magnetic cross stir bar placed directly under the working electrode (~6 mm away) to aid gas removal from the electrode surface and minimize surface adhesion of H_2 bubbles (**Figure S1**). The 50% C_{wax} electrode with catalyst sample embedded on its surface leads to ~40-50 Ω cell resistance values. Details of the experimental setup are similar those described in our recent work.[38, 59, 60]

Hydrogen evolution reaction (HER) polarization curves were obtained using linear sweep voltammetry (LSV) at 5 mV s^{-1} in acidic 0.5 M H_2SO_4 (pH = 0.3) aqueous solutions. The electrolyte solutions were continually purged with H_2 (ultra-high purity 99.999%, Praxair) to maintain a reversible (H^+/H_2) Nernstian potential in the solution for HER reactions.[65] The SCE reference was calibrated against reversible hydrogen electrode (RHE) values for the electrolyte solution using established conversions

[E(RHE) = E(SCE) + 241 mV + (59 mV) pH]. RHE adjustment for 0.5 M H_2SO_4 is 258.2 mV. All experimental and literature potential values are reported versus RHE. All current densities are calculated using the geometric surface area of the C_{wax} electrode (0.08 cm^2). Typically, 50 LSV scans without iR compensation and 20 LSV scans with 85% iR compensation were performed to verify reproducible sample responses and short-term sample stability. For iR uncompensated LSV scans, the potential was swept to negative values until applied potentials of about -750 mV were reached or, for 85% iR compensated LSV scans, the potential was swept until current density of about 50 mA/cm^2 is reached. Multiple LSV data sets were processed using a custom Excel macro program.[38] Extended stability experiments of samples in 0.5 M H_2SO_4 were analyzed by constant potential time base amperometry (chronoamperometery, CA) with the working electrode potential set at a value to ideally produce ~10-20 mA cm^{-2} current density and held at that potential for 18 hours.

Electrochemical surface area (ECSA) measurements were obtained from double layer capacitance (C_{dl}) values determined by cyclic voltammetry (CV) in the non-faradaic region (-100 mV to 350 mV RHE) in 0.5 M H_2SO_4 at scan rates from 5 to 75 mV s^{-1} similar to our prior work.[38] ECSA was calculated from the C_{dl} of each sample and the ideal specific capacitance (C_s, 35 μF cm^{-2}) of a planar electrode surface in 0.5 M H_2SO_4.[64, 66] Geometric electrode area is useful when catalytic surface reactions are limited by reactant transport, but ECSA accounts for electroactive surface area of embedded electrocatalyst particles. When different powders have similar particle sizes, normalization by geometric electrode area is sufficient for relative electrochemical comparisons.

Post-electrochemical analysis. Approximately 1-2 mm of the surface of each catalyst loaded working electrode tip was cut for post-electrochemical analysis and compared with similarly cut fresh catalyst loaded electrode tips (**Figure S1**). Powder X-ray diffraction (XRD) was done using a Bruker D8 DaVinci diffractometer with nickel filtered Cu Kα radiation, (40kV, 40mA, 0.01° step size, 27°-60° two theta). The cut electrode tip slices were affixed to a powder XRD holder using a thin layer of vacuum grease. The PTFE lining around the electrode tips was removed, they were pressed onto carbon tape on aluminum stubs for analysis by SEM and EDS mapping on a Hitachi S3400 system.

Results and Discussion

Direct nickel phosphide formation via PCl_3 elimination. Our prior metal phosphide synthesis work demonstrated flexible, moderate temperature, solvent-free procedures (direct or tin-flux assisted) to produce crystalline phosphorus-rich MP_2/MP_3 phases of a variety of 3d and 4d transition metals (Fe, Co, Ni, Cu, Pd).[38, 58] Successful direct MCl_2/P reactions at 500 °C are exothermic and proceed via PCl_3

elimination (ΔH_f = -320 kJ/mol). The Ni-P phase diagram is complex with a variety of metal-rich to phosphorus-rich phases (eight phases from Ni_3P to NiP_3 and six are room-temperature stable).[20] In this study, we examined the tunability of direct $NiCl_2$/P reactions to target a range of metal-rich (Ni_2P, Ni_5P_4) in addition to phosphorus-rich (*c*-NiP_2) nickel phosphides using rational modifications in reaction stoichiometry that still produce slightly thermochemically favorable reactions (ΔH_{rxn} < -20 kJ/mol Ni, **Table S1**). The balanced reactions for direct Ni_2P, Ni_5P_4 and *c*-NiP_2 synthesis are shown in **Equations 1-3** and highlight the potential new tunability of the simple direct $NiCl_2$/P reaction in producing metal-rich nickel phosphides.

$$2\ NiCl_2 + 7/3\ P \rightarrow \mathbf{Ni_2P} + 4/3\ PCl_3 \quad (1)$$

$$5\ NiCl_2 + 22/3\ P \rightarrow \mathbf{Ni_5P_4} + 10/3\ PCl_3 \quad (2)$$

$$NiCl_2 + 8/3\ P \rightarrow \mathbf{NiP_2} + 2/3\ PCl_3 \quad (3)$$

In each reaction, ground $NiCl_2$/P powders in evacuated ampoules visibly darkened to black color at ~250 °C indicating some initial surface reaction. Heating the reaction mixtures above ~420 °C will result in solid red phosphorus sublimation to gaseous molecular P_4. Continued heating to 500 °C, produces colorless PCl_3 vapor and black Ni-P products. Subsequent cooling of the reaction ampoule results in black NiP_x solids along with a colorless liquid transport, PCl_3 previously confirmed by ^{31}P NMR.[58] Initial Ni_5P_4 stoichiometrically balanced reactions (**Equation 2**) contained detectable Ni_2P (**Figure S2**), so a ~7% excess of phosphorus was used in the Ni_5P_4 reaction to minimize Ni_2P secondary phase formation.

Figure 1 shows a powder X-ray diffraction (XRD) comparison of the three nickel phosphide products (Ni_2P, Ni_5P_4, *c*-NiP_2) from direct $NiCl_2$/P reactions. The XRD results show that rational changes to the $NiCl_2$/P reaction stoichiometry yield crystalline metal-rich Ni-P phases Ni_2P (PDF #3-1863) and Ni_5P_4 (PDF #14-7901) as single-phase materials. Stoichiometric reactions produce single phase Ni_2P, while slight excess P reactions yield single-phase Ni_5P_4. Stoichiometric reactions also form phosphorus-rich cubic pyrite NiP_2 (*c*-NiP_2, PDF #3-2351) consistent with our prior work and verified by others.[36, 38] While the overall solid $NiCl_2$ - P_4 vapor reactions are expected to proceed similarly for the different reaction stoichiometries, their resulting crystal structures are distinct, with Ni_2P and Ni_5P_4 exhibiting prominent Ni-Ni (~2.5 – 2.6 Å) interactions as shown in **Figure 2** (additional images in **Figure S3**) that lead to more metallic character for these NiP_x phases.[18] This contrasts with *c*-NiP_2 that has Ni cation centers encapsulated in extended P-P bonded polyphosphide anion arrays arranged as $[P_2]^{4-}$ dumbbells, leading to long Ni-Ni contacts (3.87 Å).[17, 36] Prior synthetic studies describe the cubic NiP_2 phase as a high T/high P (metastable) phase (1200 °C, 65 kbar) produced from elemental solid-state reactions or high energy ball milling under inert atmospheres.[56, 58, 67]

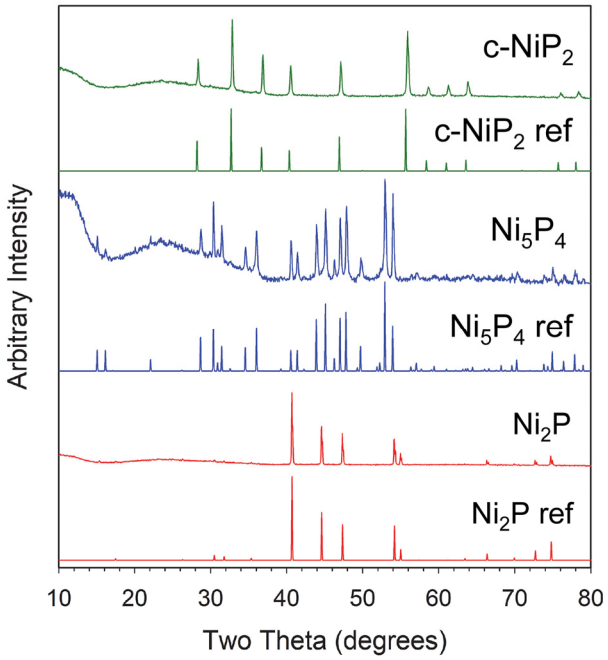

Figure 1. Powder XRD results for Ni-P products from direct 500 °C $NiCl_2$/P reactions with different stoichiometries. Reference (ref) patterns are shown below the experimental data.

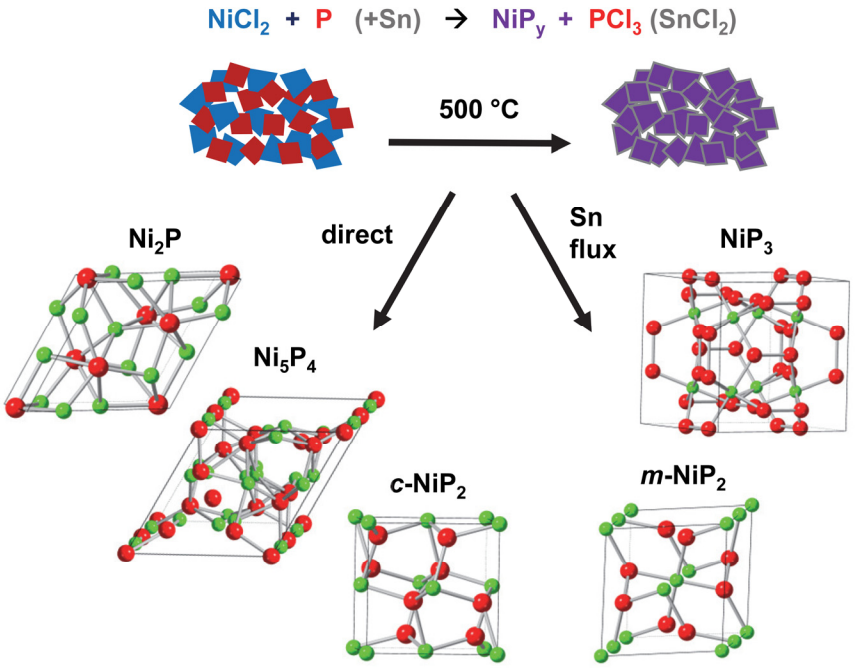

Figure 2. Schematic of solvent-free $NiCl_2$/P direct and tin flux reactions forming crystalline nickel phosphides at 500 °C with a wide range of compositions and structures. Unit cells shown for each structure (Ni green, P red). Extended structures for these compounds are shown in **Figure S3**.

Reaction and product characterization data for these Ni-P products are shown in **Table 1** and indicate that the overall stoichiometry of these three Ni-P materials is consistent with their crystalline phases that were isolated in high yields. These solvent-free 500 °C direct reactions show a good degree of phase control producing several metal-rich to phosphorous-rich crystalline Ni-P products. We previously speculated that the reaction of P_4 with the MCl_x surface favors polyphosphide formation,[38] but in the Ni-P system, a wider variety of Ni-P, Ni-Ni, and P-P bonding is accessible via this synthetic approach.

Table 1. Summary of experimental and characterization results for Ni-P products

$NiCl_2$/P/Sn molar ratio (target phase)	XRD product phase (crystallite size, nm)[1]	Mass yield[2] (%)	ICP molar ratios[3] Ni : P : Sn	SEM morphology (particle size, µm)
1/1.17/0 (Ni_2P)	Ni_2P (95)	79	1 : 0.50 : n/a	Irregular (~1-2)
1/1.55/0 (Ni_5P_4)	Ni_5P_4 (tr Ni_2P) (59)	86	1 : 0.85 : n/a	Irregular (~1-2)
1/2.7/0 (NiP_2)	*c*-NiP_2 (60)	83	1 : 1.81 : n/a	Elongated (~5-10)
1/2/5 (NiP_2)	*m*-NiP_2 (88)	53	1 : 1.80 : n/d	Blocky (~20-100)
1/5/5 (NiP_3)	NiP_3 (197)	83	1 : 2.46 : 0.003	Cube-like (~2-10)
1/7/5 (NiP_3)	NiP_3 (114)	84	1 : 3.2 : 0.006	Irregular (~1-2)

1) tr = trace peaks detected, crystallite size from XRD peak widths. 2) Yield based on target phase composition. 3) n/a = not applicable, n/d = below detection limits.

Tin-flux assisted nickel phosphide formation. While our direct $CoCl_2$/P reactions at 500 °C successfully produce cubic skutterudite CoP_3,[38] similar direct reactions targeting the NiP_3 analog from $NiCl_2$/P at 500 °C were unsuccessful and only produce crystalline *c*-NiP_2 using stoichiometric ($NiCl_2$/P of 1/3.6) or excess phosphorus ($NiCl_2$/P of 1/4.6) (**Figure S4**). There is a long history of molten metals such as tin (mp = 232 °C) facilitating reactions between metals and phosphorus. For example, elemental reactions in tin fluxes at 700 °C have produced NiP_3,[68, 69] and monoclinic, *m*-NiP_2 forms from a tin flux reaction using Ni/P/Sn molar ratios of 1/2/20 at 1150 °C.[70] Our prior work shows that a reactive tin flux for $NiCl_2$/P 500 °C reactions (using $NiCl_2$/P/Sn molar ratio of ~1/2.7/27), produces the thermodynamically stable *m*-NiP_2 phase along with a $SnCl_2$ byproduct (ΔH_f = -328 kJ/mol).[38] It is reported that an irreversible phase transition of *c*-NiP_2 to *m*-NiP_2 occurs at higher temperatures above 600 °C.[36] A tin flux also facilitates FeP_2 formation at lower temperatures than achieved via direct $FeCl_3$/P reactions.[38] The mechanism of reaction and intermediate formation in molten tin are likely more complex than in the direct MCl_x/P reactions.

We investigated lower tin contents in $NiCl_2$/P reactions to produce *m*-NiP_2 and utilized tin fluxes to access cubic NiP_3. In addition to causing less reaction interference, lower tin amounts make it easier to isolate products using 6 M HCl wash processes. After several trial experiments, a Ni/Sn molar ratio of 1/5 was identified as a reasonable ratio to produce *m*-NiP_2 and was used as a starting point for NiP_3 reactions (**Equations 4** and **5**). The stoichiometric reactions with $SnCl_2$ byproduct formation are thermodynamically favorable by enthalpy considerations (ΔH_{rxn} of -155 kJ/mol *m*-NiP_2,-183 kJ/mol NiP_3, **Table S1**).

$$NiCl_2 + 2\ P + 5\ Sn \rightarrow \mathbf{NiP_2} + SnCl_2 + [4\ Sn] \quad (4)$$

$$NiCl_2 + (3+x)\ P + 5\ Sn \rightarrow \mathbf{NiP_3} + SnCl_2 + [4\ Sn + x\ P] \quad (5)$$

Initial heating of these tin flux assisted reactions resulted in darkening of the reactant powder mixture and tin melting near 230 °C. Phosphorus may undergo a combination of vaporization near 400 °C, reaction with $NiCl_2$, and dissolution into the molten tin. Stoichiometric $NiCl_2$/P reactions performed at 500 °C with lower amounts of tin ($NiCl_2$/P/Sn = 1/2/5 molar ratio, ~1/5 the amount of Sn used in our prior work[38]) resulted in *m*-NiP_2 along with Ni_2SnP (**Figure S5**). Extended 6 M HCl washing of the crude product yielded shiny gray, single phase *m*-NiP_2 in ~50% yield. The Ni_2SnP phase detected in the crude reaction products indicates that metal salt reduction may take place in the tin flux along with phosphide formation and similar M-Sn-P phases are produced in elemental reactions with tin.[69] The *m*-NiP_2 structure consists of zigzag one-dimensional infinite polyphosphide $[P^-]_n$ anionic chains bonded to Ni^{2+} metal centers (**Figures 2** and **S3**).[36]

In the tin flux assisted NiP_3 reactions, excess phosphorus beyond the ideal Ni/P ratio (x=0 in **Equation 5**) was required to obtain cubic skutterudite NiP_3 as the only crystalline phase. Lower amounts of phosphorus lead to some *m*-NiP_2 formation (**Figure S6**). XRD results for NiP_3 from a 500 °C reaction with $NiCl_2$/P/Sn molar ratio of 1/5/5 is shown in **Figure 3**. The NiP_3 structure is analogous to cubic skutterudite CoP_3 with $[P_4]^{4-}$ polyphosphide rings encapsulating Ni^{3+} ions and leading to long Ni-Ni distances of 3.91 Å (**Figures 2** and **S3**).[68, 71] In both *m*-NiP_2 and NiP_3 tin flux assisted reactions, a white solid $SnCl_2$ transport was observed. Unwashed NiP_3 reaction products formed using excess phosphorus also show evidence of Sn_4P_3 formation (**Figure S7**). The Sn-P side products are readily soluble in 6 M HCl, and phosphorus-rich nickel phosphides (*m*-NiP_2, NiP_3) were isolated in good yields as shiny gray solids (**Table 1**).

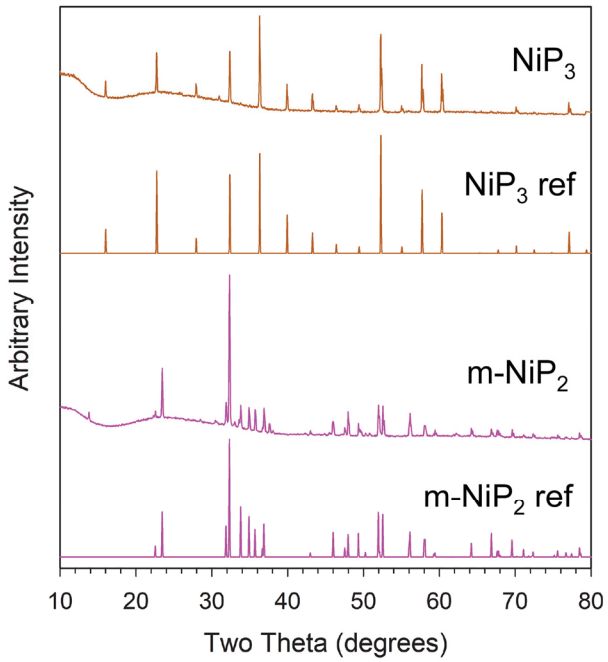

Figure 3. Powder XRD results for Ni-P products from 500 °C $NiCl_2$/P reactions with different stoichiometries using a tin flux. Reference (ref) patterns are shown below the experimental data. Results for NiP_3 from $NiCl_2$/P/Sn = 1/5/5 molar ratio and *m*-NiP_2 from $NiCl_2$/P/Sn = 1/2/5 molar ratio reactions.

An examination of different reactant ratios in the $NiCl_2$/P/Sn reactions showed successful single phase NiP_3 growth for several reactant molar ratios in this range: $NiCl_2$/P/Sn = 1/x/y where $10 \geq x \geq 4$ and $5 \geq y \geq 2$ molar ratios, several XRDs in **Figure S6**. There is some variation in the bulk composition from different NiP_3 preparations, but generally XRD single phase NiP_3 is observed for P/Ni product ratios of ~2.5 or higher. For example, **Table 1** shows that a $NiCl_2$/P/Sn reactant ratio of 1/7/5 produces NiP_3 with a bulk P/Ni ratio of 3.2. In general, the acid washed Ni-P products show negligible chlorine residue by EDS and little or no tin by ICP-OES. The NiP_3 materials formed in tin fluxes are isolated from 6 M HCl with high yields, so they are resistant to acid corrosion, which is desirable for HER electrocatalysis in acidic environments.

Morphology of different nickel phosphide products. Scanning electron microscopy (SEM) images of the direct grown nickel phosphide products are shown in **Figure 4** (additional images in **Figure S8**). The Ni_2P product consists of loosely packed aggregates of ~1-2 μm irregular particles with smooth surfaces. The Ni_5P_4 product is an aggregate of interconnected ~15-20 μm particles comprised of irregular ~1-2 μm particles. The *c*-NiP_2 product contains larger ~50-100 μm aggregates of ~5-10 μm thick, elongated

particles with rough exterior surfaces. The tin flux grown *m*-NiP_2 has large well-defined faceted monolithic blocky particles of ~20-100 μm (**Figures 5** and **S9**). For NiP_3, variations in particle size and morphology were observed for products grown with different phosphorus and tin amounts. The NiP_3 product grown with smaller tin amount (NiP_3 from $NiCl_2$/P/Sn ratio of 1/4/2) consists of ~30-50 μm aggregates of small spherical ~1 μm particles with rough exterior surfaces. The NiP_3 product grown with more tin (NiP_3 from $NiCl_2$/P/Sn ratio of 1/5/5) has extended regions of fused aggregates and well-defined faceted cube-like ~2-10 μm particles. Similarly, the NiP_3 product from $NiCl_2$/P/Sn ratio of 1/7/5 consists of ~25-30 μm aggregates of extended fused sheets comprised of smaller ~1 μm irregular particles. It appears that the particles from direct nickel phosphide reactions (Ni_2P, Ni_5P_4, *c*-NiP_2) are generally smaller and more irregular than the larger, faceted aggregates from tin flux growth (*m*-NiP_2, NiP_3). There are also some trends towards smaller NiP_3 SEM particle sizes for reactions using higher P/Sn ratios (>1). In electrocatalytic studies described below, an increase in electrochemically active surface area is also seen for NiP_3 produced using the larger P/Sn ratios (>1). Previous studies have observed that direct reactions using red phosphorus can produce macroporous metal phosphides[58] and higher temperature molten tin fluxes have been employed for large single crystal growth.[69]

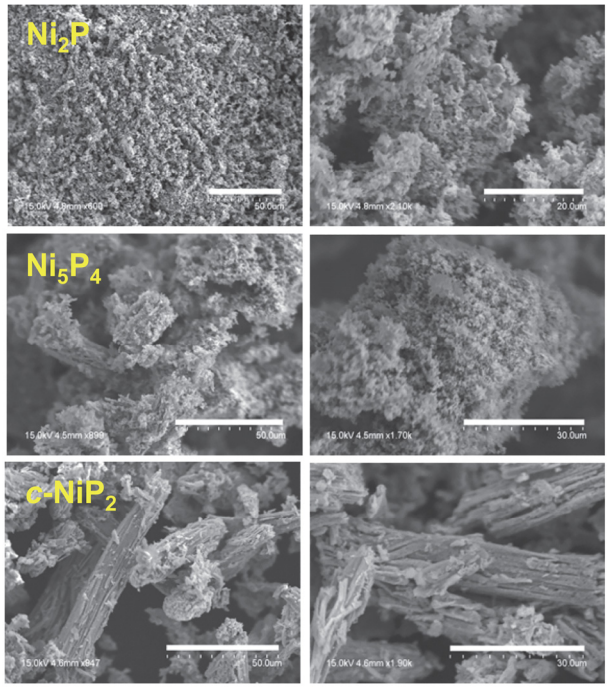

Figure 4. Representative SEM images of Ni-P products from direct $NiCl_2$/P reactions. Right images are higher magnification images of sample shown in the left image. Scale bars for left images are 50 μm long. Scale bars lengths for right images are 20 μm for Ni_2P and 30 μm for Ni_5P_4 and *c*-NiP_2.

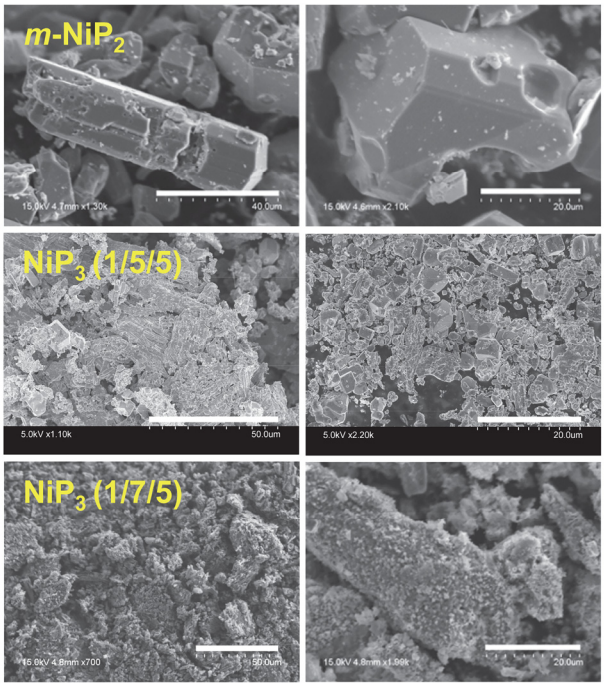

Figure 5. Representative SEM images of Ni-P products from tin flux $NiCl_2$/P reactions. Right images are higher magnification images of sample shown in the left image. Scale bars for left images are 40 μm long for *m*-NiP_2 and 50 μm long for the NiP_3 samples Scale bars lengths for right images are all 20 μm.

Surface analysis of several Ni-P structures. Bulk chemical analysis (**Table 1**) demonstrates that these five Ni-P structures have stoichiometries consistent with their compositions and have nearly undetectable tin residues (< 0.1%). Surface sensitive (~5 nm depth) XPS shows major Ni $2p_{3/2}$ peaks for the nickel phosphides at higher binding energy than metallic Ni $2p_{3/2}$ (852.2 eV) and P $2p_{3/2}$ peaks at lower binding energy than elemental P $2p_{3/2}$ (129.9 eV) (see **Table S2** and **Figure S10**). This is consistent with expected charge transfer from Ni to P leading to positively charged Ni species ($Ni^{\delta+}$) and negatively charged P species ($P^{\delta-}$) in these bulk structures and on their surface. The binding energies of Ni $2p_{3/2}$ peaks are in the range of ~853 - 855 eV and P $2p_{3/2}$ in range of ~128 - 130 eV. The Ni and P binding energies are consistent with literature values and previous data for other Ni-P structures such as Ni_2P[27, 28, 72] and both polymorphs of NiP_2.[36] The P 2p data is consistent with surface phosphide ($P^{\delta-}$) along with higher energy peaks for oxidized P such as $PO_x(OH)_y$ near 134 eV (**Table S2**). Similarities in Ni and P binding energies for low and high oxidation state Ni-P structures (e.g., Ni_2P versus NiP_3), suggest that the acidic wash processes create expected surface hydrolysis or oxidation.[39, 41] XPS analysis of these acid washed Ni-P products confirmed presence of Ni-P surface bonds as well as evidence of Ni-O and P-O

bonds. In some samples, surface chloride anions and Sn or SnO_x species are detected, and these are attributed to the HCl wash process or sampling a particulate region with residual tin from the flux. As is detailed later, EDS mapping of the phosphide powders mounted on electrode surfaces show uniform distributions of elements (Ni, P) in the microparticulate aggregates with no detectable tin.

Mechanistic studies to examine tin-flux assisted nickel phosphide formation. From the above results, tin appears to serve as a reactant as well as a liquid flux to facilitate *m*-NiP_2 and NiP_3 growth. Several intermediate and sequential reactions were conducted to better identify possible mechanisms operative in these tin flux assisted reactions (**Table S3**). **Figure 6** shows a graphical summary of the major crystalline products formed from different intermediate reactions. One possible reaction pathway is that the direct reaction of $NiCl_2$ particles with P_4 vapor occurs on the Sn surface to produce *c*-NiP_2 and PCl_3 gas at 500 °C. Since $SnCl_2$ is more thermodynamically stable than PCl_3, subsequent reactions between PCl_3 and Sn can produce the observed $SnCl_2$ transport. Since *m*-NiP_2 is formed instead of *c*-NiP_2, it is possible that the tin flux recrystallizes a cubic product to its thermodynamically stable monoclinic phase. An experiment with *c*-NiP_2 reacted with Sn at 500°C (using Ni/Sn molar ratio of 1/5), resulted in primarily *c*-NiP_2, so the cubic phase's kinetic stability appears sufficient to resist conversion to *m*-NiP_2 in our P/Sn reactions. This suggests that *m*-NiP_2 forms or crystallizes in the tin flux directly or via different intermediates. The tin flux with excess P may facilitate conversion of either *m*-NiP_2 or *c*-NiP_2 to NiP_3 (**Table S3** and **Figure S11**).

A possible sequential reaction could occur where phosphorus dissolves in molten tin and then reacts with $NiCl_2$ to form *m*-NiP_2/NiP_3 and $SnCl_2$ (**Figure 6** and **Table S3**). According to the Sn-P phase diagram, molten tin dissolves ~9 mol % of phosphorus at 500 °C[20] and crystalline Sn-P products are observed when excess phosphorus is present. To verify tin phosphide formation, Sn/P reactions were performed at 500 °C and produced crystalline Sn-P phases (Sn_4P_3, Sn_3P_4, **Figure S12**). The isolated Sn-P products were subsequently reacted with $NiCl_2$ at 500 °C to produce *m*-NiP_2 but no detectable NiP_3, so this sequential reaction may be operative for NiP_2 formation (**Figure S13**). Notably, the formation of intermediates such as Sn_4P_3 (ΔH_{rxn} = -29 kJ/mol) and NiP_x products using $NiCl_2$/Sn_4P_3 reactions (ΔH_{rxn} = -125 kJ/mol of *m*-NiP_2, ΔH_{rxn} = -154 kJ/mol of NiP_3) are thermodynamically favorable.

A third possible sequential reaction (**Figure 6**) is one where $NiCl_2$ is reduced by molten tin to form a Ni-Sn alloy that subsequently reacts with gaseous molecular phosphorus vapor and/or phosphorus dissolved in the tin flux. Experiments using $NiCl_2$/Sn at 500 °C were performed and several crystalline Ni-Sn phases along with $SnCl_2$ was produced, depending on relative amounts of Sn used (Ni_3Sn, Ni_3Sn_2, Ni_3Sn_4

using low to high tin-flux amounts, **Figure S14**). A variety of Ni-Sn alloys were then reacted with phosphorus at 500 °C to target NiP_3, but they produced mixtures of NiP_3 and *m*-NiP_2 along with possible trace Sn_4P_3 (**Figure S15**). The formation of stable Ni-Sn alloy intermediates such as Ni_3Sn (ΔH_{rxn}= -60 kJ/mol of Ni), Ni_3Sn_2 (ΔH_{rxn} = -90 kJ/mol of Ni), Ni_3Sn_4 (ΔH_{rxn} =-104 kJ/mol of Ni) from $NiCl_2$/2Sn or 5Sn reactions are very exothermic and their subsequent reactions with excess P to form either *m*-NiP_2 or NiP_3 are also exothermic regardless of the Ni-Sn alloy reactant. These intermediate formation experiments indicate that reaction pathways involving metal reduction and Sn-P intermediates could be responsible for the formation of *m*-NiP_2 or NiP_3 from $NiCl_2$/P reactions in molten tin, depending on phase and reactant ratios. The stability of Sn-P and/or Ni-Sn intermediates may serve to help sequester both Ni and P inside the molten tin flux and facilitate Ni-P product crystallization from the melt.

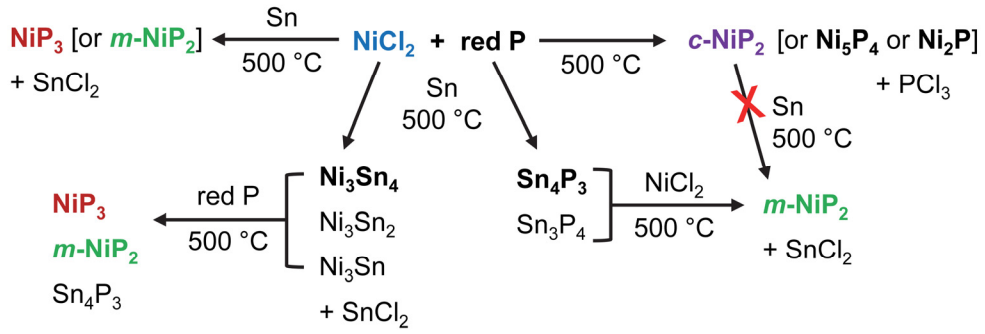

Figure 6. Summary of various reactions and product formation that inform possible intermediate reaction pathways for phosphorus rich Ni-P phase formation from $NiCl_2$/P facilitated by molten tin.

Comparison of relative electrocatalytic HER activity for different nickel phosphide phases. While metal sites are typically invoked as key catalytic surface reaction sites for hydrogen adsorption and reduction in HER, recent reviews and theoretical studies on nanostructured metal-rich nickel phosphides indicate that anionic phosphorus surface sites may be energetically favorable for hydrogen adsorption and reduction versus metal surface sites in HER electrocatalysis.[14, 32, 33, 55] Theoretical studies on Ni_2P and Ni_5P_4 identified that both Ni-rich and P-rich surface sites on surfaces of faceted nanoparticles may favor hydrogen adsorption and reduction in acidic HER.[22, 23, 32] Bonding to P-rich surfaces on Ni_5P_4 is proposed as a reason for its higher HER activity. The Ni-Ni bonding in Ni_2P and Ni_5P_4 may also render them more reactive in aqueous acidic media. The higher phosphorus content metal phosphides with structural polyphosphide anions can increase surface phosphide sites for hydrogen adsorption and reduction. The

polyphosphide anions may also allow new catalytic redox flexibility by accessing various phosphorus oxidation states in the polyphosphide chain.

Differences in product crystallinity and synthetic methods used vary considerably across reported nickel phosphides, leading to challenges in making direct comparisons of their relative HER activity.[13, 14, 55] For example, nanoscale Ni_2P and Ni_5P_4 with different morphologies are produced from surfactant-aided, metal precursor-based solvothermal reactions or gas-solid reactions using *in-situ* generated PH_3 at low temperatures (≤ 350 °C).[23, 24, 28, 30] These nanostructured metal-rich nickel phosphides have shown impressive HER activities that are sometimes near platinum levels of catalyst activity.[23, 28-30] Experimental investigations on the effect of phosphorus content on HER activity observed the trend of $Ni_5P_4 > Ni_2P > Ni_{12}P_5$ (-118 mV, -137 mV, and -208 mV applied potentials for 10 mA/cm^2, respectively) with Ni_5P_4 reported as the most HER active and corrosion resistant in acidic electrolyte.[28-30] A comparison of prior HER electrocatalysis results on several Ni-P materials is compiled in **Table S4**. As demonstrated above, our stoichiometrically tunable $NiCl_2$/P reactions produce crystalline single-phase Ni_2P, Ni_5P_4, *c*-NiP_2, *m*-NiP_2, and NiP_3 micrometer-sized particles. Their similarity in preparation permits a better relative comparison of their electrocatalytic HER activities versus comparing results from different experimental studies that use different preparation methods, form phosphides with varying degrees of crystallinity, and make measurements with different electrode materials.

The relative electrocatalytic HER performance of crystalline nickel-rich to phosphorus-rich phases synthesized in this work were evaluated in a three-electrode system in H_2-saturated 0.5 M H_2SO_4 with powders adhered to sticky conducting carbon-wax working electrodes (50% graphite: 50% paraffin wax by mass) analogous to our recent work (**Figure S1**).[38, 59, 60] Representative negative applied potential linear sweep voltammetry (LSV) curves for each Ni-P sample are shown in **Figure 7**. LSV data was obtained without iR compensation and higher relative HER activity is indicated by increased current flow at lower negative applied potentials. We also obtained LSVs with 85% iR compensation, which may help "normalize" data from different materials and different solution resistances, but it can also mask materials differences in surface catalysis or charge accumulation ability.[64, 73] LSV overlay plots and run number graphs charting changes in applied potentials versus current densities for LSV runs for both uncompensated (50 LSV) and iR compensated (20 LSV) data are shown in **Figure S16-S21.** HER activities for all samples show stable HER activity within the first couple of LSV runs.

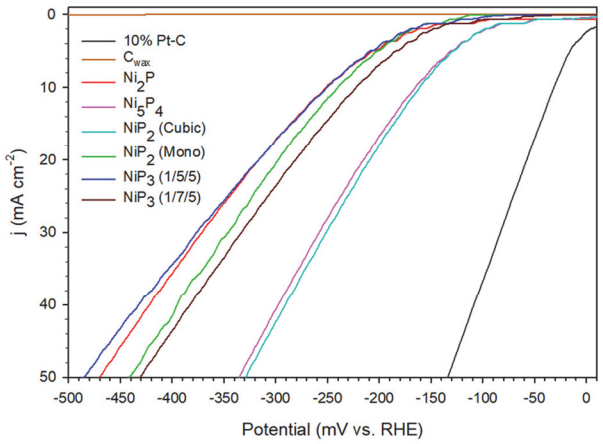

Figure 7. Representative LSV data taken in 0.5 M H_2SO_4 (5 mV/s scan rate) for various Ni-P particles embedded on a C_{wax} working electrode using Pt wire counter and SCE reference in a three-electrode cell. NiP_3 shown is from both $NiCl_2$/P/Sn 1/7/5 and 1/5/5 reactions. Data shown here are without iR compensation (85% iR compensated data is shown in **Figure S16-S21**). Plots for C_{wax} and embedded commercial 10 wt% Pt/C are also shown for comparison.

The average LSV results for HER electrocatalysis in 0.5 M H_2SO_4 are summarized in **Table 2**. The HER activity of the five nickel phosphides is reproducible over at least 50 LSV runs with low to moderate deviations from average values. Instrumental iR corrections for cell resistance decrease the applied potentials required for 10 mA/cm^2 current flow by ~25-50 mV.

Table 2. Summary of HER electrocatalysis results for various Ni-P phases in 0.5 M H_2SO_4[1]

Ni-P direct or Sn assist (M/P/Sn)	**10 mA/cm^2 (mV)^2**	**20 mA/cm^2 (mV)^2**	**Tafel slope (mV/dec)**	**ECSA (cm^2)^3**	**Extended stability[4]**
Ni_2P-direct (1/1.17/0)	-250 ± 10 (-204 ± 1)	-315 ± 12 (-288 ± 1)	-102 ± 5 (-94 ± 2)	14/2	77%
Ni_5P_4-direct (1/1.55/0)	-163 ± 4 (-132 ± 2)	-213 ± 4 (-159 ± 3)	-87 ± 1 (-74 ± 8)	24/9	68%
c-NiP_2-direct (1/2.7/0)	-161 ± 2 (-136 ± 1)	-210 ± 2 (-162 ± 1)	-108 ± 8 (-78 ± 2)	21/16	96%
m-NiP_2 (1/2/5)	-239 ± 3 (-194 ± 1)	-296 ± 4 (-228 ± 1)	-126 ± 1 (-95 ± 2)	2/2	90%
NiP_3 (1/5/5)	-255 ± 2 (-204 ± 7)	-321 ± 2 (-236 ± 7)	-95 ± 1 (-78 ± 5)	4/2	67%
NiP_3 (1/7/5)	-220 ± 8 (-175 ± 4)	-279 ± 8 (-204 ± 4)	-87 ± 2 (-75 ± 1)	24/6	73%
10%Pt/C	-31 ± 4 (-8 ± 1)	-57 ± 8 (-33 ± 2)	-49 ± 2 (-31 ± 3)	27/44	30%

1) LSV results in 0.5 M H_2SO_4 with SCE reference converted to RHE, Pt wire counter, powders embedded on a carbon-wax electrode. 2) Average data from 50 LSVs and current densities scaled for 0.08 cm^2 geometric electrode area. Average 20 LSV results using 85% iR correction in parentheses. 3) Data shown before/after 50 LSVs. 4) From constant potential amperometry measurements over the 30 min to 18-hour period.

The crystalline Ni-P phases require moderate negative applied potentials for appreciable electrocatalytic H_2 generation. The most metal-rich phosphide, Ni_2P, has the lowest HER activity while the nearly stoichiometric Ni_5P_4 and P-rich *c*-NiP_2 phase show higher (and similar) HER activity at smaller negative applied potentials (**Table 2**). The HER results for direct synthesis products Ni_2P, Ni_5P_4, and *c*-NiP_2 indicate that as more phosphorus is introduced in the structure, higher H_2 generation is achieved at the same applied potentials (*c*-$NiP_2 \geq Ni_5P_4 > Ni_2P$). These phosphides also generally have smaller SEM particle sizes and higher electrochemically active surface area (ECSA), which may influence their relative HER activity (**Table 1** and **2** info).

The *m*-NiP_2 and NiP_3 phases from tin flux reactions both show moderate HER activity and better than Ni_2P. As **Figure 7** and **Table 2** show, there is a group of phases (Ni_2P, *m*-NiP_2, NiP_3) with 10 mA/cm^2 current densities near -240 mV and a lower applied potential group (Ni_5P_4, *c*-NiP_2) near -150 mV and these groupings hold regardless of iR compensation. The phosphorus-rich nickel phosphide phases *m*-NiP_2 and NiP_3 (1/5/5) from molten tin fluxes generally have larger particle sizes and correspondingly lower ECSA values, which might be part of the reason for their lower HER behavior relative to directly synthesized *c*-NiP_2. The NiP_3 sample synthesized with higher excess P ($NiCl_2$/P/Sn of 1/7/5) has elemental analysis near NiP_3 and shows slightly higher activity at lower applied potentials than the NiP_3 (1/5/5) sample. This higher activity for NiP_3 (1/7/5) may be due to its higher ECSA and smaller particle size. As shown in **Table 1** and **Table S5**, NiP_3 reactions with higher P/Sn reactant ratios (1/7/5 and 1/4/2) result in NiP_3 products with higher ECSA values than the NiP_3 (1/5/5) product and they show similarly improved HER activities. The applied potentials to achieve 10 mA/cm^2 current density are in the -130 to -200 mV range (iR compensated) and their HER catalytic activity follows the trend of *c*-$NiP_2 \sim Ni_5P_4 >$ NiP_3 (1/7/5) > *m*-NiP_2 > NiP_3 (1/5/5) ~ Ni_2P. A direct comparison of these Ni-P results with prior nickel phosphide HER reports is challenging owing to differences in crystallinity (or amorphous materials) or nanostructuring or use of a catalyst growth support. Many prior studies are on metal-rich nickel phosphides with higher surface areas and smaller particles than those in this study and some report high current densities at lower applied potentials while others fall into a similar potential range as our work (see **Table S4** for literature comparisons). For example, Ni_2P as an HER electrocatalyst achieves 10

mA/cm^2 current densities ranging from about -140 mV to -240 mV depending on morphology and support. Our crystalline and micrometer-size aggregated Ni-P materials show slightly lower activities as compared to nanostructured Ni_2P.

In general, all three P-rich structures (*c*/*m*-NiP_2 and NiP_3) show impressive HER activity when considering their low 25-33% Ni content versus the metal-rich Ni_2P (67% Ni) and Ni_5P_4 (56% Ni) structures. In comparing the two polymorphs of NiP_2, the *m*-NiP_2 product has a lower ECSA than *c*-NiP_2, which may account for its lower HER activity. The different oxidation states of the cubic (Ni^{4+}/P^{2-} dumbbells) versus monoclinic (Ni^{2+}/P^{-} chains) NiP_2 or different redox properties of the polyphosphide networks (*e.g.*, dimers versus chains, see **Figures 2** and **S3**) may also influence surface reduction reactions.

While catalytic activity should not depend on the amount of the catalyst, for similar amounts, if surface areas differ greatly, this could lead to higher current densities for materials with higher ECSA values. To examine this possible influence, a plot of iR compensated LSVs scaled to ECSA instead of geometric electrode surface area shows that the relative activity of some Ni-P materials changes when scaled by ECSA (**Figure 8**). While several Ni-P phases show close overlap, the *m*-NiP_2 and NiP_3 (1/7/5) products are relatively more and less active, respectively than shown in **Figure 7**, leading to an ECSA scaled relative HER activity ordering of: *m*-NiP_2 > Ni_5P_4 ~ *c*-NiP_2 ~ NiP_3 (1/5/5) > NiP_3 (1/7/5) > Ni_2P. This reinforces the challenge of identifying a single reason for an observed trend in relative HER activities that may be influenced by particle size and electrochemically active surface sites, in addition to phosphorus content (and P anion influence on redox behavior) and Ni-P surface structures.

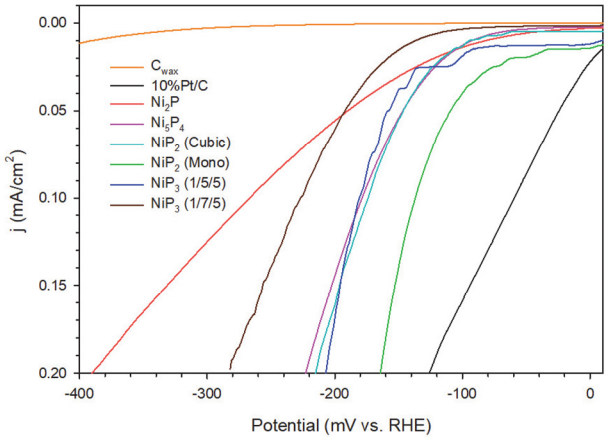

Figure 8. Representative applied potential versus current density plots for several Ni-P products that are normalized to measured ECSA values using 85% iR compensation.

The extended stability of the different nickel phosphides synthesized here was evaluated by constant potential time base chronoamperometry (CA) experiments in 0.5 M H_2SO_4 held for 18 h at an applied potential to produce ~10-20 mA/cm^2 current density based on LSV data (**Table 2**). Metal rich Ni_2P and Ni_5P_4 phases retained ~70-80% of initial activity after 18 h (CA extended stability data using Pt or graphite CEs are shown in **Figures S22** and **S23**). This instability of metal-rich nickel phosphides has been observed in corrosive acidic environments.[23, 29] The highest phosphorus content NiP_3 showed steady loss in HER activity loss similar to metal-rich phosphides. In contrast, both *c*-NiP_2 and *m*-NiP_2 showed very good stability over time retaining greater than 90% of the initial activity. These phosphorus-rich structures with nickel ions encapsulated by polyphosphide anion networks may serve to minimize nickel loss and decomposition and favor stabilization of P-H bonds on the Ni-P surface. CA studies and LSV polarization overlay curves show little or no detectable influence from use of a Pt CE versus graphite CE (**Figure S24**), which has been identified as a potential issue in some acidic HER electrocatalysis.[74]

Post-electrochemical analysis of catalysts on C_{wax} electrodes. After the extended stability CA experiments, the catalyst loaded working electrode tips were cut off for postmortem analysis. The powder XRD of the nickel phosphide catalysts on a C_{wax} support before and after CA experiments is shown in **Figures S25** and **S26**. Good crystallinity was retained by all the phosphorus-rich nickel phosphide catalysts after 18 h revealing their chemical robustness in reducing, acidic HER environments. A more notable loss of crystallinity was observed for the metal-rich phases (Ni_2P and Ni_5P_4), consistent with their lower acid stability for extended periods. SEM analysis of the post CA experiment electrode tips shows that the large micrometer sized *m*-NiP_2 and NiP_3 crystallites retained their original morphology, but smaller Ni_2P, Ni_5P_4, and *c*-NiP_2 particles were partly embedded in carbon wax electrode surface, making visualization of their morphology more difficult (**Figures S27** and **S28**). The EDS elemental maps (Ni, P, O, C) of nickel phosphides on C_{wax} electrodes before and after CA experiments are compared (**Figure S29-S34**). Generally, a homogeneous distribution of Ni and P was observed on both the fresh catalyst loaded electrode surface and postmortem electrode surfaces after HER. No tin residues were detectable on *m*-NiP_2 or NiP_3 particles before or after the CA experiments. EDS compositional analysis of each post-CA nickel phosphide electrode surface shows that lower phosphorus and higher oxygen content is present versus the fresh catalyst (**Table S6**). These observations of possible catalyst surface oxidation and formation of oxide/phosphate surface layers under HER acidic conditions are consistent with previous reports.[30, 34] The composition of *c*-NiP_2 was maintained after 18 h CA experiments, providing further support for it having high stability in an acidic and reducing environment.

Hydrogen surface reduction results compared with theoretical precedents. While the nickel phosphides studied here are good electrical conductors with low or zero band gaps, their different polyphosphide anion structures can impact different surface structures for metal stabilization and proton adsorption and reduction in HER electrocatalysis. The Ni-P products formed with and without tin can lead to differences in composition, particle size, aggregation, and ECSA related to surface charge. Some of the more active Ni-P phases have higher ECSA values, which can influence HER activity, though it does not appear as the major distinctive property. The rate of H_2 formation may be limited by initial proton adsorption and reduction step on a surface site (M-H formation, Volmer step) or limited by the combination two adjacent adsorbed hydrogen atoms (2 M-H → H_2, Tafel step), limited by a step when H_2 is formed by combination/reduction of an adsorbed hydrogen with second H^+ from solution (M-H/H^+ → H_2, Heyrovsky step). An analysis of the initial (Tafel) slopes of LSV curves has been correlated with different kinetically slow steps for the surface catalyzed reaction of 2 H^+ → H_2. Initial Tafel slopes near 120 mV/dec, 30 mV/dec, or 40 mV/dec are ascribed to primarily Volmer, Tafel or Heyrovsky rate determining steps.[75] As shown in **Table 2**, the initial Tafel slopes for this series of nickel phosphides are in the range of about 90 to 130 mV/dec, which is consistent with HER mechanisms in acidic conditions described as mixed Volmer-Tafel or Volmer-Heyrovsky reactions on catalytic surface sites. The Tafel slopes for these nickel phosphide catalysts near 100 mV/dec suggest H_2 formation is limited by primarily Volmer-type surface proton adsorption and reduction. Reported Tafel slopes for metal-rich Ni_2P and phosphorus rich *c*-NiP_2 grown on carbon nanofibers are similar to our values and a Volmer-Heyrovsky mechanism is proposed as the limiting reaction step for *c*-NiP_2 HER.[34]

The different physical and electronic structures in Ni-P catalysts can impact interactions between 1s H orbitals and surface sites during HER electrocatalysis.[78] In considering the local bonding of five Ni-P structures synthesized in this work, there are differences in Ni-Ni versus Ni-P and P-P bonding interactions (**Figure 2** and **S3**). Close Ni-Ni contacts (~2.5 Å) and primarily isolated P^{3-} anions are found in metal-rich Ni_2P and Ni_5P_4 structures versus phosphorus-rich nickel phosphides that have longer Ni-Ni separation (~3.9 Å) and polyphosphide anions ranging from P_2^{4-} dimers (*c*-NiP_2), zigzag $[P^-]_n$ chains (*m*-NiP_2) and P_4^{4-} square rings (NiP_3).[17, 32, 33, 36, 71] These nickel phosphides also show a variety of formal oxidation states for Ni (+1 to +4) and P (-1 to -3) and Ni/P coordination geometries varying from square planar to tetrahedral to trigonal bipyramidal to octahedral. The electronic structures of these nickel phosphides indicate that predominantly Ni 3d orbitals are intermixed with P 3p orbitals to form their valence band structures.[18, 76-78] As shown in **Figures 2** and **S3**, a variety of surface structures with Ni-P

and/or P-P bonding is present on low index unit cell faces and these can influence proton binding to the catalyst surface and subsequent reduction and hydrogen migration.

Several theoretical DFT studies have calculated the relative strength of hydrogen bonding to various crystallographic planes of different Ni-P structures with the bond energies described by the Gibbs free energy of hydrogen adsorption (ΔG_H) and surface charge transfer capabilities.[34, 55, 76, 78] These computational results are generally performed on pristine surfaces without solvent/water effects. Relatively low surface adsorption/bond energy on Ni, P, or combined Ni-P sites can favor migration to and/or bonding with another H/H^+ leading to H_2 formation. The overall importance of modest hydrogen bonding to a catalyst surface is described as the Sabatier Effect and some DFT predictions provide insight into surface catalytic reactions.[79] The ΔG_H values reported for most of the metal-rich to phosphorus-rich nickel phosphides predict that protons can adsorb moderately or strongly to surface catalytic sites with binding that greatly varies with surface structures present on different crystal facets.

The Ni_2P and Ni_5P_4 surfaces with P-rich regions are predicted to have relatively lower P-H adsorption energies than their Ni-H counterparts, suggesting that anionic and Lewis basic P surface sites may be preferred for H^+ adsorption and reduction even in structures with close Ni-Ni contacts. For example, the ΔG_H for Ni sites on Ni_2P and Ni_5P_4 surface are calculated near -0.5 eV, while ΔG_H for P sites on Ni_2P and Ni_5P_4 are near -0.1 eV.[32, 33] Some crystallographic planes for Ni_2P are predicted to have a very small ΔG_H and show higher relative HER activity versus phosphorus-rich phases (*m*-NiP_2, NiP_3),[78] though opposite predictions are made in other studies.[34] One study calculated ΔG_H for (111) surfaces of Ni_2P, Ni_5P_4 and *c*-NiP_2 (P terminated) of -0.27 eV, -0.22 eV and -0.02 eV respectively,[34] suggesting that the lower H adsorption energy in phosphorus-rich *c*-NiP_2 (close to ΔG_H of -0.09 eV for Pt) may facilitate its higher HER activity compared to Ni_2P. These findings are consistent with our observed HER activity trend of *c*-$NiP_2 \geq Ni_5P_4 > Ni_2P$. Our relatively low HER activity for Ni_2P is consistent with other experimental studies[28, 29] and may be related to its poor chemical stability or surface hydrolysis in acidic environments and overall activity reflects multiple crystallographic facets present in polycrystalline particulate catalysts.

In contrast to the low ΔG_H for the metal-rich Ni-P structures and *c*-NiP_2, theoretical studies on *m*-NiP_2 and NiP_3 predict relatively larger adsorption energies in the range of -0.5 to -1.5 eV corresponding to stronger hydrogen surface bonding that can hinder H_2 formation and impact HER activity.[78] NiP_3 surfaces are also predicted to have large water adsorption energy of -0.63 eV, which may lead to water blocking reactive surface sites.[39] As compared to *m*-NiP_2, NiP_3 is predicted to have relatively smaller ΔG_H values for several similar crystallographic planes, consistent with our observed higher H_2 production

by NiP_3 versus *m*-NiP_2. Also, *m*-NiP_2 shows lower relative HER activity than *c*-NiP_2 in our study and consistent with previous reports.[36, 38] Although these surface hydrogen reactions play a considerable role in HER performance, direct correlations of computed gas phase ΔG_H to bulk phase HER activity is challenging as real particulate catalysts display a variety of crystallographic faces and include a range of aggregation and shapes that may impact the net observed HER activity. Additional real-world issues around water surface reactions to form hydroxides or phosphates can also impact observed electrocatalytic activity.

Conclusions

Solvent-free, direct and tin-flux assisted $NiCl_2$/P reactions at moderate temperature (500 °C) are demonstrated as synthetically tunable to produce a range of five crystalline nickel phosphides (Ni_2P, Ni_5P_4, *c/m*-NiP_2 and NiP_3). These crystalline single-phase Ni-P structures form as microparticle aggregates with some nanoparticulate features. Mechanistic insight into the actions of the tin flux additive was achieved using intermediate stage reactions. The tin flux can serve as a metal halide reductant, phosphorous reservoir, and metal phosphide recrystallization medium. In the case of NiP_3, excess phosphorus in the tin flux reaction led to a smaller particle size and higher ECSA product. These results suggest further tunability of other metal phosphide syntheses using this synthetic approach. The tunable synthesis of these five different Ni-P structures and compositions allows for a comparable evaluation of their HER catalytic activity and stability. The relative HER activities were measured as *c*-NiP_2 ~ Ni_5P_4 > NiP_3 (1/7/5) > *m*-NiP_2 > NiP_3 (1/5/5) ~ Ni_2P and all retain their crystalline bulk structures after 18 h constant potential testing, with the *c/m*-NiP_2 materials showing the best acid stability during extended HER reactions. Relative electrocatalytic HER activities and materials stability appear to be a function of several factors including particle size, electrochemically active surface area, phosphorus content, and surface structures for proton bonding, all of which can be influenced by the polyphosphide anions and crystallite growth processes.

Acknowledgments. The authors gratefully thank Matthew Lovander for preliminary electrochemical analysis and assistance with carbon-wax electrode designs and gratefully acknowledge funding support from a U.S. National Science Foundation (Division of Chemistry) under grant No. 1954676 and the University of Iowa. Staff in the UI MatFab (K. Horkley and P. Pagano) are thanked for assistance with SEM and XPS. Any opinions, findings, and conclusions, or recommendations expressed in this material are those of the authors and do not necessarily reflect the views of the National Science Foundation.

Author Information Notes. Corresponding author (Edward G. Gillan, edward-gillan@uiowa.edu). The authors declare no competing financial interest. IL and AF performed all metal phosphide synthesis and conducted all product analyses; IL conducted all reported electrochemical experiments; IL, AF, and EG contributed to experimental designs; IL and EG contributed to manuscript preparation, revision, and creation of graphical and tabular content.

Supporting Information: Images of electrochemical cell and electrodes, additional product data, images, and summary tables (XRD, XPS, SEM, EDS), and HER electrocatalysis data for Ni-P phases, HER literature comparisons. This material is available free of charge *via* the Internet at http://pubs.acs.org.

REFERENCES

(1) Yue, M. L.; Lambert, H.; Pahon, E.; Roche, R.; Jemei, S.; Hissel, D. Hydrogen energy systems: A critical review of technologies, applications, trends and challenges. *Renew. Sust. Energ. Rev.* **2021**, *146*, 111180. DOI: 10.1016/j.rser.2021.111180.
(2) Christopher, K.; Dimitrios, R. A review on exergy comparison of hydrogen production methods from renewable energy sources. *Energy Environ. Sci.* **2012**, *5* (5), 6640-6651. DOI: 10.1039/c2ee01098d.
(3) Walter, M. G.; Warren, E. L.; McKone, J. R.; Boettcher, S. W.; Mi, Q.; Santori, E. A.; Lewis, N. S. Solar water splitting cells. *Chem. Rev.* **2010**, *110* (11), 6446-6473. DOI: 10.1021/cr1002326.
(4) Tee, S. Y.; Win, K. Y.; Teo, W. S.; Koh, L. D.; Liu, S.; Teng, C. P.; Han, M. Y. Recent Progress in Energy-Driven Water Splitting. *Adv. Sci.* **2017**, *4* (5), 1600337. DOI: 10.1002/advs.201600337.
(5) Zou, X.; Zhang, Y. Noble metal-free hydrogen evolution catalysts for water splitting. *Chem. Soc. Rev.* **2015**, *44* (15), 5148-5180. DOI: 10.1039/c4cs00448e.
(6) Roger, I.; Shipman, M. A.; Symes, M. D. Earth-abundant catalysts for electrochemical and photoelectrochemical water splitting. *Nat. Rev. Chem.* **2017**, *1* (1), 0003. DOI: 10.1038/s41570-016-0003.
(7) Anantharaj, S.; Ede, S. R.; Sakthikumar, K.; Karthick, K.; Mishra, S.; Kundu, S. Recent Trends and Perspectives in Electrochemical Water Splitting with an Emphasis on Sulfide, Selenide, and Phosphide Catalysts of Fe, Co, and Ni: A Review. *ACS Catal.* **2016**, *6* (12), 8069-8097. DOI: 10.1021/acscatal.6b02479.
(8) Carenco, S.; Portehault, D.; Boissiere, C.; Mezailles, N.; Sanchez, C. Nanoscaled metal borides and phosphides: recent developments and perspectives. *Chem. Rev.* **2013**, *113* (10), 7981-8065. DOI: 10.1021/cr400020d.
(9) Schmuecker, S. M.; Clouser, D.; Kraus, T. J.; Leonard, B. M. Synthesis of metastable chromium carbide nanomaterials and their electrocatalytic activity for the hydrogen evolution reaction. *Dalton Trans.* **2017**, *46* (39), 13524-13530. DOI: 10.1039/c7dt01404j.
(10) Chia, X.; Eng, A. Y.; Ambrosi, A.; Tan, S. M.; Pumera, M. Electrochemistry of Nanostructured Layered Transition-Metal Dichalcogenides. *Chem. Rev.* **2015**, *115* (21), 11941-11966. DOI: 10.1021/acs.chemrev.5b00287.
(11) Peng, X.; Pi, C. R.; Zhang, X. M.; Li, S.; Huo, K. F.; Chu, P. K. Recent progress of transition metal nitrides for efficient electrocatalytic water splitting. *Sustain. Energy Fuels* **2019**, *3* (2), 366-381. DOI: 10.1039/c8se00525g.
(12) Zhu, Y. L.; Lin, Q.; Zhong, Y. J.; Tahini, H. A.; Shao, Z. P.; Wang, H. T. Metal oxide-based materials as an emerging family of hydrogen evolution electrocatalysts. *Energy Environ. Sci.* **2020**, *13* (10), 3361-3392. DOI: 10.1039/d0ee02485f.

(13) Callejas, J. F.; Read, C. G.; Roske, C. W.; Lewis, N. S.; Schaak, R. E. Synthesis, Characterization, and Properties of Metal Phosphide Catalysts for the Hydrogen-Evolution Reaction. *Chem. Mater.* **2016**, *28* (17), 6017-6044. DOI: 10.1021/acs.chemmater.6b02148.
(14) Li, Y.; Dong, Z.; Jiao, L. Multifunctional Transition Metal-Based Phosphides in Energy-Related Electrocatalysis. *Adv. Energy Mater.* **2019**, *10* (11), 1902104. DOI: 10.1002/aenm.201902104.
(15) Shi, Y.; Zhang, B. Recent advances in transition metal phosphide nanomaterials: synthesis and applications in hydrogen evolution reaction. *Chem. Soc. Rev.* **2016**, *45* (6), 1529-1541. DOI: 10.1039/c5cs00434a.
(16) Weng, C. C.; Ren, J. T.; Yuan, Z. Y. Transition Metal Phosphide-Based Materials for Efficient Electrochemical Hydrogen Evolution: A Critical Review. *ChemSusChem* **2020**, *13* (13), 3357-3375. DOI: 10.1002/cssc.202000416.
(17) Von Schnering, H. G.; Hoenle, W. Chemistry and structural chemistry of phosphides and polyphosphides. 48. Bridging chasms with polyphosphides. *Chem. Rev.* **1988**, *88* (1), 243-273. DOI: 10.1021/cr00083a012.
(18) Ren, J.; Wang, J.-g.; Li, J.-f.; Li, Y.-w. Density functional theory study on crystal nickel phosphides. *J. Fuel Chem. Technol.* **2007**, *35* (4), 458-464. DOI: 10.1016/s1872-5813(07)60029-2.
(19) Zhao, D. D.; Zhou, L. C.; Du, Y.; Wang, A. J.; Peng, Y. B.; Kong, Y.; Sha, C. S.; Ouyang, Y. F.; Zhang, W. Q. Structure, elastic and thermodynamic properties of the Ni-P system from first-principles calculations. *Calphad* **2011**, *35* (3), 284-291. DOI: 10.1016/j.calphad.2011.03.002.
(20) Okamoto, H. Ni-P (Nickel-Phosphorus). *J Phase Equilib Diff* **2010**, *31* (2), 200-201. DOI: 10.1007/s11669-010-9664-1.
(21) Oyama, S. T. Novel catalysts for advanced hydroprocessing: transition metal phosphides. *J. Catal.* **2003**, *216* (1-2), 343-352. DOI: 10.1016/S0021-9517(02)00069-6.
(22) Liu, P.; Rodriguez, J. A. Catalysts for hydrogen evolution from the [NiFe] hydrogenase to the Ni2P(001) surface: the importance of ensemble effect. *J. Am. Chem. Soc.* **2005**, *127* (42), 14871-14878. DOI: 10.1021/ja0540019.
(23) Popczun, E. J.; McKone, J. R.; Read, C. G.; Biacchi, A. J.; Wiltrout, A. M.; Lewis, N. S.; Schaak, R. E. Nanostructured nickel phosphide as an electrocatalyst for the hydrogen evolution reaction. *J. Am. Chem. Soc.* **2013**, *135* (25), 9267-9270. DOI: 10.1021/ja403440e.
(24) Zheng, H.; Huang, X.; Wu, Z.; Gao, H.; Dong, W.; Wang, G. Controlled Synthesis of 3D Flower-like Ni(2) P Composed of Mesoporous Nanoplates for Overall Water Splitting. *Chem. Asian J.* **2017**, *12* (22), 2956-2961. DOI: 10.1002/asia.201701255.
(25) Zhou, Z.; Wei, L.; Wang, Y. Q.; Karahan, H. E.; Chen, Z. B.; Lei, Y. J.; Chen, X. C.; Zhai, S. L.; Liao, X. Z.; Chen, Y. Hydrogen evolution reaction activity of nickel phosphide is highly sensitive to electrolyte pH. *J. Mater. Chem. A* **2017**, *5* (38), 20390-20397. DOI: 10.1039/c7ta06000a.
(26) Huang, Z.; Chen, Z.; Chen, Z.; Lv, C.; Meng, H.; Zhang, C. Ni12P5 Nanoparticles as an Efficient Catalyst for Hydrogen Generation via Electrolysis and Photoelectrolysis. *ACS Nano* **2014**, *8* (8), 8121-8129. DOI: 10.1021/nn5022204.
(27) Wang, C.; Ding, T.; Sun, Y.; Zhou, X.; Liu, Y.; Yang, Q. Ni12P5 nanoparticles decorated on carbon nanotubes with enhanced electrocatalytic and lithium storage properties. *Nanoscale* **2015**, *7* (45), 19241-19249, 10.1039/C5NR05432J. DOI: 10.1039/C5NR05432J.
(28) Pan, Y.; Liu, Y. R.; Zhao, J. C.; Yang, K.; Liang, J. L.; Liu, D. D.; Hu, W. H.; Liu, D. P.; Liu, Y. Q.; Liu, C. G. Monodispersed nickel phosphide nanocrystals with different phases: synthesis, characterization and electrocatalytic properties for hydrogen evolution. *J. Mater. Chem. A* **2015**, *3* (4), 1656-1665. DOI: 10.1039/c4ta04867a.
(29) Kucernak, A. R. J.; Sundaram, V. N. N. Nickel phosphide: the effect of phosphorus content on hydrogen evolution activity and corrosion resistance in acidic medium. *J. Mater. Chem. A* **2014**, *2* (41), 17435-17445. DOI: 10.1039/c4ta03468f.
(30) Laursen, A. B.; Patraju, K. R.; Whitaker, M. J.; Retuerto, M.; Sarkar, T.; Yao, N.; Ramanujachary, K. V.; Greenblatt, M.; Dismukes, G. C. Nanocrystalline Ni5P4: a hydrogen evolution electrocatalyst of

exceptional efficiency in both alkaline and acidic media. *Energy Environ. Sci.* **2015**, *8* (3), 1027-1034. DOI: 10.1039/c4ee02940b.
(31) Lai, C. G.; Liu, X. B.; Deng, Y. Q.; Yang, H.; Jiang, H. H.; Xiao, Z. C.; Liang, T. X. Rice-shape nanocrystalline Ni5P4: A promising bifunctional electrocatalyst for hydrogen evolution reaction and oxygen evolution reaction. *Inorg. Chem. Commun.* **2018**, *97*, 98-102. DOI: 10.1016/j.inoche.2018.09.024.
(32) Wexler, R. B.; Martirez, J. M. P.; Rappe, A. M. Active Role of Phosphorus in the Hydrogen Evolving Activity of Nickel Phosphide (0001) Surfaces. *ACS Catal.* **2017**, *7* (11), 7718-7725. DOI: 10.1021/acscatal.7b02761.
(33) Wexler, R. B.; Martirez, J. M. P.; Rappe, A. M. Stable Phosphorus-Enriched (0001) Surfaces of Nickel Phosphides. *Chem. Mater.* **2016**, *28* (15), 5365-5372. DOI: 10.1021/acs.chemmater.6b01437.
(34) Kim, J. Y.; Park, H.; Joo, W.; Nam, D. H.; Lee, S.; Kim, H. G.; Ahn, I. K.; Kang, H. Y.; Lee, G. B.; Jung, I. H.; Kim, M. Y.; Lee, G. D.; Joo, Y. C. Predictive fabrication of Ni phosphide embedded in carbon nanofibers as active and stable electrocatalysts. *J. Mater. Chem. A* **2019**, *7* (13), 7451-7458. DOI: 10.1039/c9ta00455f.
(35) Jiang, P.; Liu, Q.; Sun, X. NiP2 nanosheet arrays supported on carbon cloth: an efficient 3D hydrogen evolution cathode in both acidic and alkaline solutions. *Nanoscale* **2014**, *6* (22), 13440-13445. DOI: 10.1039/c4nr04866k.
(36) Owens-Baird, B.; Xu, J. Y.; Petrovykh, D. Y.; Bondarchuk, O.; Ziouani, Y.; Gonzalez-Ballesteros, N.; Yox, P.; Sapountzi, F. M.; Niemantsverdriet, H.; Kolen'ko, Y. V.; Kovnir, K. NiP2: A Story of Two Divergent Polymorphic Multifunctional Materials. *Mater. Chem.* **2019**, *31* (9), 3407-3418. DOI: 10.1021/acs.chemmater.9b00565.
(37) Owens-Baird, B.; Sousa, J. P. S.; Ziouani, Y.; Petrovykh, D. Y.; Zarkevich, N. A.; Johnson, D. D.; Kolen'ko, Y. V.; Kovnir, K. Crystallographic facet selective HER catalysis: exemplified in FeP and NiP2 single crystals. *Chem. Sci.* **2020**, *11* (19), 5007-5016. DOI: 10.1039/d0sc00676a.
(38) Coleman, N., Jr.; Lovander, M. D.; Leddy, J.; Gillan, E. G. Phosphorus-Rich Metal Phosphides: Direct and Tin Flux-Assisted Synthesis and Evaluation as Hydrogen Evolution Electrocatalysts. *Inorg. Chem.* **2019**, *58* (8), 5013-5024. DOI: 10.1021/acs.inorgchem.9b00032.
(39) Ma, G.; Du, X.; Zhang, X. Controlled phosphating: a novel strategy toward NiP(3)@CeO(2) interface engineering for efficient oxygen evolution electrocatalysis. *Dalton Trans.* **2020**, *49* (36), 12581-12585. DOI: 10.1039/d0dt02599b.
(40) Fullenwarth, J.; Darwiche, A.; Soares, A.; Donnadieu, B.; Monconduit, L. NiP3: a promising negative electrode for Li- and Na-ion batteries. *J. Mater. Chem. A* **2014**, *2* (7), 2050-2059. DOI: 10.1039/c3ta13976j.
(41) Ihsan-Ul-Haq, M.; Huang, H.; Cui, J.; Yao, S. S.; Wu, J. X.; Chong, W. G.; Huang, B. L.; Kim, J. K. Chemical interactions between red P and functional groups in NiP3/CNT composite anodes for enhanced sodium storage. *J. Mater. Chem. A* **2018**, *6* (41), 20184-20194, 10.1039/C8TA06841K. DOI: 10.1039/c8ta06841k.
(42) Lou, P.; Cui, Z.; Jia, Z.; Sun, J.; Tan, Y.; Guo, X. Monodispersed Carbon-Coated Cubic NiP(2) Nanoparticles Anchored on Carbon Nanotubes as Ultra-Long-Life Anodes for Reversible Lithium Storage. *ACS Nano* **2017**, *11* (4), 3705-3715. DOI: 10.1021/acsnano.6b08223.
(43) Boyanov, S.; Gillot, F.; Monconduit, L. The electrochemical reactivity of the NiP3 skutterudite-type phase with lithium. *Ionics* **2008**, *14* (2), 125-130. DOI: 10.1007/s11581-007-0190-z.
(44) Boda, G.; Stenström, B.; Sagredo, V.; Beckman, O.; Carlsson, B.; Rundqvist, S. Magnetic and Electric Properties of FeP2Single Crystals. *Phys. Scr.* **1971**, *4* (3), 132-134. DOI: 10.1088/0031-8949/4/3/010.
(45) Lee, C. H.; Kito, H.; Ihara, H.; Akita, K.; Yanase, N.; Sekine, C.; Shirotani, I. Single crystal growth of skutterudite CoP3 under high pressure. *J. Cryst. Growth* **2004**, *263* (1-4), 358-362. DOI: 10.1016/j.jcrysgro.2003.11.111.
(46) Yuan, Q. Y.; Ariga, H.; Asakura, K. An Investigation of Ni2P Single Crystal Surfaces: Structure, Electronic State and Reactivity. *Top Catal* **2015**, *58* (4-6), 194-200. DOI: 10.1007/s11244-015-0360-6.

(47) Xie, Y.; Su, H. L.; Qian, X. F.; Liu, X. M.; Qian, Y. T. A Mild One-Step Solvothermal Route to Metal Phosphides (Metal=Co, Ni, Cu). *J. Solid State Chem.* **2000**, *149* (1), 88-91. DOI: 10.1006/jssc.1999.8499.
(48) Liu, J. W.; Chen, X. Y.; Shao, M. W.; An, C. H.; Yu, W. C.; Qian, Y. T. Surfactant-aided solvothermal synthesis of dinickel phosphide nanocrystallites using red phosphorus as starting materials. *J. Cryst. Growth* **2003**, *252* (1-3), 297-301. DOI: 10.1016/S0022-0248(03)00939-4.
(49) Henkes, A. E.; Schaak, R. E. Trioctylphosphine: A general phosphorus source for the low-temperature conversion of metals into metal phosphides. *Chem. Mater.* **2007**, *19* (17), 4234-4242. DOI: 10.1021/cm071021w.
(50) Henkes, A. E.; Vasquez, Y.; Schaak, R. E. Converting metals into phosphides: a general strategy for the synthesis of metal phosphide nanocrystals. *J. Am. Chem. Soc.* **2007**, *129* (7), 1896-1897. DOI: 10.1021/ja068502l.
(51) Barry, B. M.; Gillan, E. G. Low-temperature solvothermal synthesis of phosphorus-rich transition-metal phosphides. *Chem. Mater.* **2008**, *20* (8), 2618-2620. DOI: 10.1021/cm703095z.
(52) Jiang, J.; Wang, C. D.; Zhang, J. J.; Wang, W. L.; Zhou, X. L.; Pan, B. C.; Tang, K. B.; Zuo, J.; Yang, Q. Synthesis of FeP2/C nanohybrids and their performance for hydrogen evolution reaction. *J. Mater. Chem. A* **2015**, *3* (2), 499-503. DOI: 10.1039/c4ta04758c.
(53) Muthuswamy, E.; Savithra, G. H.; Brock, S. L. Synthetic levers enabling independent control of phase, size, and morphology in nickel phosphide nanoparticles. *ACS Nano* **2011**, *5* (3), 2402-2411. DOI: 10.1021/nn1033357.
(54) Su, J. Z.; Zhou, J. L.; Wang, L.; Liu, C.; Chen, Y. B. Synthesis and application of transition metal phosphides as electrocatalyst for water splitting. *Sci. Bull.* **2017**, *62* (9), 633-644. DOI: 10.1016/j.scib.2016.12.011.
(55) Hu, C.; Lv, C.; Liu, S.; Shi, Y.; Song, J. F.; Zhang, Z.; Cai, J. G.; Watanabe, A. Nickel Phosphide Electrocatalysts for Hydrogen Evolution Reaction. *Catalysts* **2020**, *10* (2), 188. DOI: 10.3390/catal10020188.
(56) Gillot, F.; Boyanov, S.; Dupont, L.; Doublet, M. L.; Morcrette, M.; Monconduit, L.; Tarascon, J. M. Electrochemical Reactivity and Design of NiP2 Negative Electrodes for Secondary Li-Ion Batteries. *Chem. Mater.* **2005**, *17* (25), 6327-6337. DOI: 10.1021/cm051574b.
(57) Schipper, D. E.; Zhao, Z. H.; Thirumalai, H.; Leitner, A. P.; Donaldson, S. L.; Kumar, A.; Qin, F.; Wang, Z. M.; Grabow, L. C.; Bao, J. M.; Whitmire, K. H. Effects of Catalyst Phase on the Hydrogen Evolution Reaction of Water Splitting: Preparation of Phase-Pure Films of FeP, Fe2P, and Fe3P and Their Relative Catalytic Activities. *Chem. Mater.* **2018**, *30* (10), 3588-3598. DOI: 10.1021/acs.chemmater.8b01624.
(58) Barry, B. M.; Gillan, E. G. A General and Flexible Synthesis of Transition-Metal Polyphosphides via PCl3 Elimination. *Chem. Mater.* **2009**, *21* (19), 4454-4461. DOI: 10.1021/cm9010663.
(59) Abeysinghe, J. P.; Kolln, A. F.; Gillan, E. G. Rapid and Energetic Solid-State Metathesis Reactions for Iron, Cobalt, and Nickel Boride Formation and Their Investigation as Bifunctional Water Splitting Electrocatalysts. *ACS Mater. Au* **2022**, *2* (4), 489-504. DOI: 10.1021/acsmaterialsau.1c00079.
(60) Coleman, N.; Liyanage, I. A.; Lovander, M. D.; Leddy, J.; Gillan, E. G. Facile Solvent-Free Synthesis of Metal Thiophosphates and Their Examination as Hydrogen Evolution Electrocatalysts. *Molecules* **2022**, *27* (16). DOI: 10.3390/molecules27165053.
(61) Almeida, C. M. V. B.; Giannetti, B. F. A new and practical carbon paste electrode for insoluble and ground samples. *Electrochem. Commun.* **2002**, *4* (12), 985-988. DOI: 10.1016/S1388-2481(02)00511-8.
(62) Eghbalnia, M.; Dixon, D. G. Electrochemical study of leached chalcopyrite using solid paraffin-based carbon paste electrodes. *Hydrometallurgy* **2011**, *110* (1-4), 1-12. DOI: 10.1016/j.hydromet.2011.07.009.
(63) Long, J. W.; Ayers, K. E.; Rolison, D. R. Electrochemical characterization of high-surface-area catalysts and other nanoscale electroactive materials at sticky-carbon electrodes. *J. Electroanal. Chem.* **2002**, *522* (1), 58-65. DOI: 10.1016/S0022-0728(02)00653-8.

(64) Anantharaj, S.; Ede, S. R.; Karthick, K.; Sankar, S. S.; Sangeetha, K.; Karthik, P. E.; Kundu, S. Precision and correctness in the evaluation of electrocatalytic water splitting: revisiting activity parameters with a critical assessment. *Energy Environ. Sci.* **2018**, *11* (4), 744-771. DOI: 10.1039/c7ee03457a.
(65) Chen, Z.; Dinh, H. N.; Miller, E. *Photoelectrochemical Water Splitting: Standards, Experimental Methods, and Protocols*; Springer, 2013. DOI: 10.1007/978-1-4614-8298-7.
(66) Kibsgaard, J.; Tsai, C.; Chan, K.; Benck, J. D.; Norskov, J. K.; Abild-Pedersen, F.; Jaramillo, T. F. Designing an improved transition metal phosphide catalyst for hydrogen evolution using experimental and theoretical trends. *Energy & Environmental Science* **2015**, *8* (10), 3022-3029. DOI: 10.1039/c5ee02179k.
(67) Donohue, P. C.; Bither, T. A.; Young, H. S. High-Pressure Synthesis of Pyrite-Type Nickel Diphosphide and Nickel Diarsenide. *Inorg. Chem.* **1968**, *7* (5), 998-&. DOI: DOI 10.1021/ic50063a031.
(68) Jeitschko, W.; Foecker, A. J.; Paschke, D.; Dewalsky, M. V.; Evers, C. B. H.; Kunnen, B.; Lang, A.; Kotzyba, G.; Rodewald, U. C.; Moller, M. H. Crystal structure and properties of some filled and unfilled skutterudites: GdFe4P12, SmFe4P12, NdFe4As12, Eu0.54Co4Sb12, Fe0.5Ni0.5P3, CoP3, and NiP3. *Z Anorg Allg Chem* **2000**, *626* (5), 1112-1120. DOI: 10.1002/(Sici)1521-3749(200005)626:5<1112::Aid-Zaac1112>3.0.Co;2-E.
(69) Kanatzidis, M. G.; Pottgen, R.; Jeitschko, W. The metal flux: a preparative tool for the exploration of intermetallic compounds. *Angew. Chem. Int. Ed.* **2005**, *44* (43), 6996-7023. DOI: 10.1002/anie.200462170.
(70) Odile, J. P.; Soled, S.; Castro, C. A.; Wold, A. Crystal growth and characterization of the transition-metal phosphides copper diphosphide, nickel diphosphide, and rhodium triphosphide. *Inorg. Chem.* **2002**, *17* (2), 283-286. DOI: 10.1021/ic50180a018.
(71) Llunell, M.; Alemany, P.; Alvarez, S.; Zhukov, V. P.; Vernes, A. Electronic structure and bonding in skutterudite-type phosphides. *Phys. Rev. B Condens. Matter* **1996**, *53* (16), 10605-10609. DOI: 10.1103/physrevb.53.10605.
(72) Pan, Y.; Hu, W. H.; Liu, D. P.; Liu, Y. Q.; Liu, C. G. Carbon nanotubes decorated with nickel phosphide nanoparticles as efficient nanohybrid electrocatalysts for the hydrogen evolution reaction. *J. Mater. Chem. A* **2015**, *3* (24), 13087-13094. DOI: 10.1039/c5ta02128f.
(73) Yu, L.; Ren, Z. Systematic study of the influence of iR compensation on water electrolysis. *Mater. Today Phys.* **2020**, *14*. DOI: 10.1016/j.mtphys.2020.100253.
(74) Chen, R.; Yang, C. J.; Cai, W. Z.; Wang, H. Y.; Miao, J. W.; Zhang, L. P.; Chen, S. L.; Liu, B. Use of Platinum as the Counter Electrode to Study the Activity of Nonprecious Metal Catalysts for the Hydrogen Evolution Reaction. *ACS Energy Lett.* **2017**, *2* (5), 1070-1075. DOI: 10.1021/acsenergylett.7b00219.
(75) Shinagawa, T.; Garcia-Esparza, A. T.; Takanabe, K. Insight on Tafel slopes from a microkinetic analysis of aqueous electrocatalysis for energy conversion. *Sci. Rep.* **2015**, *5* (1), 13801. DOI: 10.1038/srep13801.
(76) Owens-Baird, B.; Kolen'ko, Y. V.; Kovnir, K. Structure-Activity Relationships for Pt-Free Metal Phosphide Hydrogen Evolution Electrocatalysts. *Chem. Eur. J.* **2018**, *24* (29), 7298-7311. DOI: 10.1002/chem.201705322 (acccessed 2022/10/27).
(77) Babizhetskyy, V.; Kotur, B.; Oryshchyn, S.; Zheng, C.; Kneidinger, F.; Leber, L.; Simson, C.; Bauer, E.; Michor, H. Crystal and electronic structure and physical properties of Ni5P4. *Solid State Commun.* **2013**, *164*, 1-5. DOI: 10.1016/j.ssc.2013.03.022.
(78) Zhang, C. N.; Yang, S. K.; Rao, D. W. Theoretical study the component and facet dependence of HER performance on nickel phosphides surfaces. *Int. J. Hydrog. Energy* **2022**, *47* (5), 2992-3000. DOI: 10.1016/j.ijhydene.2021.10.254.
(79) Ooka, H.; Huang, J.; Exner, K. S. The Sabatier Principle in Electrocatalysis: Basics, Limitations, and Extensions. *Front. Energy Res.* **2021**, *9*. DOI: 10.3389/fenrg.2021.654460.

For Table of Contents Only

Table of Contents Graphic

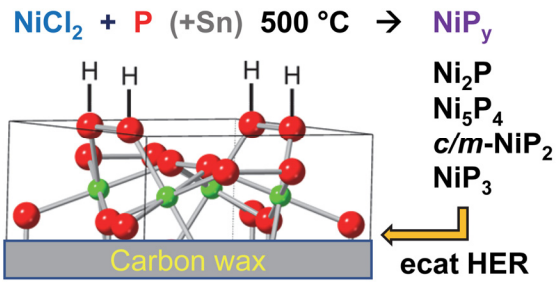

TOC synopsis

Tunable syntheses for a range of crystalline metal-rich to phosphorus-rich nickel phosphides are desired for comparable hydrogen evolution reaction (HER) studies. This report details the solvent-free, direct and tin-flux assisted synthesis of crystalline nickel phosphides from $NiCl_2$ and phosphorus at 500 °C, ranging from nickel-rich (Ni_2P, Ni_5P_4) to phosphorus-rich (NiP_2 and NiP_3) compositions. Synthetic mechanistic studies of tin influence on Ni-P growth are described and these Ni-P structures as comparatively examined as HER electrocatalysts.

Supporting Information for:

Tunable Synthesis of Metal-Rich and Phosphorus-Rich Nickel Phosphides and Their Comparative Evaluation as Hydrogen Evolution Electrocatalysts

Ishanka A. Liyanage, Ashley Flores, Edward G. Gillan*
University of Iowa, Department of Chemistry, Iowa City, Iowa 52242 USA

E-mail: edward-gillan@uiowa.edu
ORCID (Edward G. Gillan): 0000-0002-2047-0929
ORCID (Ishanka A. Liyanage) 0000-0003-4814-0099

Table of Contents (Tables and Figures are listed in the order they appear in the main text)

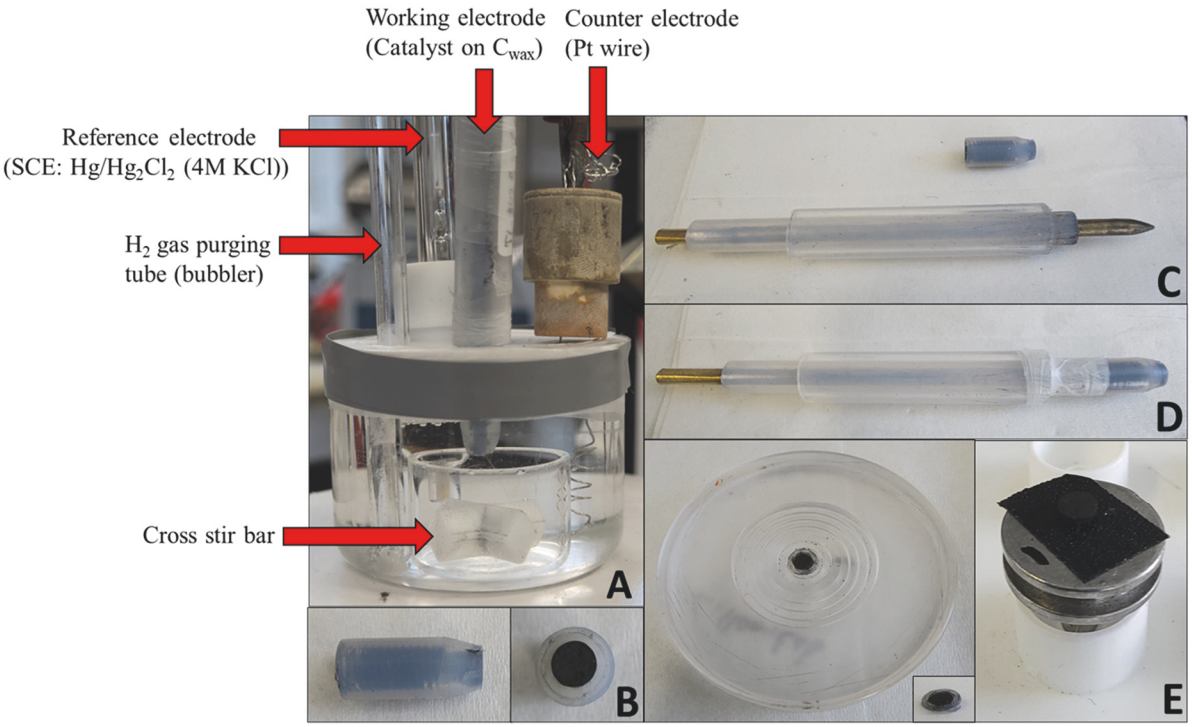

Figure S1. Images of electrochemical cell and working electrode (A) Three electrode, single compartment cell (B) coned, C_{wax} electrode tip in different geometries (C) disassembled C_{wax} electrode tip + brass current collector, (D) assembled C_{wax} working electrode (E) cut slice C_{wax} tip geometries for post electrochemical XRD and SEM-EDS analysis.

Direct and tin-flux assisted reactions enthalpy calculations. Two examples of a thermochemical ΔH_{rxn} calculation using Hess's Law for direct and tin-flux assisted $NiCl_2$/P reactions are shown below.

	$NiCl_2$	+	8/3 P	→	NiP_2	+	2/3 PCl_3
ΔH_f(kJ/mol)	-305.4		0		-108		2/3 × -320.9
ΔH_{rxn} (kJ/mol Ni)	$= \Sigma\Delta H_f$(products) - $\Sigma\Delta H_f$ (reactants) = -16.5						

	$NiCl_2$	+	5 P	+	5 Sn	→	NiP_3	+	$SnCl_2$	+	2 P	+	4 Sn
ΔH_f(kJ/mol)	-305.4		0		0		-157.7		-330.9		0		0
ΔH_{rxn} (kJ/mol Ni)	$= \Sigma\Delta H_f$(products) - $\Sigma\Delta H_f$ (reactants) = -183.2												

Table S1. Thermochemical data for direct and tin flux assisted synthesis of nickel phosphides.

Nickel phosphide	ΔH_f (kJ/mol of Ni_xP_y)	Ref.	ΔH_f(kJ/mol of Ni)	ΔH_{rxn} (kJ/mol of Ni) for PCl_3 byproduct	ΔH_{rxn} (kJ/mol of Ni) for $SnCl_2$ byproduct
Ni_2P	-185	1	-93	-1	-
Ni_5P_4	-414	2	-83	-6	-
c-NiP_2	-108	3	-108	-17	-
m-NiP_2	-129	4	-129	-	-155
NiP_3	-158	4	-158	-	-183

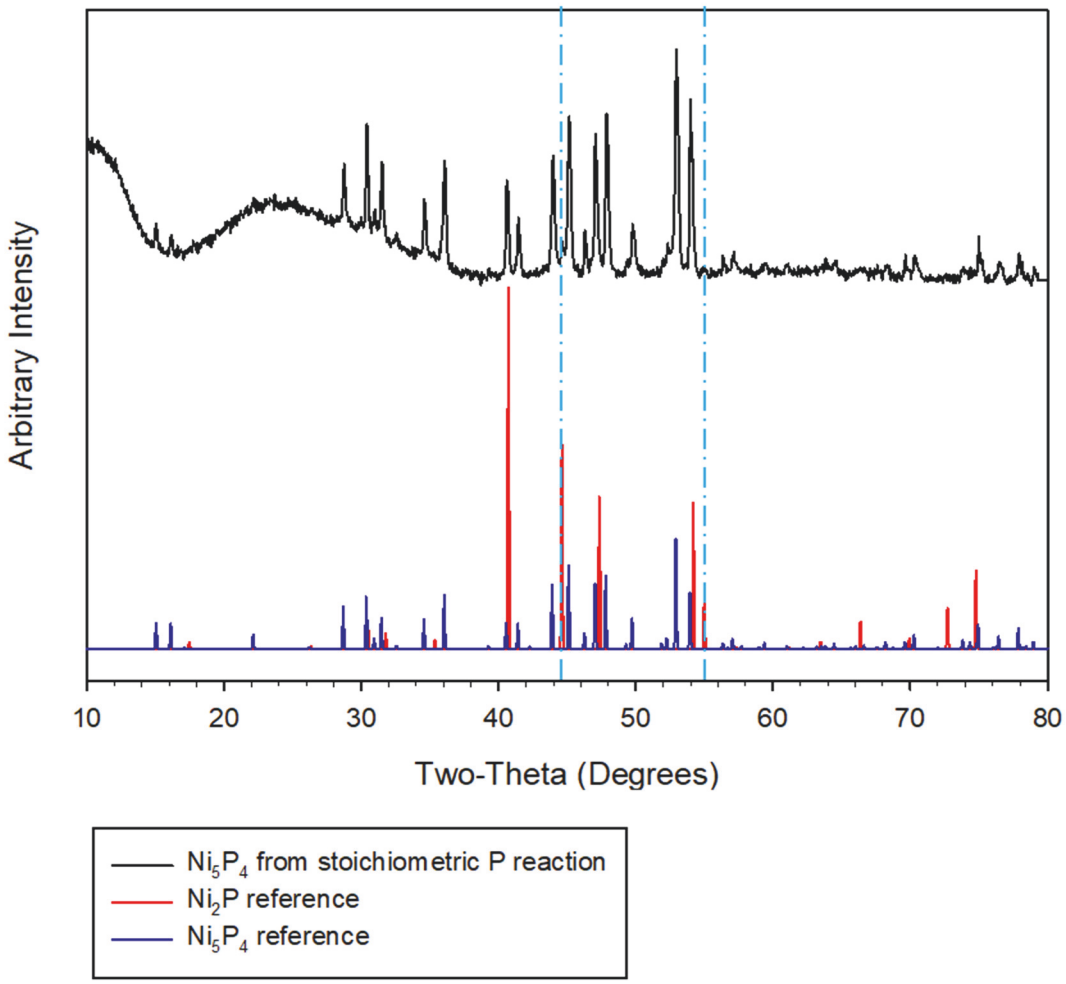

Figure S2. XRD results from Ni_5P_4 targeted stoichiometric direct $NiCl_2$/P reaction. Dashed lines show some non-overlapping peaks of Ni_2P and Ni_5P_4.

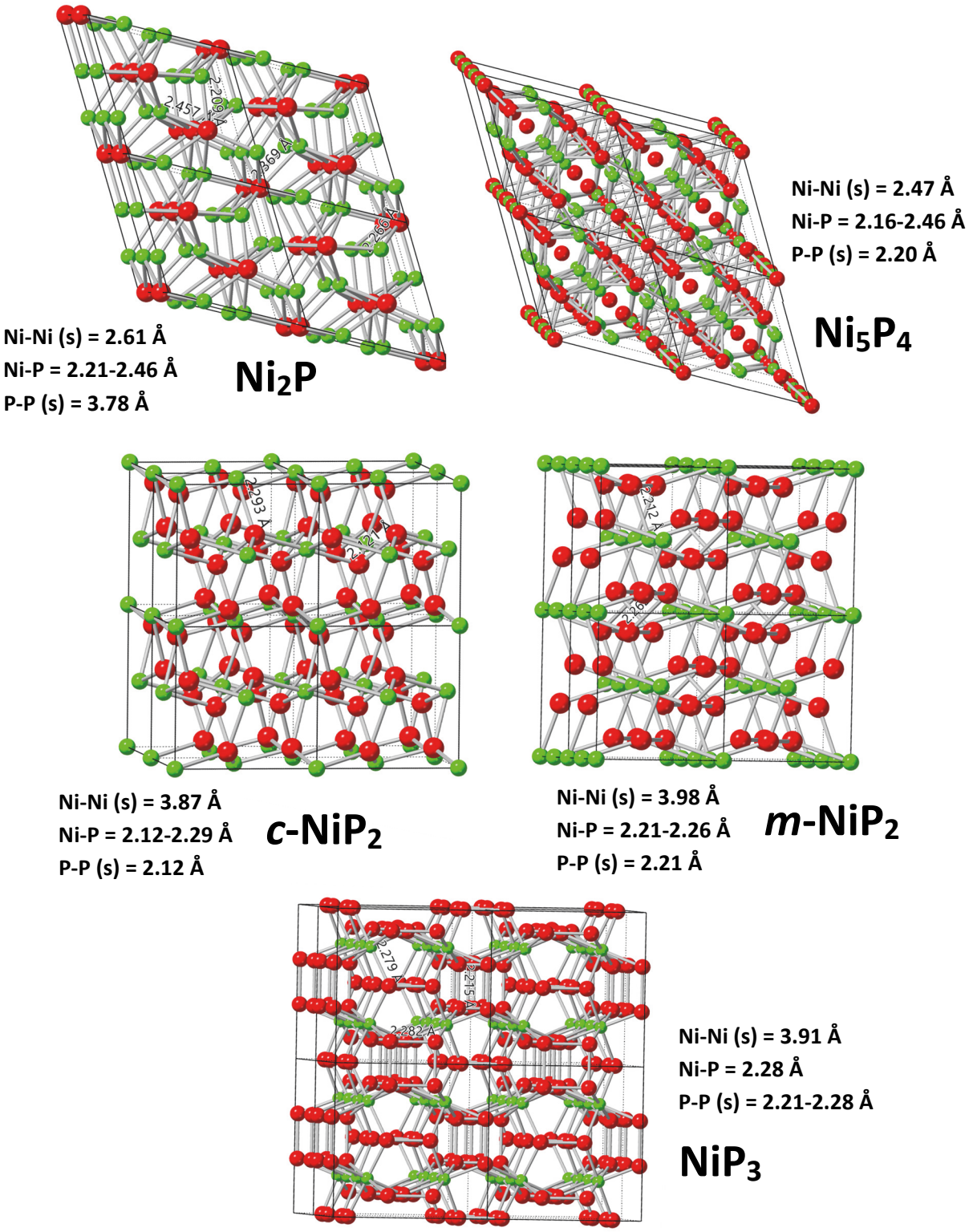

Figure S3. Crystal structure- representations of nickel phosphides [Hexagonal Ni_2P – P-62m (189), hexagonal Ni_5P_4 – P63mc (186), cubic NiP_2 – Pa-3 (205), monoclinic NiP_2 – C2/c (15), cubic NiP_3 – Im-3 (204)]. Only Ni-P bonds are shown in the structures and the atoms for Ni and P are shown in green and red respectively. (s) denotes the shortest bond.

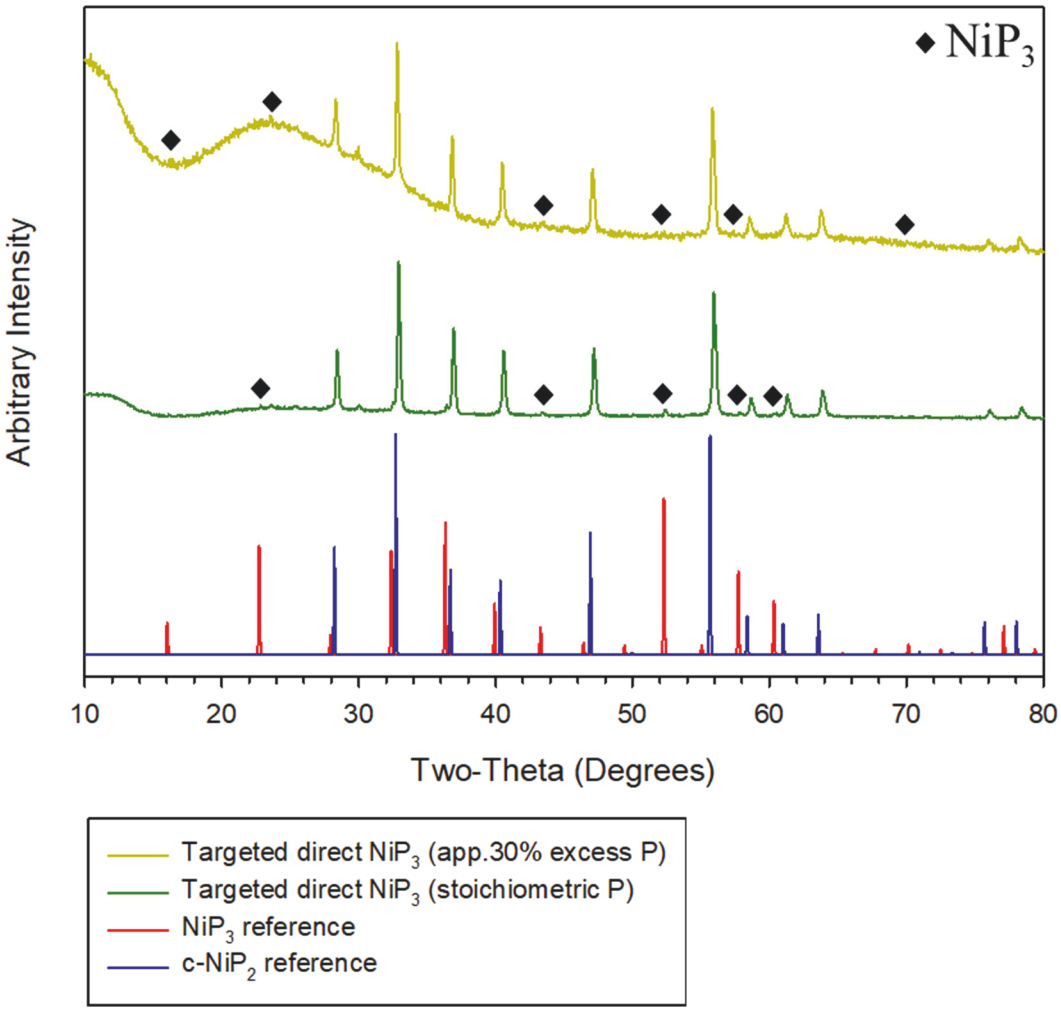

Figure S4. XRD results for targeted direct $NiCl_2$/P synthesis of NiP_3 using stoichiometric and app. 30% excess amounts of P. Diamond symbols identify some small peaks for NiP_3.

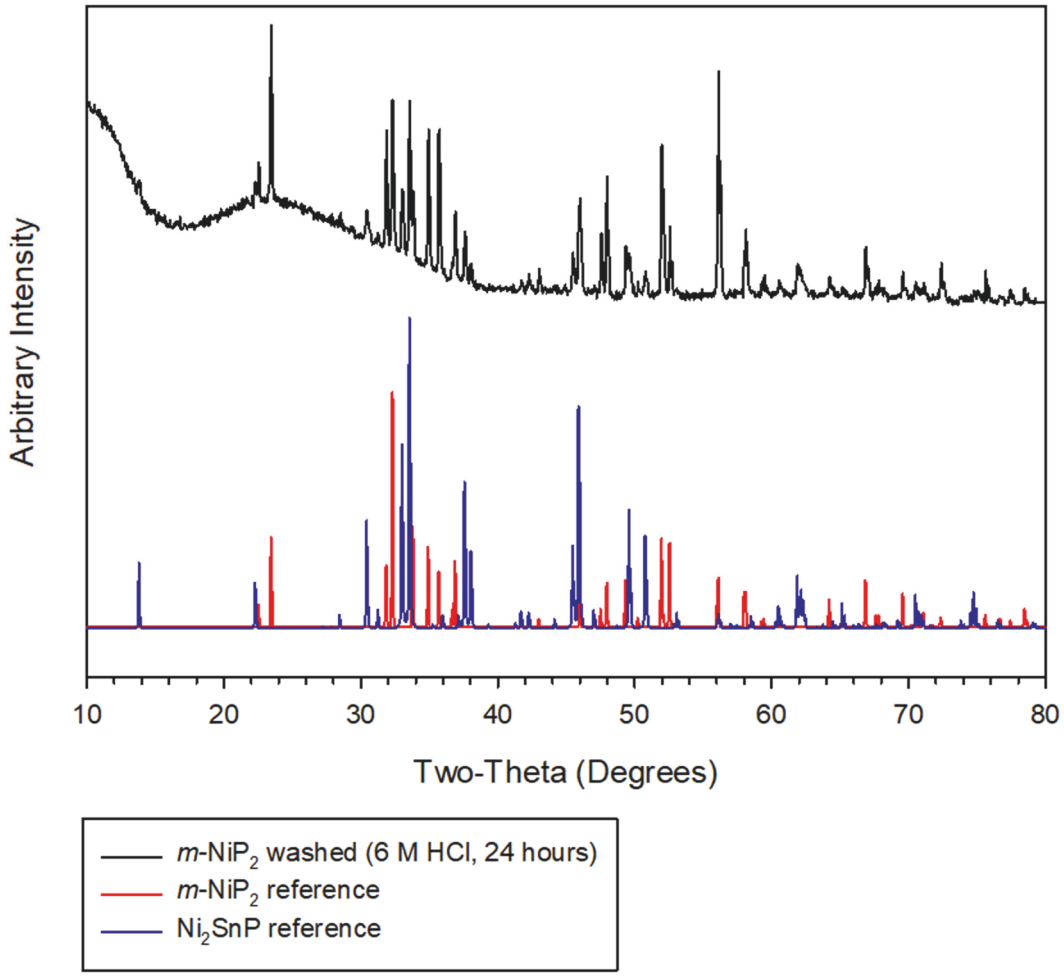

Figure S5. XRD results of *m*-NiP_2 product washed in 6 M HCl for 24 hours.

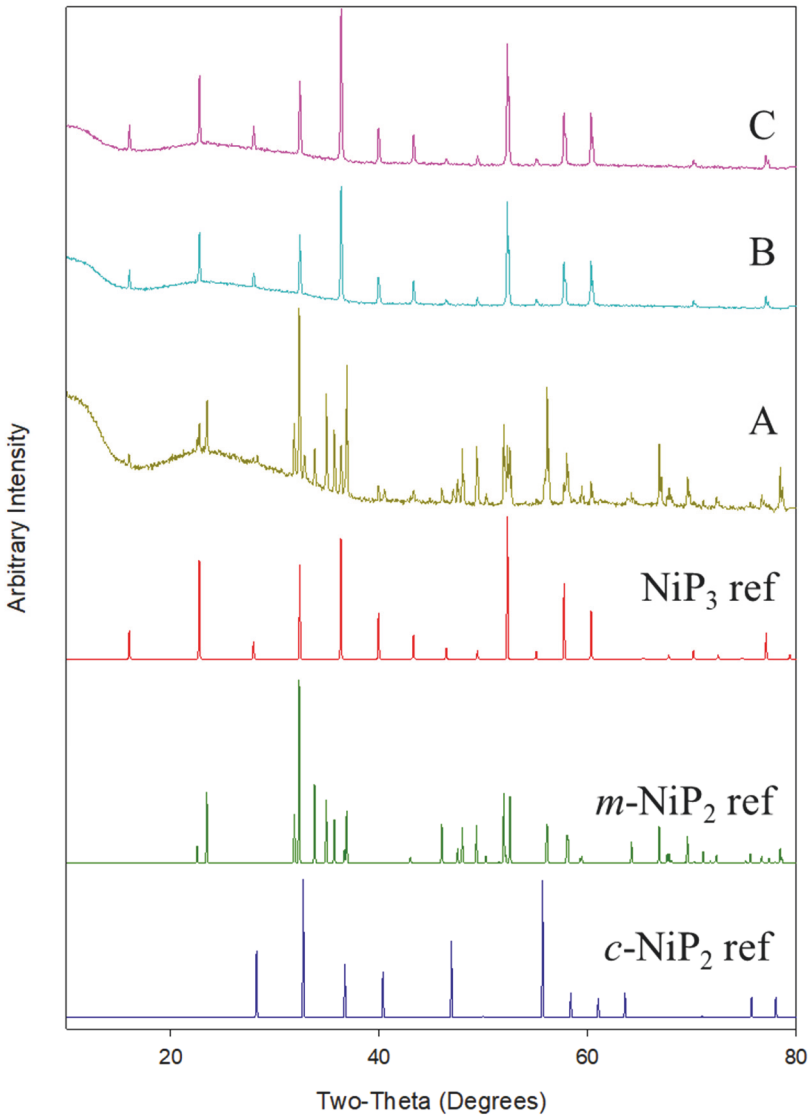

Figure S6. XRD results for targeted NiP_3 from tin flux assisted reactions using $NiCl_2$/P/Sn molar ratios of (A) 1/3/5 (B) 1/4/2 (C) 1/7/5.

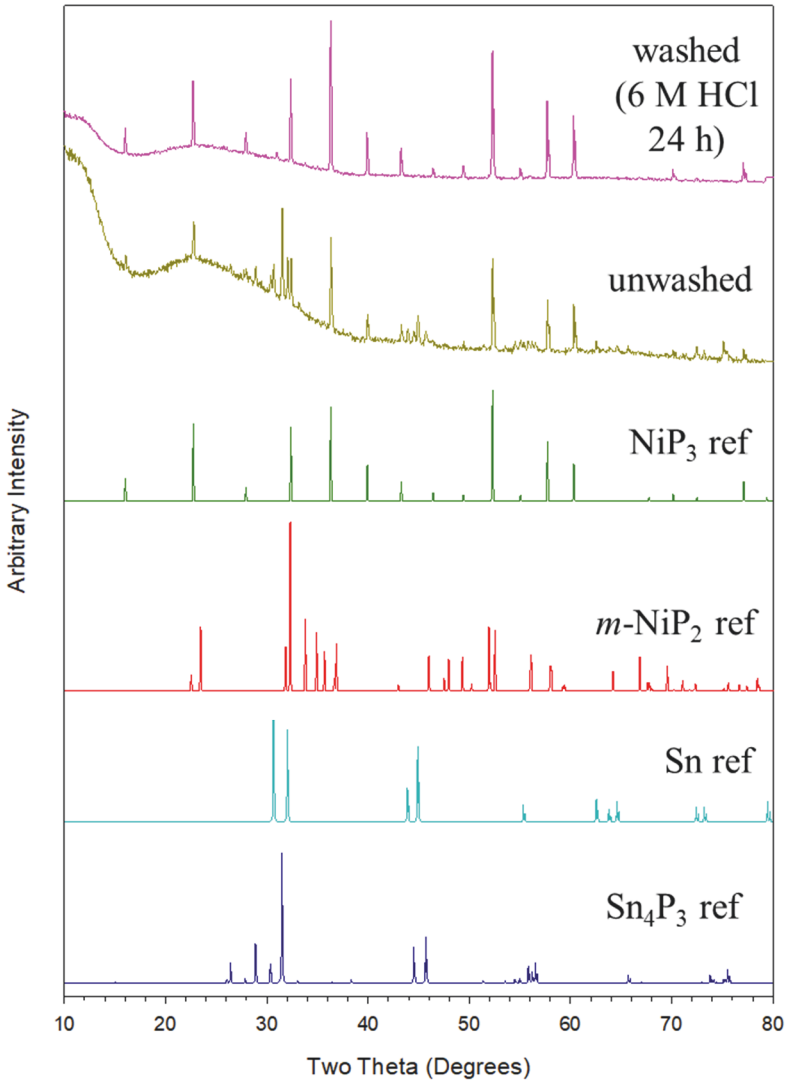

Figure S7. XRD results of unwashed and washed NiP_3 from tin flux assisted reaction using $NiCl_2$/P/Sn (1/5/5).

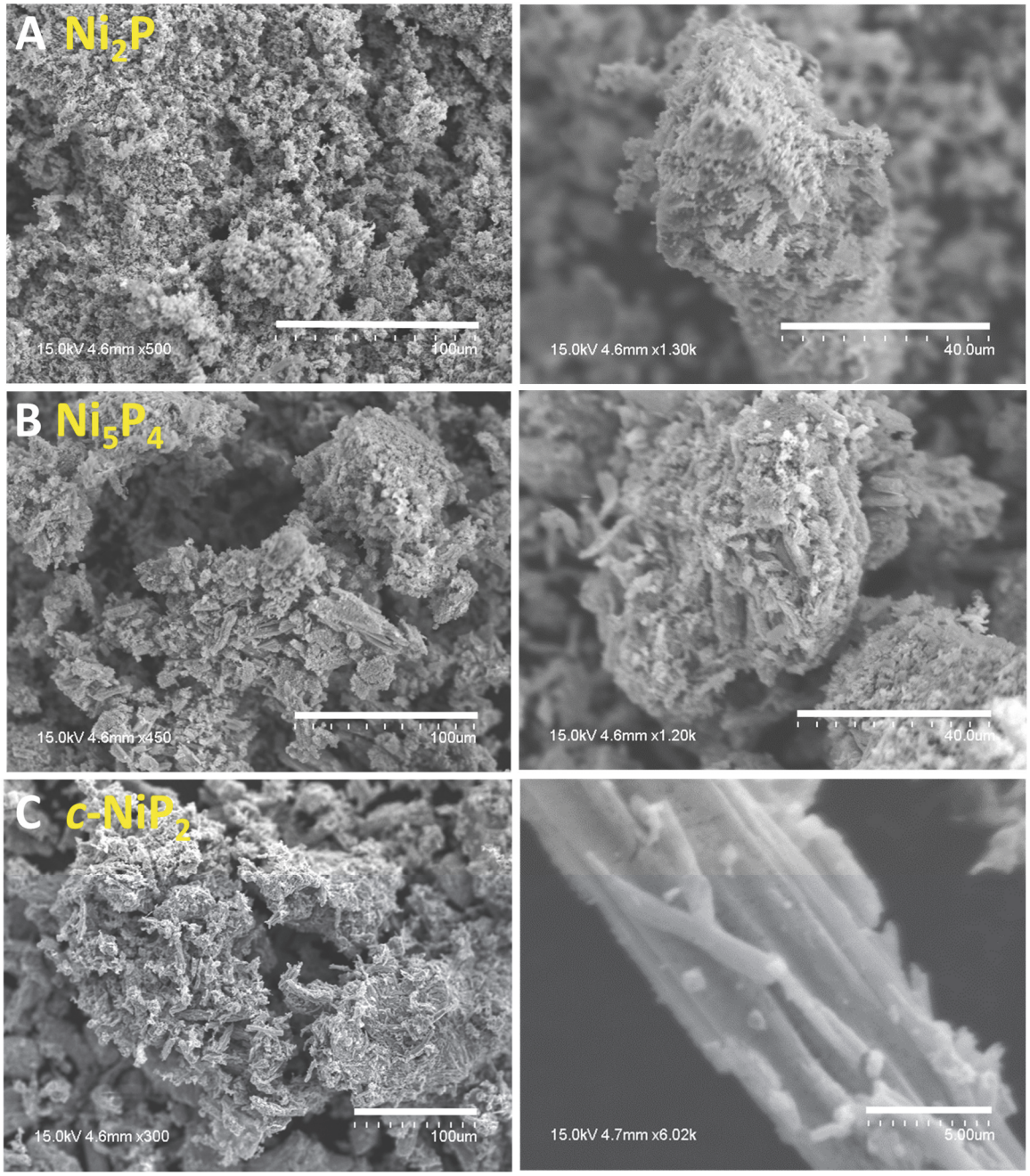

Figure S8. Scanning electron microscopy (SEM) comparison of particle sizes and morphologies obtained from direct reactions producing (A) Ni_2P (B) Ni_5P_4 (C) *c*-NiP_2. The left and right columns show images at low and high magnifications respectively. The lengths of scale bars (left, right) are (A) 100 µm, 40 µm (B) 100 µm, 40 µm (C) 100 µm, 5 µm respectively.

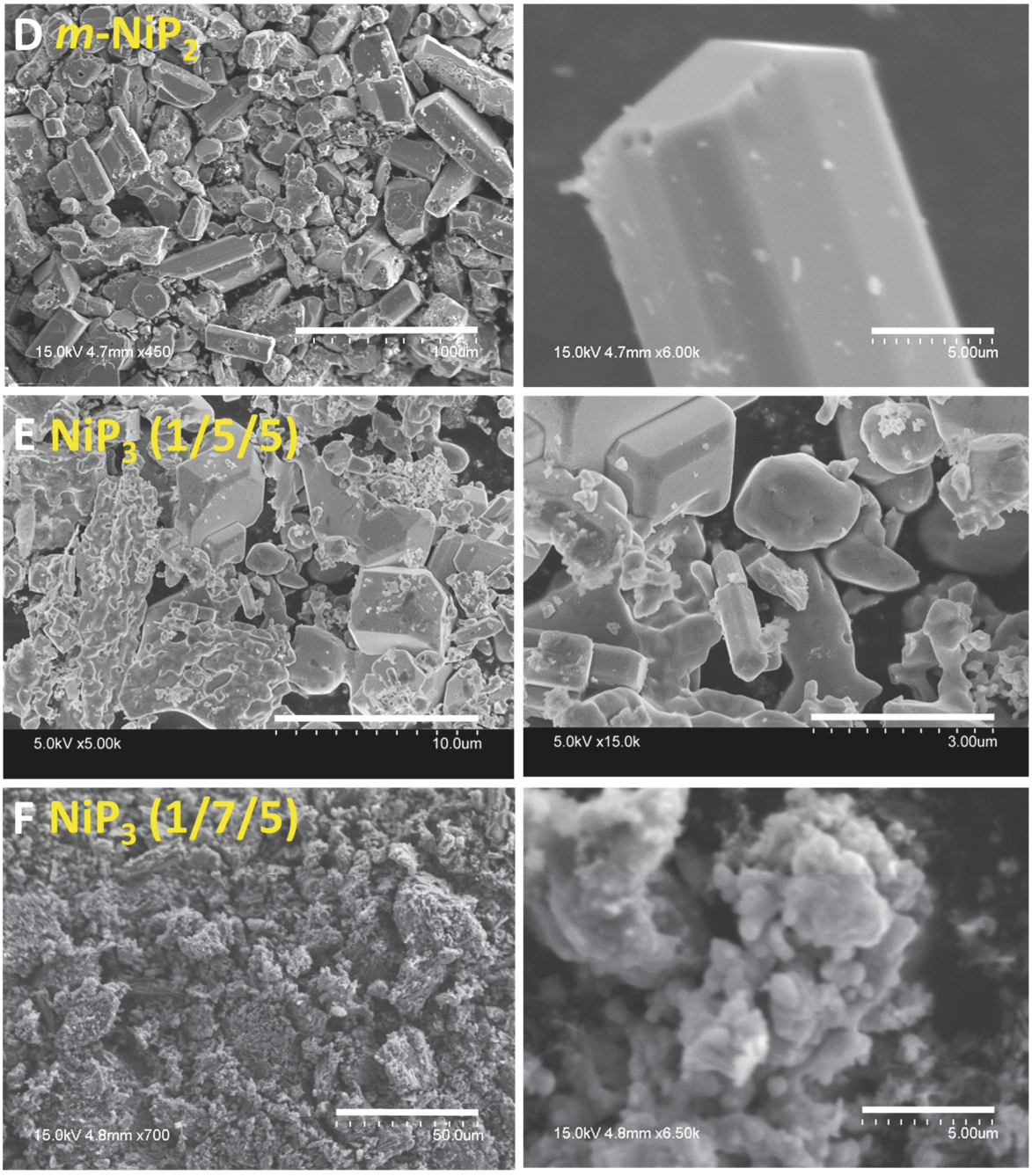

Figure S9. Scanning electron microscopy (SEM) comparison of particle sizes and morphologies obtained from tin flux assisted reactions producing (D) *m*-NiP_2 and (E) NiP_3 (1/5/5) and (F) NiP_3 (1/7/5). The left and right columns show images at low and high magnifications respectively. The lengths of scale bars (left, right) are (D) 100 µm, 5 µm (E) 10 µm, 3 µm (F) 50 µm, 5 µm respectively.

Table S2. Summary data of XPS peak deconvolutions on nickel phosphides from **Figure S9** below with reference data from NIST database[5] or from listed reference. NiO/Ni $(OH)_2$ satellite (s) peaks are noted. For some Ni, P and Cl peak deconvolutions, this table shows 2p peak positions with calculated deconvolution areas greater than 7%. Peaks consistent with $2p_{3/2}$ transitions are denoted as (*).

Nickel phosphide	**Ni_2P**	***c*-NiP_2**	***m*-NiP_2**	**NiP_3 (1/5/5)**	**Literature (eV ± 1.0) (ref. number)**	
Ni 2p (eV)	853.4 (*) 857.0 862.3 (s)	854.2 (*) 854.6 (*) 856.7 (*) 863.0 (s) 872.0 874.8 877.9	854.0 (*) 855.4 (*) 871.3	851.4 (*) 854.3 (*) 871.2	Ni metal Ni_2P *c*-NiP_2 *m*-NiP_2 NiP_3/CNT NiO Ni $(OH)_2$	852.2 853.1 854.4 (6) 853.4 (6) 853.9 (7) 854.0 856.0
P 2p (eV)	129.4 (*) 130.3 (*) 134.6 136.1 137.2	128.7 (*) 129.5 (*) 130.0 (*) 134.0 135.9	129.4 (*) 130.1 (*) 130.9 134.0	127.2 129.9 (*) 134.0	P (white) Ni_2P *c*-NiP_2 *m*-NiP_2 NiP_3/CNT PCl_3 $Ni_3(PO_4)_2$ Na_2HPO_4 P_2O_5	129.9 129.5 128.7 (6) 129.3 (6) 129.8 (7) 131.1 133.3 134.0 135.6
O 1s (eV)	531.6 533.1 535.1	531.6 533.1 534.9	531.6 533.0	529.8 532.3	SnO NiO Ni_3PO_4 Na_2HPO_4 SnO_2 Ni $(OH)_2$ $NaPO_3$ P_2O_5	530.1 530.7 531.2 531.4 531.5 531.5 533.3 534.8
Cl 2p (eV)	198.5 (*) 199.2 200.6	--	--	--	$NiCl_2$ $PCl(OC_2H_5)_2$	198.3 199.6
Sn $3d_{5/2}$(eV)	--	--	485.3 487.6 489.2	485.5 488.0	Sn metal SnO $SnCl_2$ SnO_2	485.0 486.0 486.7 486.9

Ni_2P

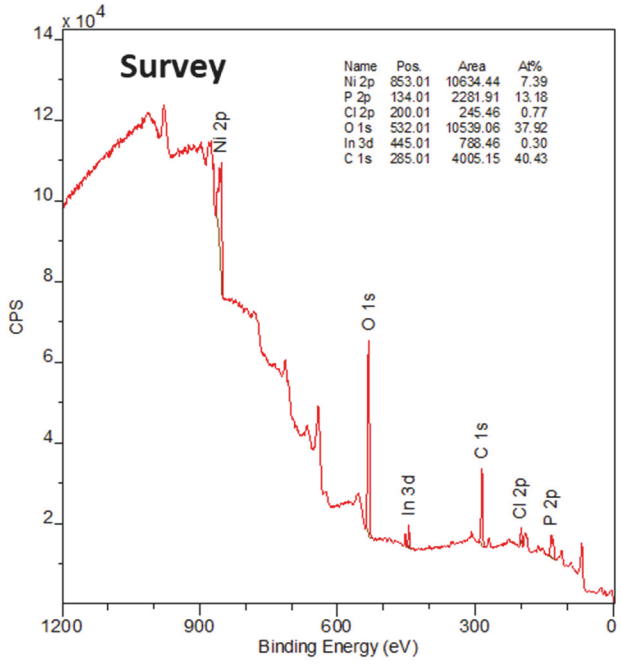
Survey
x 10^4
CPS
Binding Energy (eV)
Ni 2p
O 1s
In 3d
C 1s
Cl 2p
P 2p
Name Pos. Area At%
Ni 2p 853.01 10634.44 7.39
P 2p 134.01 2281.91 13.18
Cl 2p 200.01 245.46 0.77
O 1s 532.01 10539.06 37.92
In 3d 445.01 788.46 0.30
C 1s 285.01 4005.15 40.43

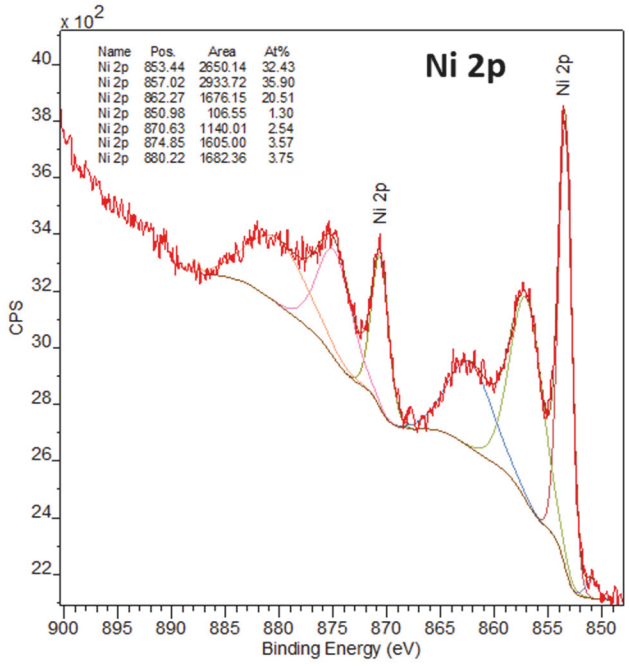
Ni 2p
x 10^2
CPS
Binding Energy (eV)
Ni 2p
Ni 2p
Name Pos. Area At%
Ni 2p 853.44 2650.14 32.43
Ni 2p 857.02 2933.72 35.90
Ni 2p 862.27 1676.15 20.51
Ni 2p 850.98 106.55 1.30
Ni 2p 870.63 1140.01 2.54
Ni 2p 874.85 1605.00 3.57
Ni 2p 880.22 1682.36 3.75

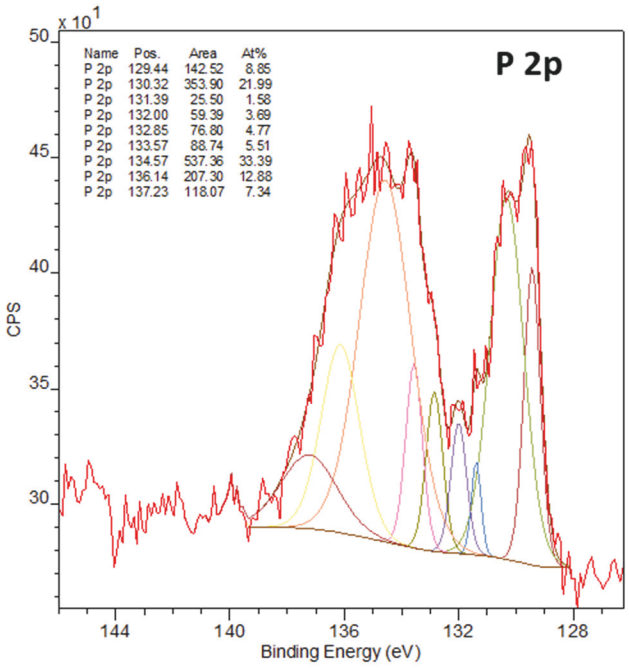
P 2p
x 10^1
CPS
Binding Energy (eV)
Name Pos. Area At%
P 2p 129.44 142.52 8.85
P 2p 130.32 353.90 21.99
P 2p 131.39 25.50 1.58
P 2p 132.00 59.39 3.69
P 2p 132.85 76.80 4.77
P 2p 133.57 88.74 5.51
P 2p 134.57 537.36 33.39
P 2p 136.14 207.30 12.88
P 2p 137.23 118.07 7.34

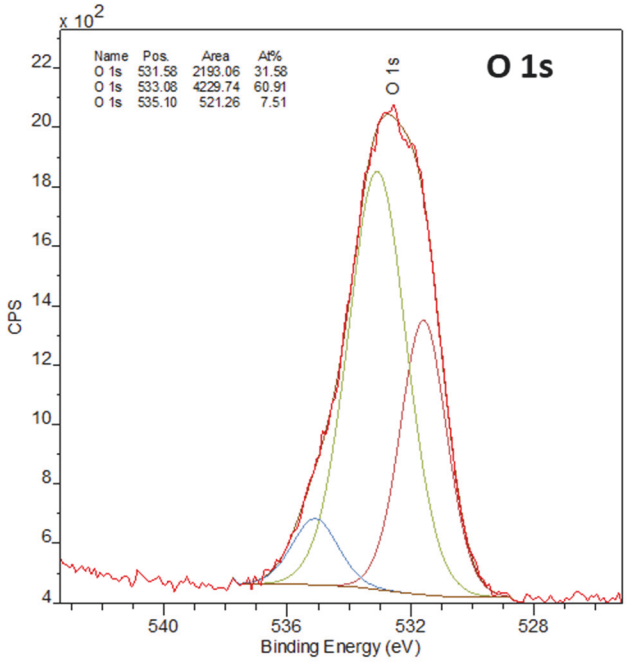
O 1s
x 10^2
CPS
Binding Energy (eV)
O 1s
Name Pos. Area At%
O 1s 531.58 2193.06 31.58
O 1s 533.08 4229.74 60.91
O 1s 535.10 521.26 7.51

c-NiP_2

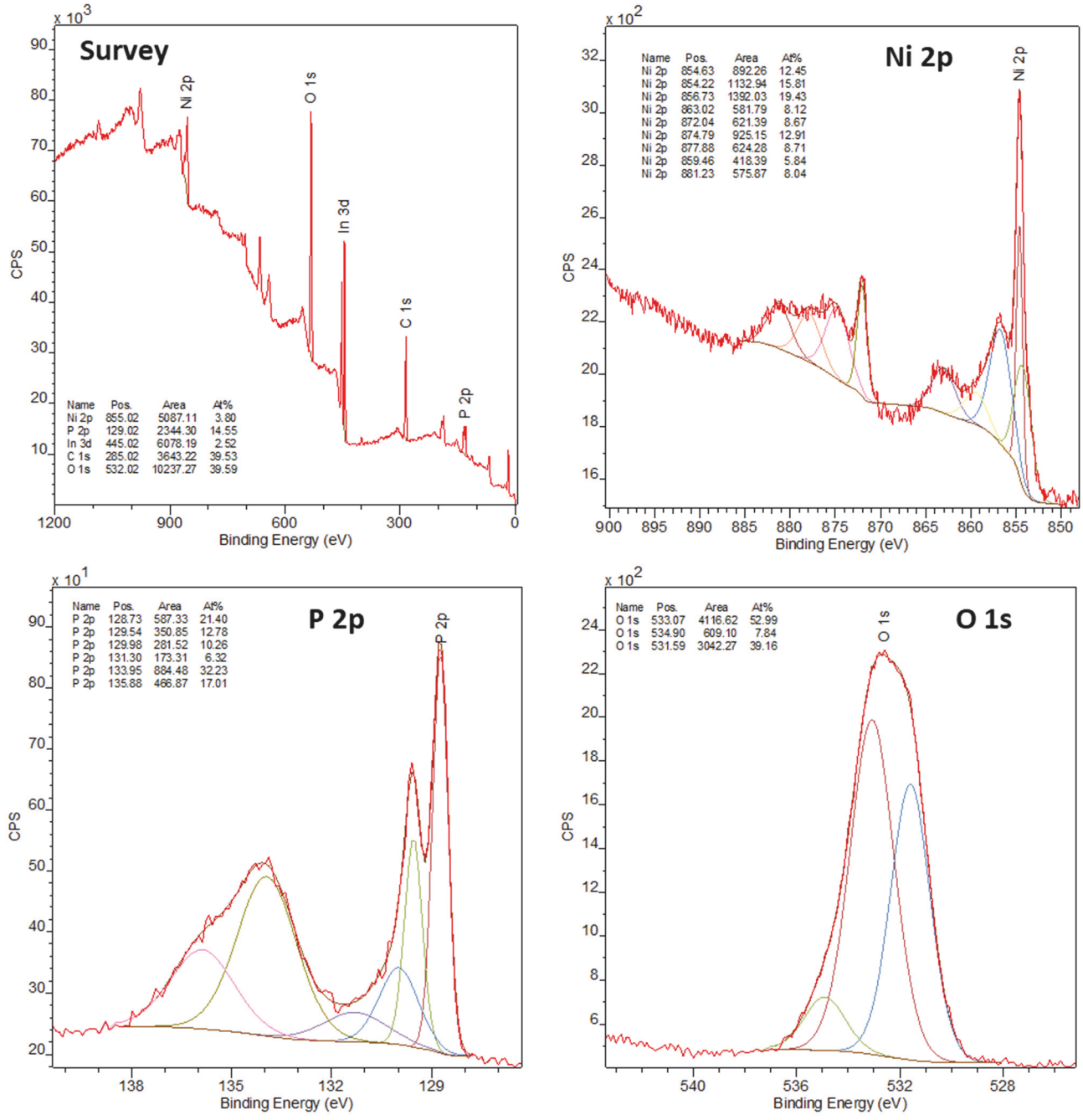
Survey
Ni 2p
O 1s
In 3d
C 1s
P 2p
Name Pos. Area At%
Ni 2p 855.02 5087.11 3.80
P 2p 129.02 2344.30 14.55
In 3d 445.02 6078.19 2.52
C 1s 285.02 3643.22 39.53
O 1s 532.02 10237.27 39.59
Binding Energy (eV)
CPS
Ni 2p
Name Pos. Area At%
Ni 2p 854.63 892.26 12.45
Ni 2p 854.22 1132.94 15.81
Ni 2p 856.73 1392.03 19.43
Ni 2p 863.02 581.79 8.12
Ni 2p 872.04 621.39 8.67
Ni 2p 874.79 925.15 12.91
Ni 2p 877.88 624.28 8.71
Ni 2p 859.46 418.39 5.84
Ni 2p 881.23 575.87 8.04
P 2p
Name Pos. Area At%
P 2p 128.73 587.33 21.40
P 2p 129.54 350.85 12.78
P 2p 129.98 281.52 10.26
P 2p 131.30 173.31 6.32
P 2p 133.95 884.48 32.23
P 2p 135.88 466.87 17.01
O 1s
Name Pos. Area At%
O 1s 533.07 4116.62 52.99
O 1s 534.90 609.10 7.84
O 1s 531.59 3042.27 39.16

m-NiP_2

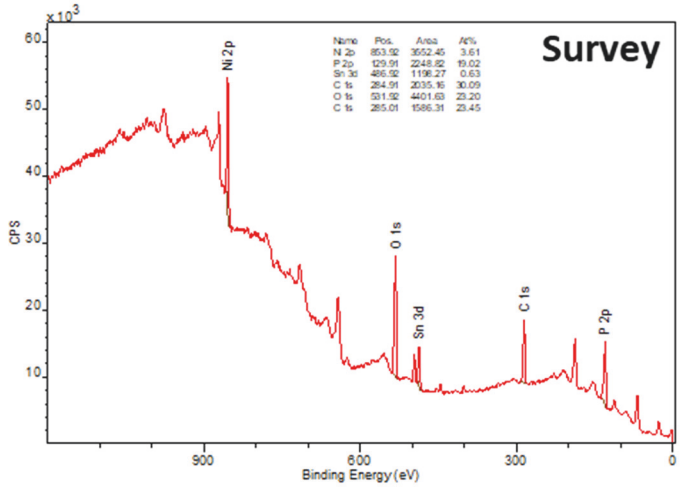
Survey
Ni 2p
O 1s
Sn 3d
C 1s
P 2p
CPS
Binding Energy (eV)

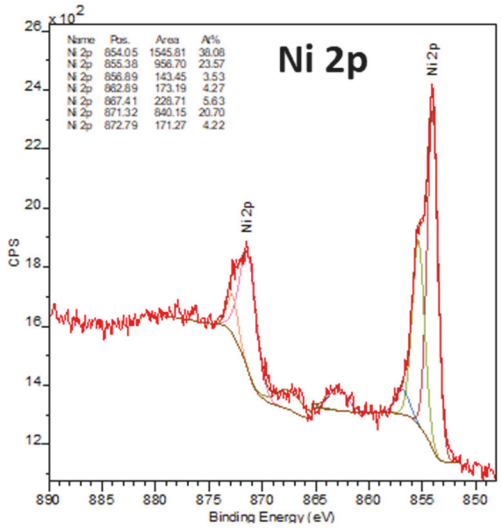
Ni 2p
Ni 2p
Ni 2p
CPS
Binding Energy (eV)

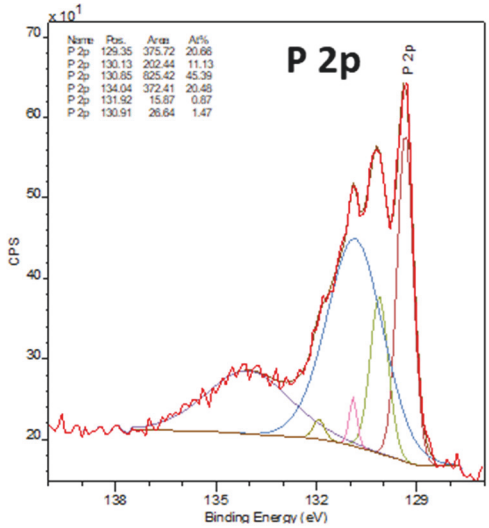
P 2p
P 2p
CPS
Binding Energy (eV)

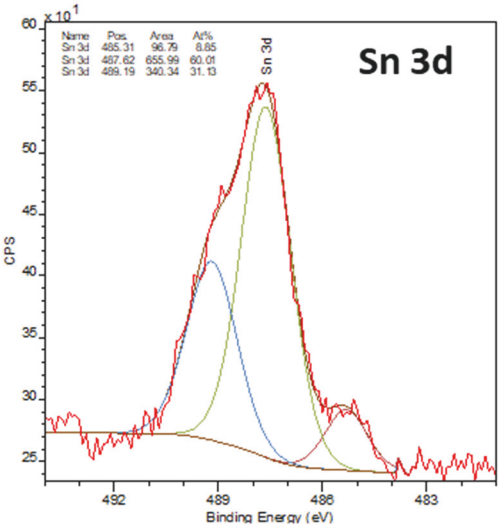
Sn 3d
Sn 3d
CPS
Binding Energy (eV)

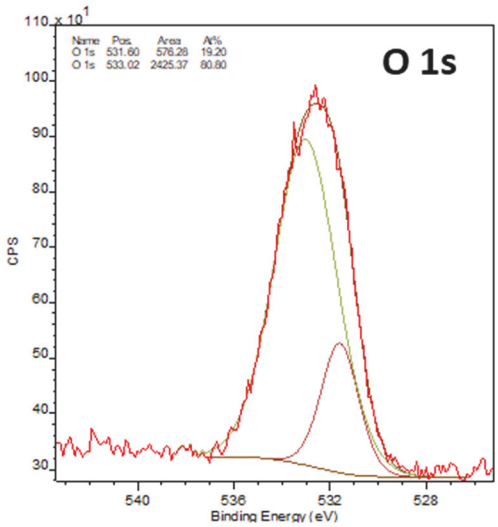
O 1s
CPS
Binding Energy (eV)

NiP_3 (1/5/5)

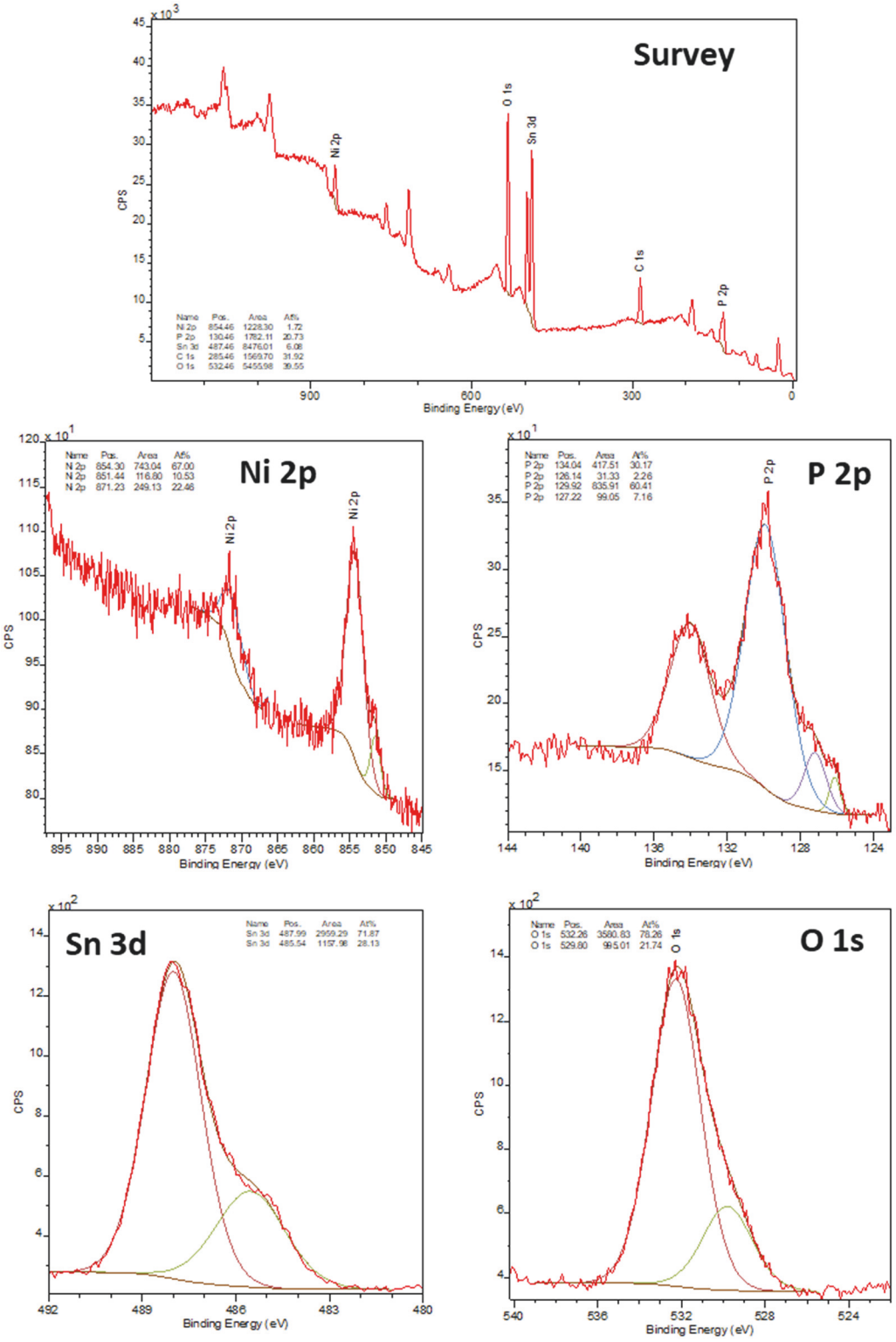

Figure S10. XPS scans of powders on indium foil from $NiCl_2$/P direct reactions (Ni_2P, *c*-NiP_2) and with tin-flux assistance [*m*-NiP_2, NiP_3 (1/5/5)].

Table S3. Summary of targeted reaction, phase, percent yield and XRD results of intermediate and sequential reactions to identify possible reaction pathways in tin-flux assisted *m*-NiP_2/NiP_3 growth. tr = trace peaks detected.

Targeted reaction	**Targeted phase and yield (%)**	**Crude PXRD (major phase in bold)**	**Washed PXRD (major phase in bold)**
c-NiP_2/5Sn	*m*-NiP_2 (--)	**Sn**, *c*-NiP_2	*c*-NiP_2 (6 M HCl, 24 h washed)
c-NiP_2/3P/4Sn	NiP_3 (37)	**Sn_4P_3,** Sn_3P_4, *c*-NiP_2 (tr), NiP_3 (tr)	***c*-NiP_2**, NiP_3 (6 M HCl, 24 h washed)
m-NiP_2/3P/4Sn	NiP_3 (39)	**Sn_4P_3,** Sn_3P_4, *m*-NiP_2, NiP_3 (tr)	***m*-NiP_2**, NiP_3 (6 M HCl, 24 h washed)
4Sn/3P	Sn_4P_3 (95)	Sn_4P_3	-
3Sn/4P	Sn_3P_4 (87)	**Sn_4P_3**, Sn_3P_4	-
Sn_4P_3/$NiCl_2$	NiP_3 (30)	**Sn**, *m*-NiP_2, Ni_2SnP (tr)	***m*-NiP_2**, Ni_2SnP (tr) (12 M HCl, 18 h washed)
$NiCl_2$/2Sn	[Ni-Sn] (98)	**Ni_3Sn_4**, Ni_3Sn, Ni_3Sn_2	-
($NiCl_2$/2Sn)/5P/3Sn	NiP_3 (84)	**NiP_3, Sn_4P_3**, *m*-NiP_2, Sn	**NiP_3**, *m*-NiP_2, Sn_4P_3 (0.1 M HCl, 24 h, 6 M HCl, 1 h washed)
$NiCl_2$/5Sn	[Ni-4Sn] (100)	-	-
($NiCl_2$/5Sn)/5P	NiP_3 (84)	**Sn_4P_3**, NiP_3, m-NiP_2	**NiP_3**, ***m*-NiP_2**, Sn_4P_3 (6 M HCl, 24 h washed)

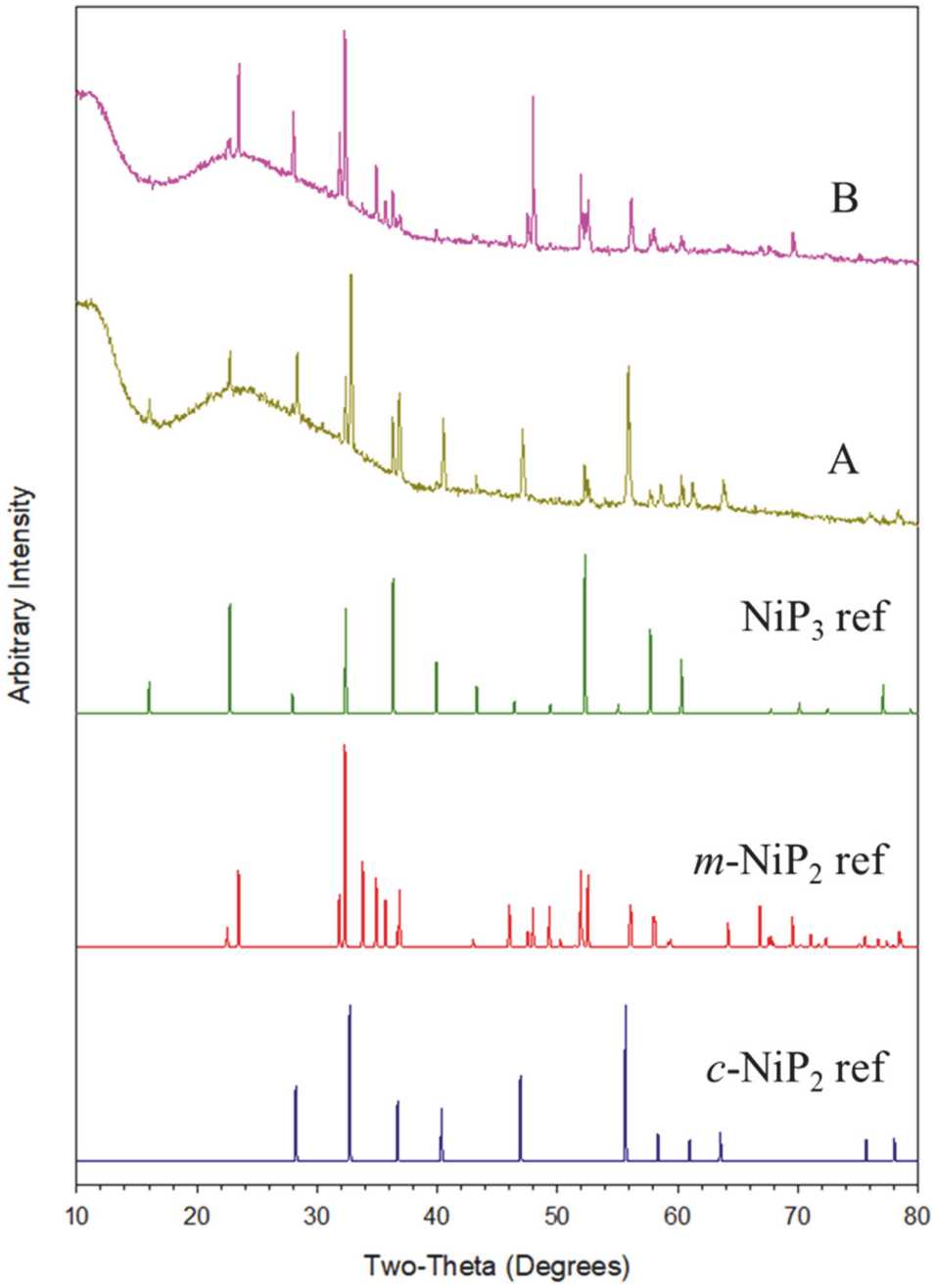

Figure S11. XRD of targeted NiP_3 associated with possible reaction pathways in tin flux assisted nickel phosphide growth: 6 M HCl, 24 h washed products of (A) *c*-NiP_2/3P/4Sn and (B) *m*-NiP_2/3P/4Sn reactions at 500 °C**.**

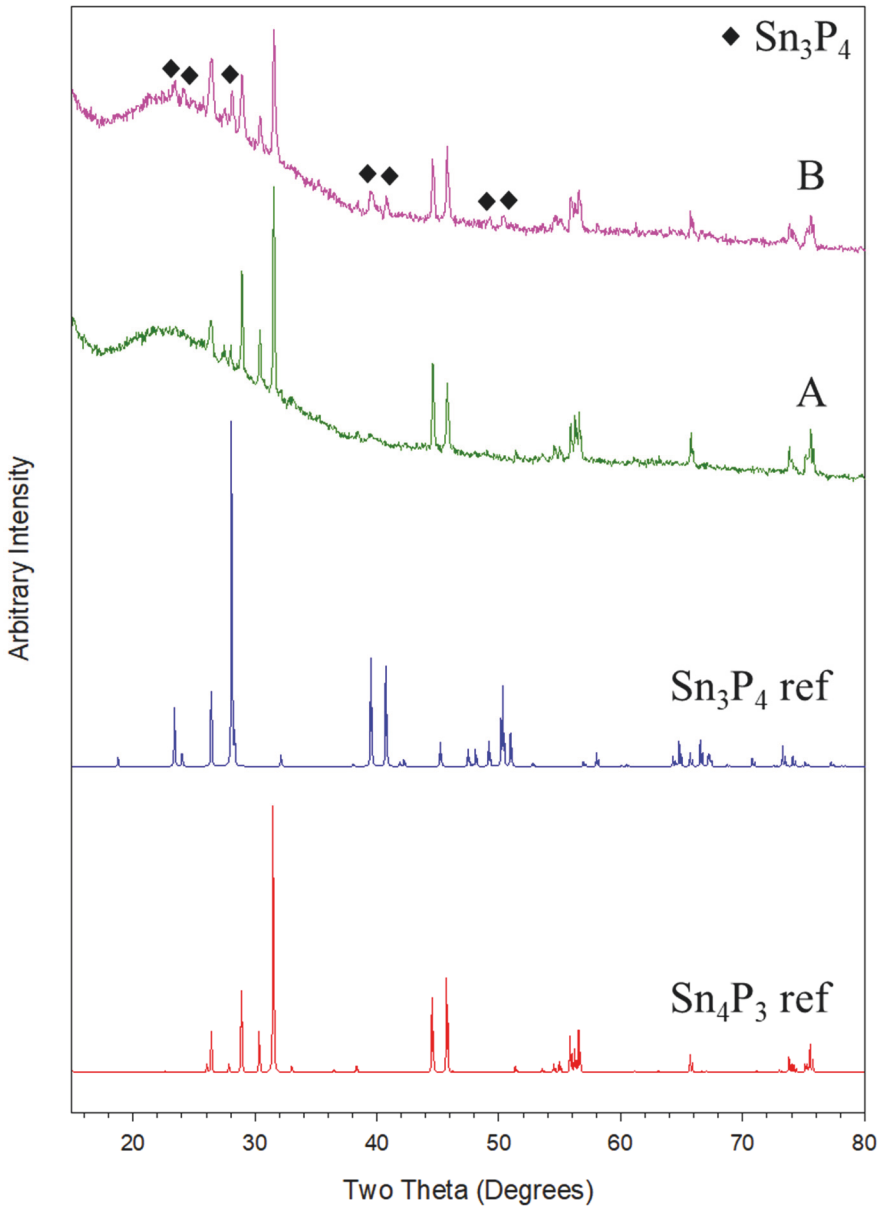

Figure S12. XRD of targeted synthesis of Sn-P phases associated with possible reaction pathways in tin flux assisted nickel phosphide growth: (A) Sn_4P_3 (4Sn/3P at 500 °C) and (B) Sn_3P_4 (3Sn/4P at 500 °C).

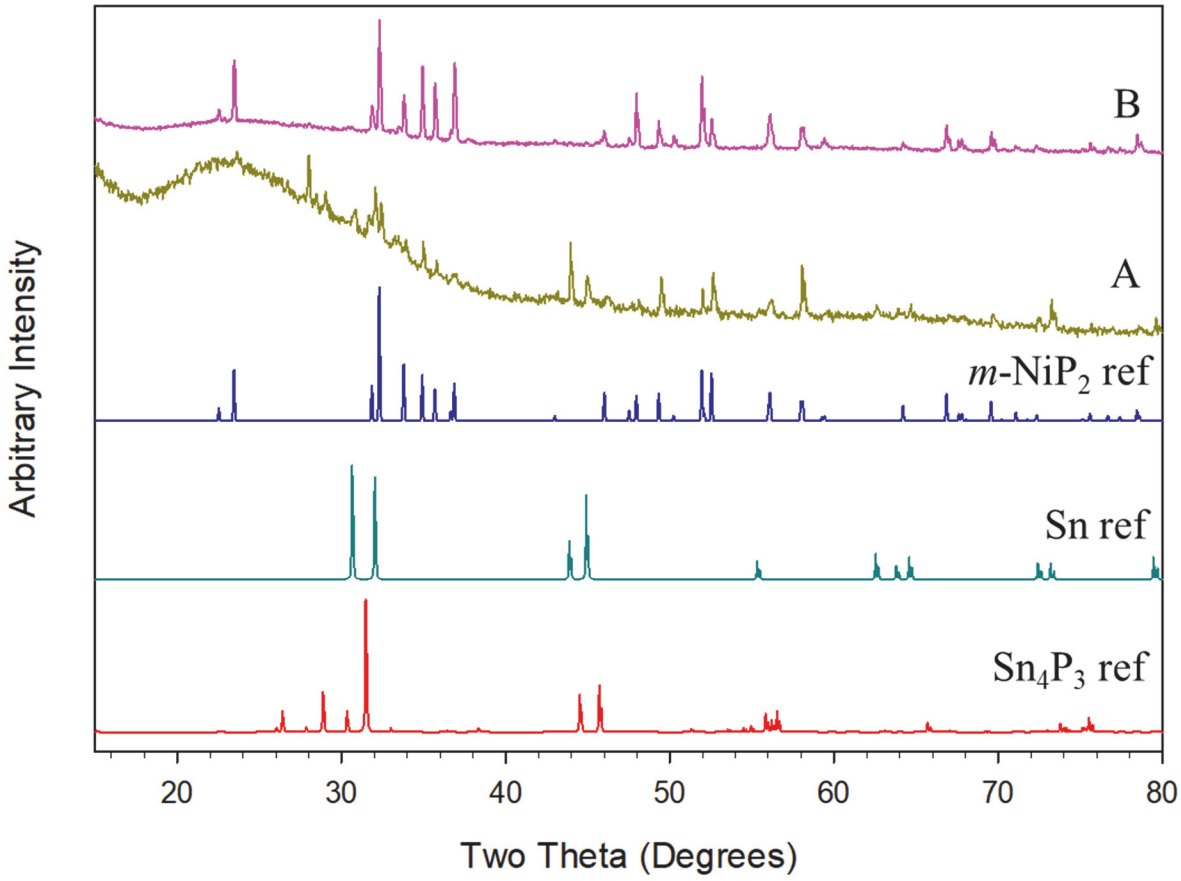

Figure S13. XRD of several intermediate reactions at 500 °C associated with possible reaction pathways in tin flux assisted nickel phosphide growth: (A) unwashed ($NiCl_2/Sn_4P_3$) (B) washed product A.

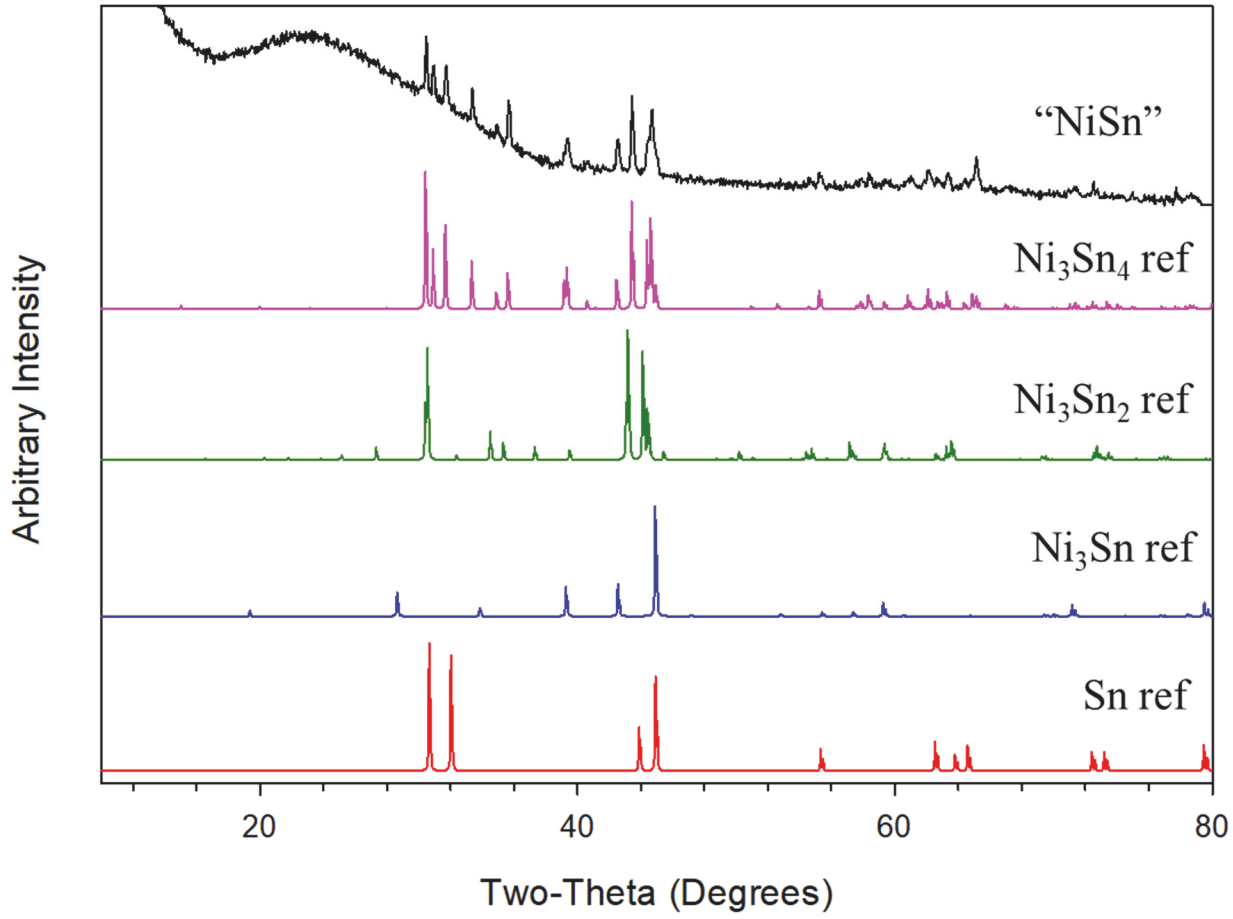

Figure S14. XRD of "NiSn" from $NiCl_2$/2Sn reaction at 500 °C associated with possible reaction pathways in tin flux assisted nickel phosphide growth.

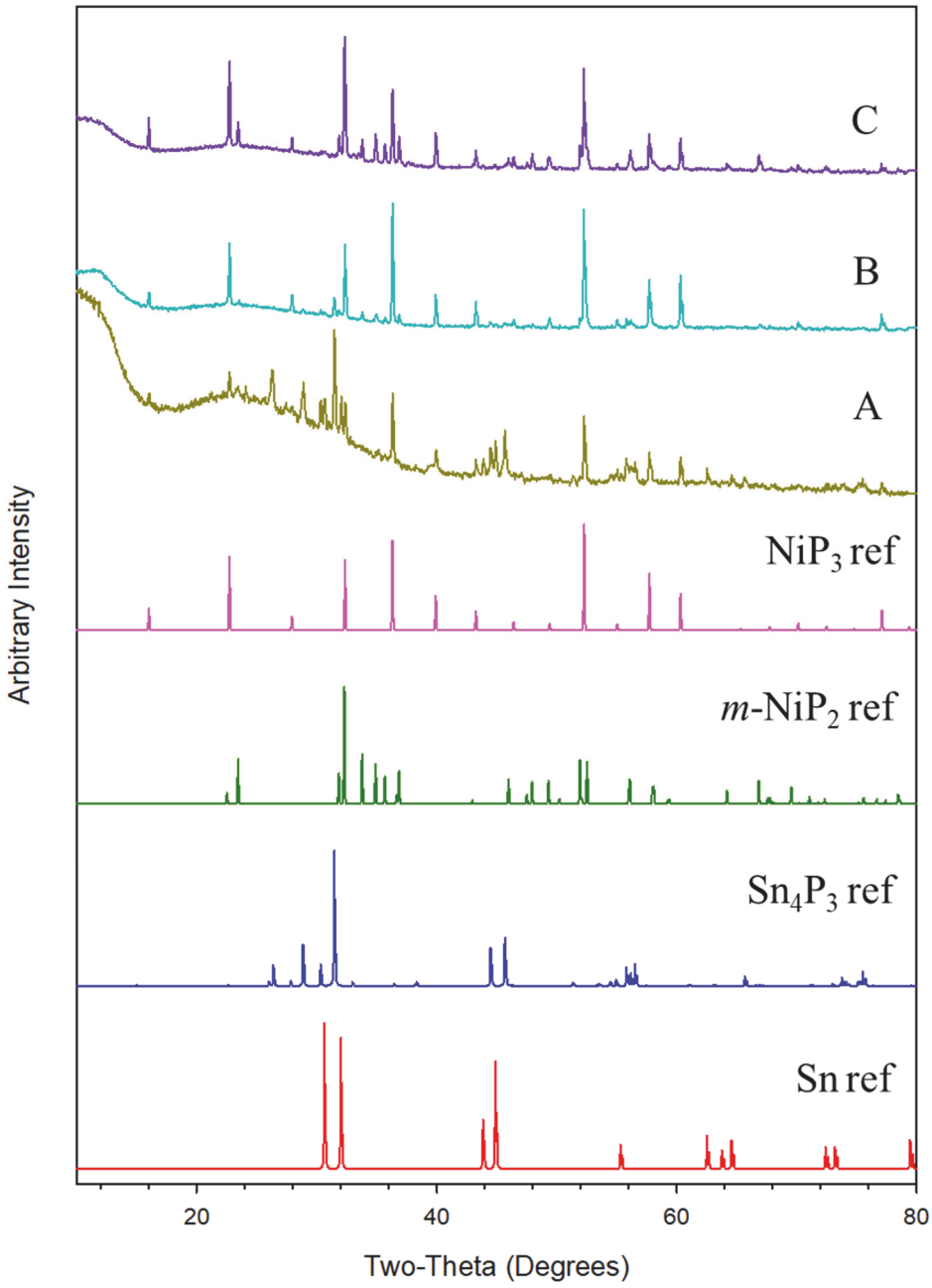

Figure S15. XRD of several intermediate reactions (A) unwashed $NiP_{2/3}$ ("NiSn"/3Sn/5P) (B) washed $NiP_{2/3}$ product from A ("NiSn"/3Sn/5P) (C) washed $NiP_{2/3}$ product from ("$NiSn_4$"/5P) associated with possible reaction pathways in tin flux assisted nickel phosphide growth.

Table S4. Literature comparison table for nickel phosphides HER activity in 0.5 M H_2SO_4. All current densities are normalized for the geometrical surface area of the electrode. a) values estimated from plots and graphical data in reference.

Nickel phosphide	Electrode, Geometric area (cm^2)	10 mA/cm^2 (mV)	20 mA/cm^2 (mV)	Tafel slope (mV/dec)	Ref.
Ni_2P nanoparticles	GCE (0.07)	-170	-215	62	8
Ni_2P film	Ti foil (0.18)	-208	-240	n/a	9
Ni_2P nanoparticles	Ti foil (0.20)	-116	-130	46	10
Ni_2P nanoparticles	GCE (0.07)	-125	-140	87	11
Ni_2P nanoparticles	GCE (0.126)	-137	-181	49	12
Ni_2P film	Ti foil (0.5)	-240[a]	n/a	84	13
Ni_2P nanocrystals	GCE (0.07)	-240	-280[a]	76	14
Ni_2P nanoparticles	GCE (0.126)	-190[a]	-228	83	15
Ni_2P/CNT nanohybrid	GCE (0.126)	-124	-170[a]	53	16
Ni_2P/CNFs	GCE (n/a)	-108	-190[a]	97	17
Ni_2P nanosheets	CC (6)	-152	-181	n/a	18
Ni_5P_4 nanoparticles	GCE (0.126)	-118	-157	42	12
Ni_5P_4 on Ni foil	RDE steel electrode (0.43)	-140	n/a	40	19
c-NiP_2 nanosheets	CC (6)	-75	-99	51	18
c-NiP_2 MP	CC (6)	-180[a]	-253	n/a	18
c-NiP_2	GCE (n/a)	-267	-320[a]	162	6
c-NiP_2/CNFs	GCE (n/a)	-71	-120[a]	74	17
m-NiP_2	Crystal [100] (0.02)	-231	-257	109	20
m-NiP_2	GCE (n/a)	-313	n/a	212	6

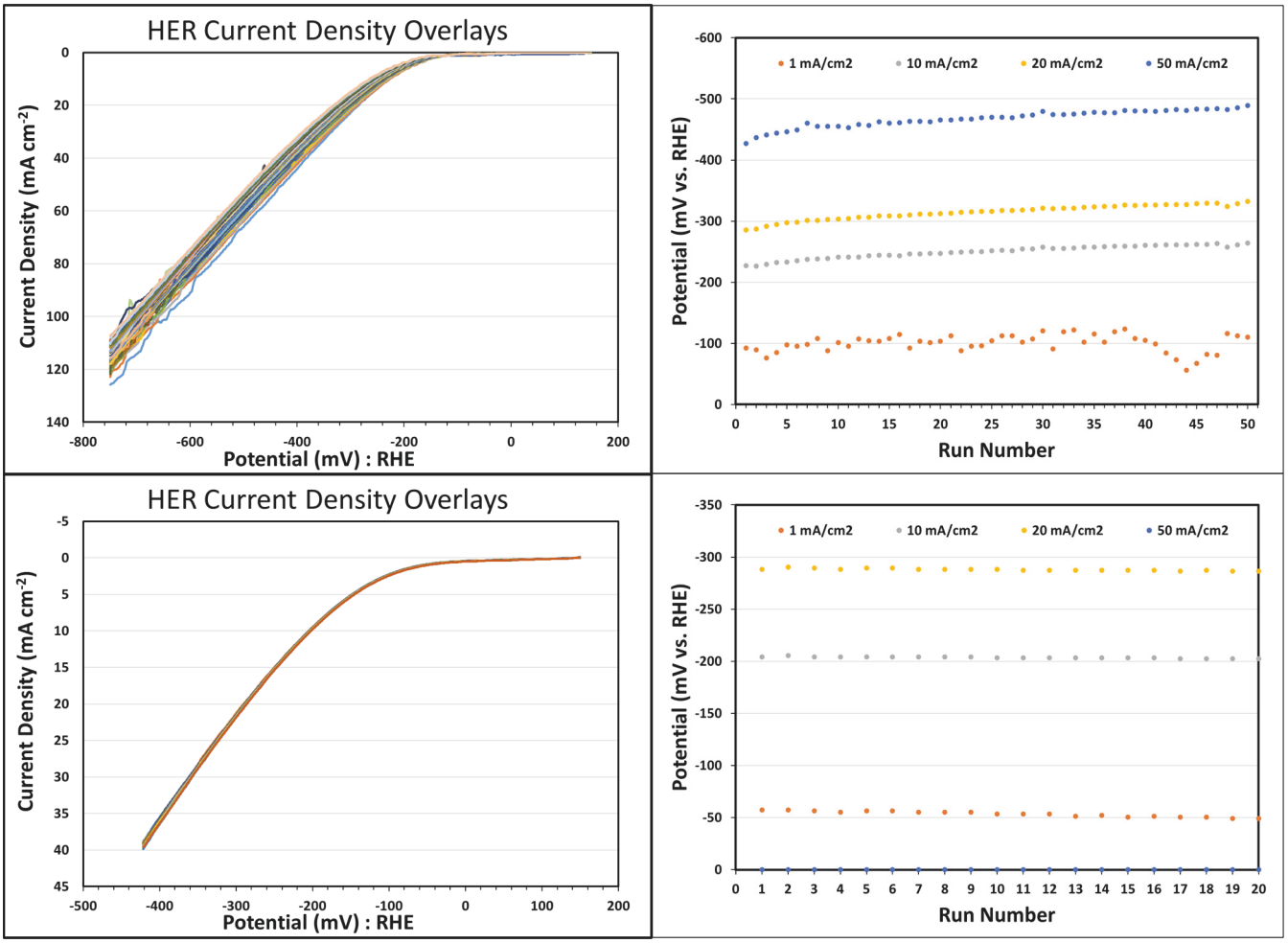

Figure S16. Left column: Overlay plots of iR uncompensated (50 LSV runs, top) and 85% iR compensated (20 LSV runs, bottom) of Ni_2P for HER experiments in 0.5 M H_2SO_4 at 5 mV/s scan rate. Right column: Plots of run number versus applied potentials to produce 1, 10, 20, 50 mA/cm^2 current densities using the LSV overlap plots shown in the left column.

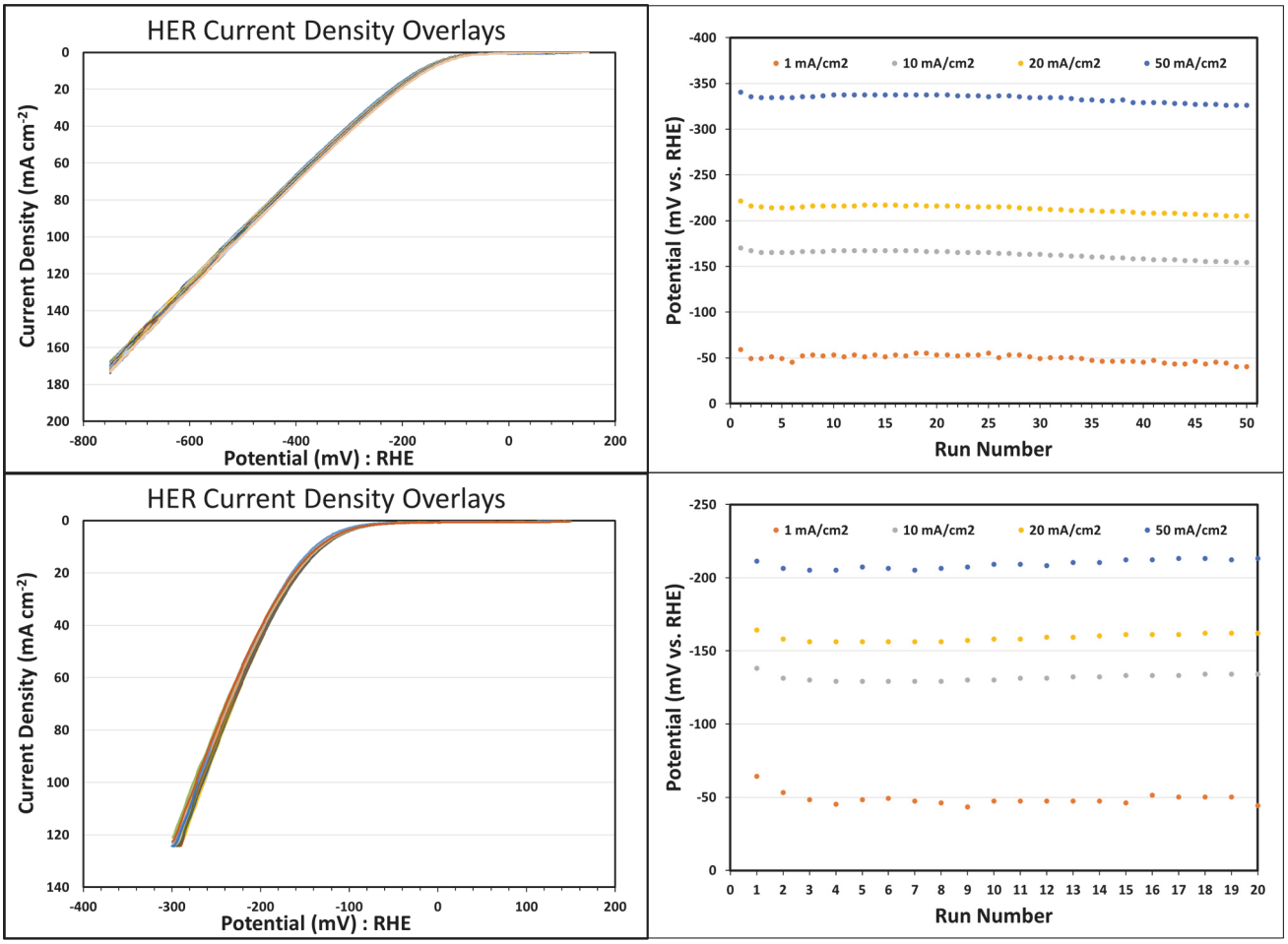

Figure S17. Left column: Overlay plots of iR uncompensated (50 LSV runs, top) and 85% iR compensated (20 LSV runs, bottom) of Ni_5P_4 for HER experiments in 0.5 M H_2SO_4 at 5 mV/s scan rate. Right column: Plots of run number versus applied potentials to produce 1, 10, 20, 50 mA/cm^2 current densities using the LSV overlap plots shown in the left column.

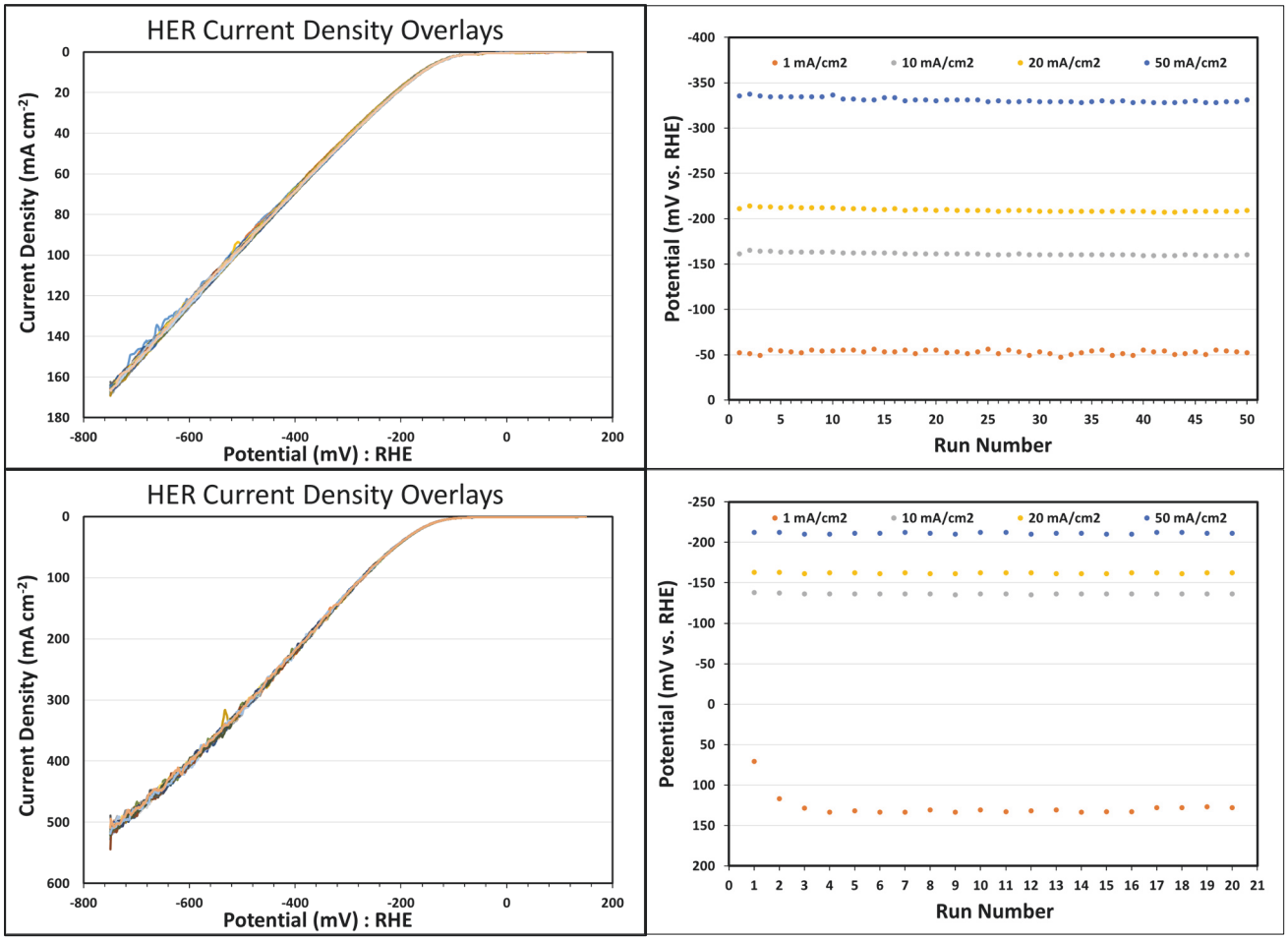

Figure S18. Left column: Overlay plots of iR uncompensated (50 LSV runs, top) and 85% iR compensated (20 LSV runs, bottom) of *c*-NiP_2 for HER experiments in 0.5 M H_2SO_4 at 5 mV/s scan rate. Right column: Plots of run number versus applied potentials to produce 1, 10, 20, 50 mA/cm^2 current densities using the LSV overlap plots shown in the left column.

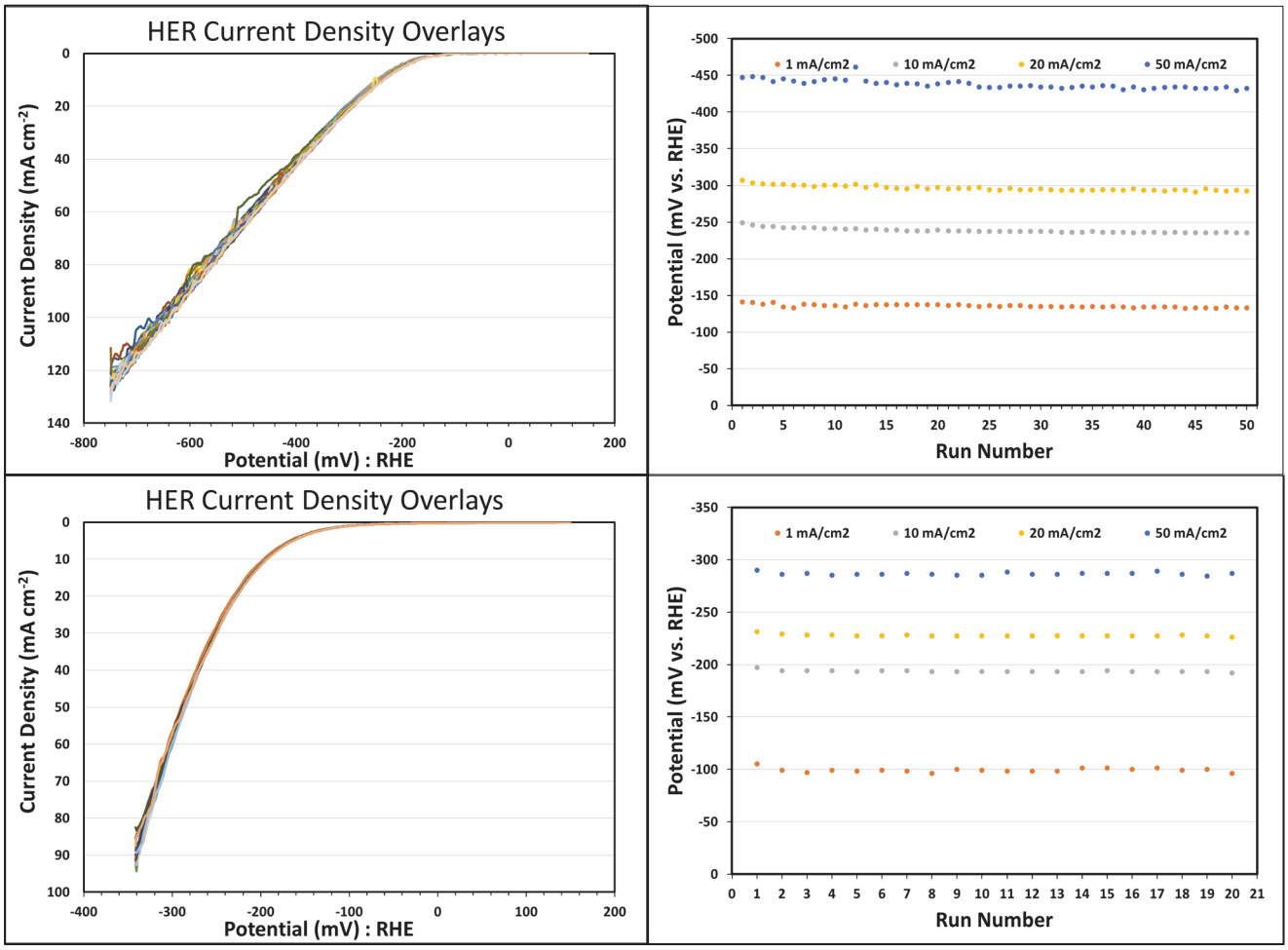

Figure S19. Left column: Overlay plots of iR uncompensated (50 LSV runs, top) and 85% iR compensated (20 LSV runs, bottom) of *m*-NiP_2 for HER experiments in 0.5 M H_2SO_4 at 5 mV/s scan rate. Right column: Plots of run number versus applied potentials to produce 1, 10, 20, 50 mA/cm^2 current densities using the LSV overlap plots shown in the left column.

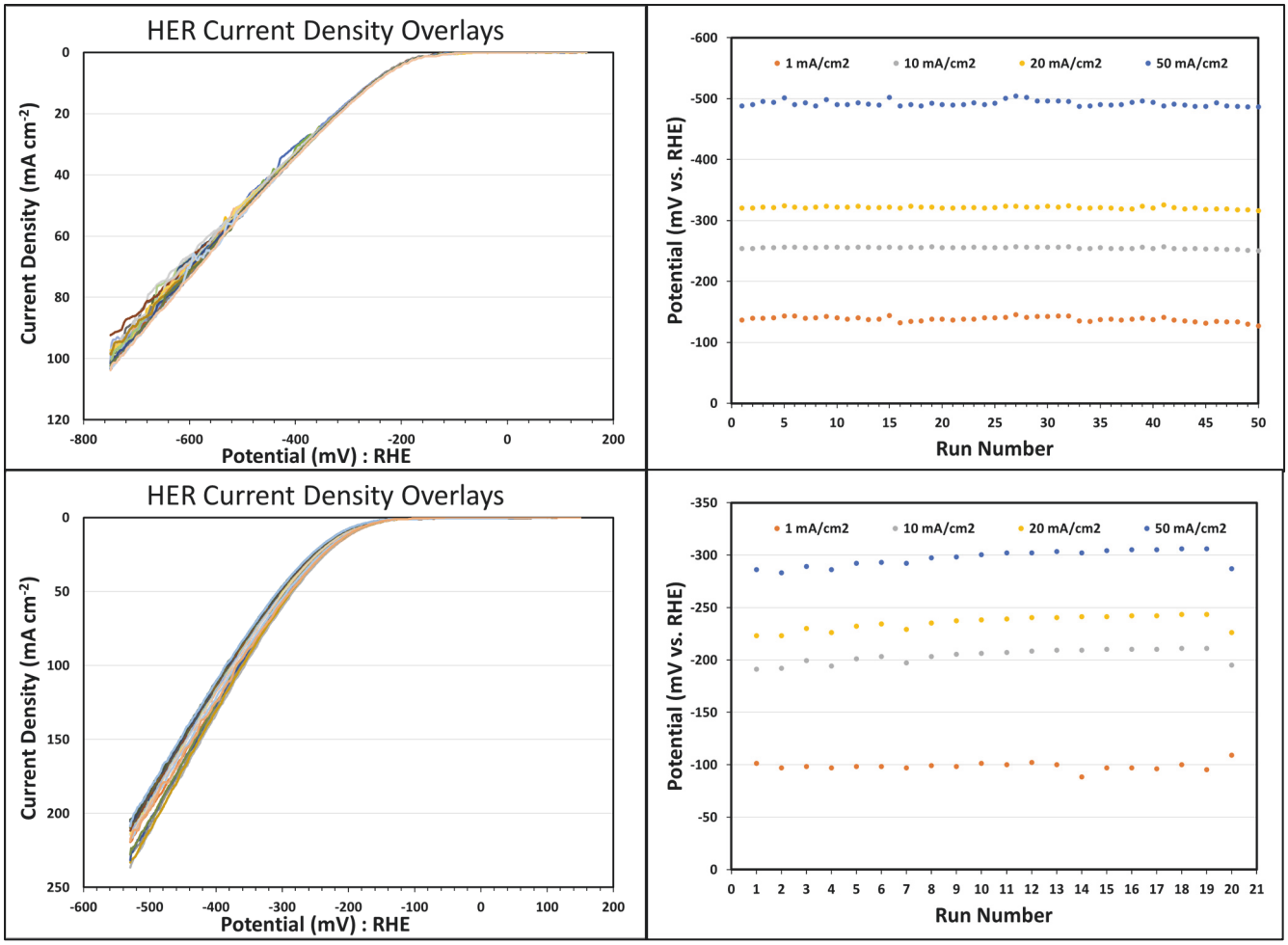

Figure S20. Left column: Overlay plots of iR uncompensated (50 LSV runs, top) and 85% iR compensated (20 LSV runs, bottom) of NiP_3 (1/5/5) for HER experiments in 0.5 M H_2SO_4 at 5 mV/s scan rate. Right column: Plots of run number versus applied potentials to produce 1, 10, 20, 50 mA/cm^2 current densities using the LSV overlap plots shown in the left column.

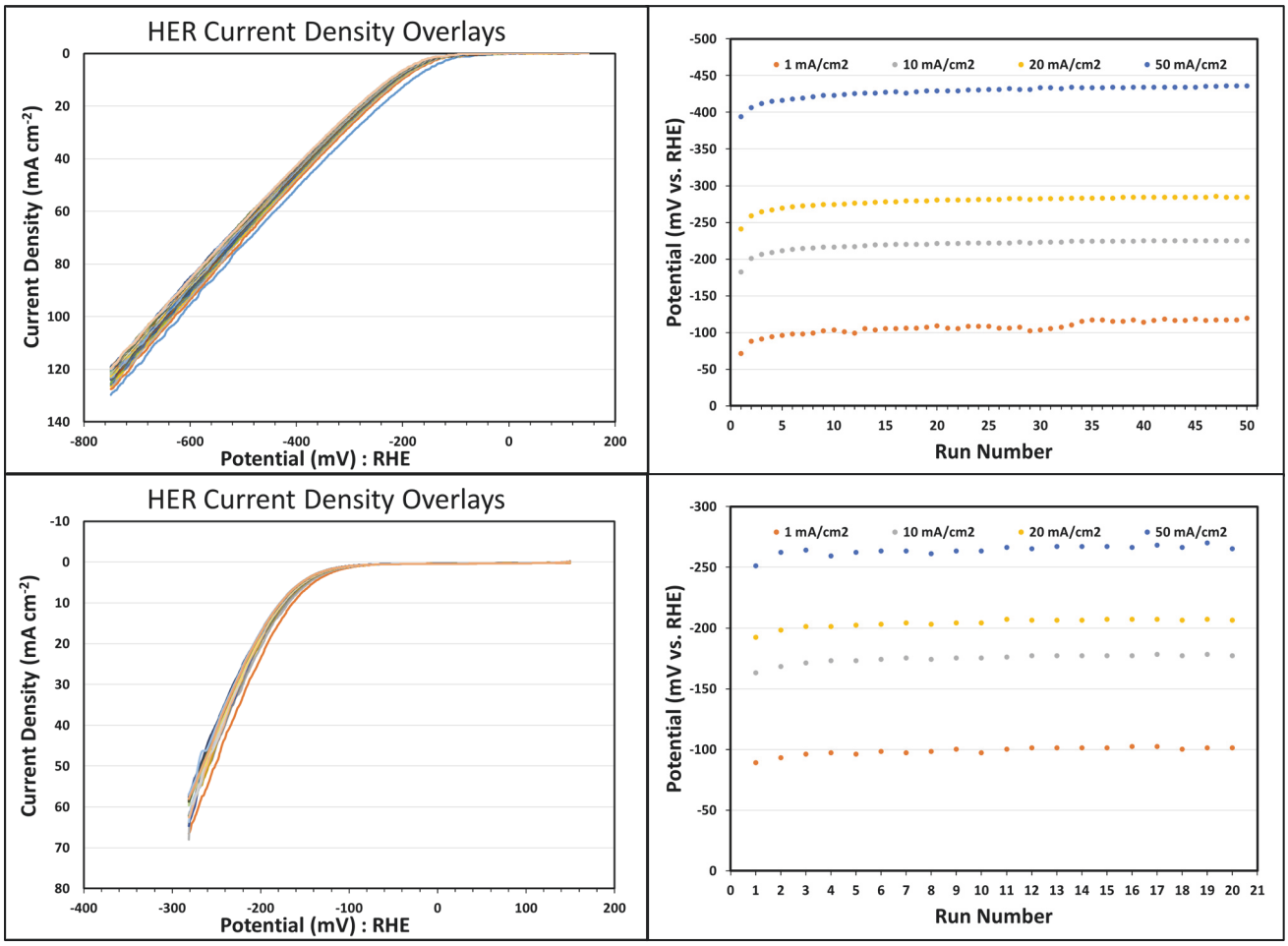

Figure S21. Left column: Overlay plots of iR uncompensated (50 LSV runs, top) and 85% iR compensated (20 LSV runs, bottom) of NiP_3 (1/7/5) for HER experiments in 0.5 M H_2SO_4 at 5 mV/s scan rate. Right column: Plots of run number versus applied potentials to produce 1, 10, 20, 50 mA/cm^2 current densities using the LSV overlap plots shown in the left column.

Table S5. Summary of HER electrocatalysis in 0.5 M H_2SO_4 for tin-flux assisted NiP_3 products obtained using different $NiCl_2$/P/Sn molar ratios. The average applied potentials for 50 (iR uncompensated) or 20 LSV runs (85% iR compensated) are shown. The 85% iR compensated data are in parenthesis.

Nickel phosphide	**PXRD (major phase in bold)**	**10 mA/cm^2** (mV)[1]	**20 mA/cm^2** (mV)[1]	**Tafel slope** (mV/dec)	**Avg ECSA** (cm^2, Before/After 50 LSVs)	**Extended stability**[2]
NiP_3 (1/3/5)	**NiP_3**, *m*-NiP_2, *c*-NiP_2 (~5: 3: 2)	-224 ± 4 (-168 ± 2)	-293 ± 4 (-199 ± 1)	-76 ± 2 (-62 ± 1)	4/5	95%
NiP_3(1/4/2)	NiP_3	-218 ± 6 (-184 ± 5)	-286 ± 6 (-211± 5)	-87 ± 4 (-79 ± 4)	10/5	73%

1) All applied potentials are reported versus RHE, and all current densities are normalized to geometric surface area of 0.08 cm^2. 2) The percent change of current density from 30 min to 18-hour mark for constant potential experiment targeting ~10-15 mA/cm^2

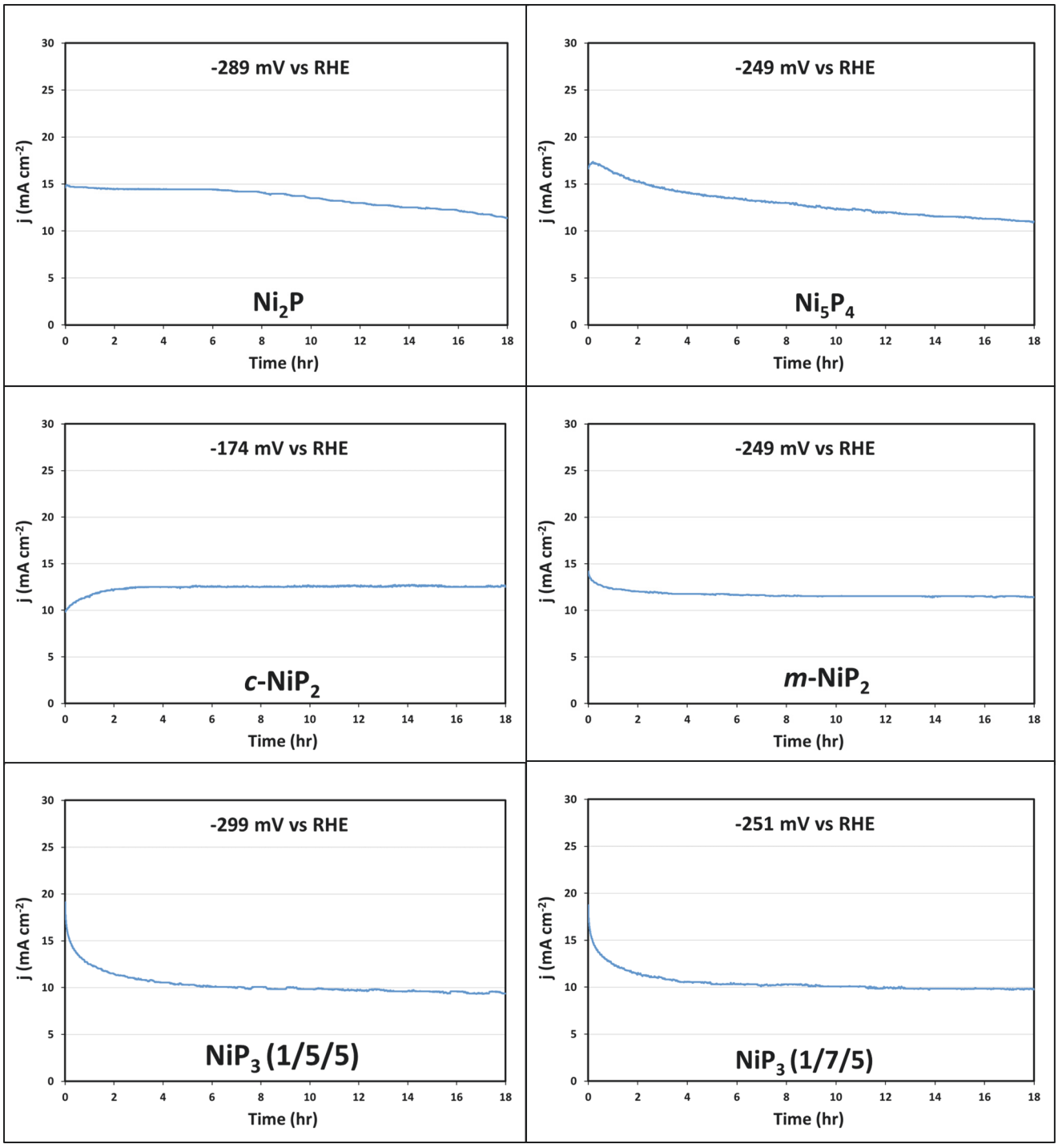

Figure S22. Applied negative potential 18-hour constant potential chronoamperometry (CA) data for nickel phosphides HER in 0.5 M H_2SO_4 using a platinum wire counter electrode. The potentials used are indicated and were selected to ideally sustain a current density of ~10-15 mA/cm^2.

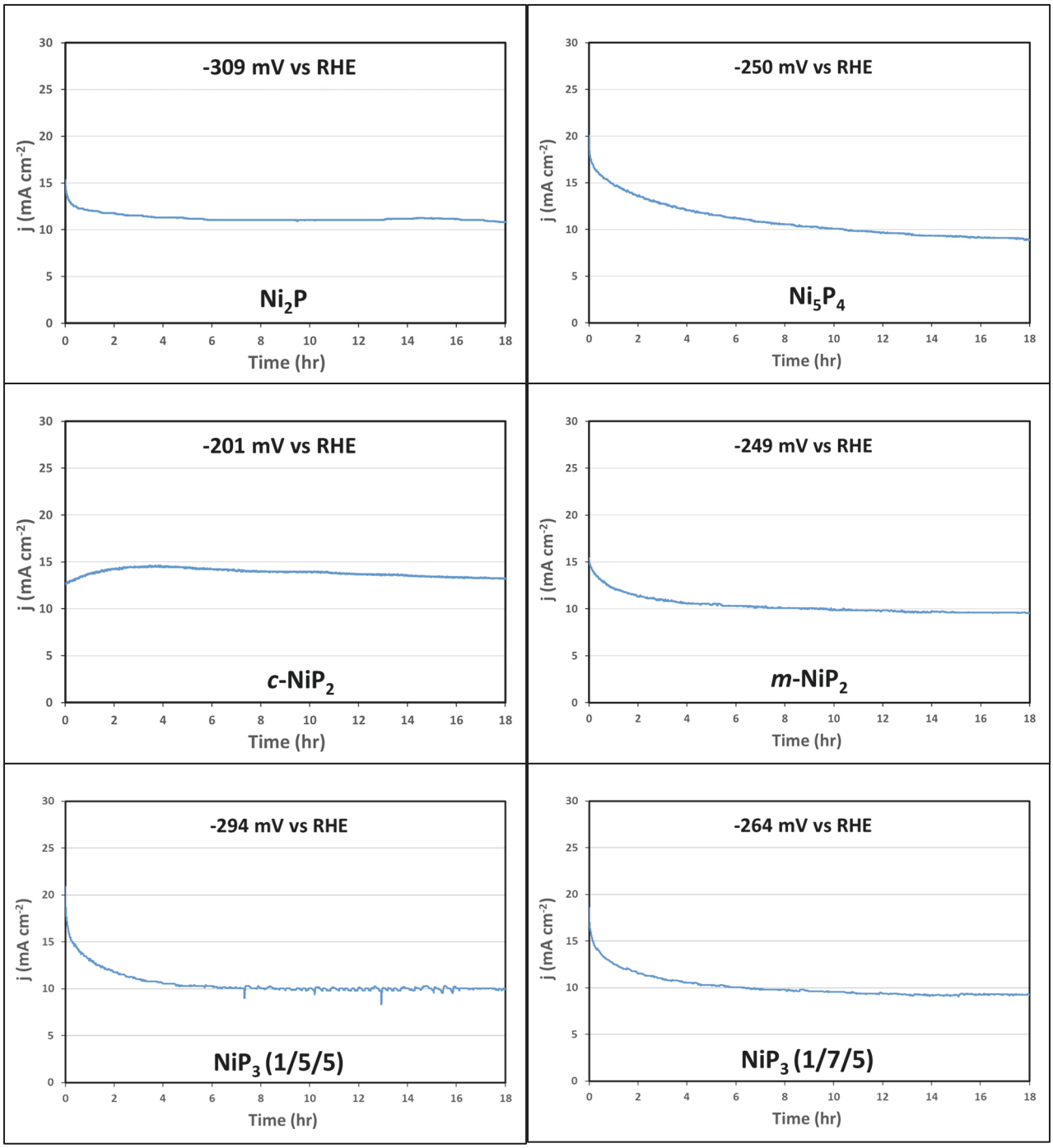

Figure S23. Applied negative potential 18-hour constant potential chronoamperometry (CA) data for nickel phosphides HER in 0.5 M H_2SO_4 using a graphite rod counter electrode. The potentials used are indicated and were selected to ideally sustain a current density of ~10-15 mA/cm^2.

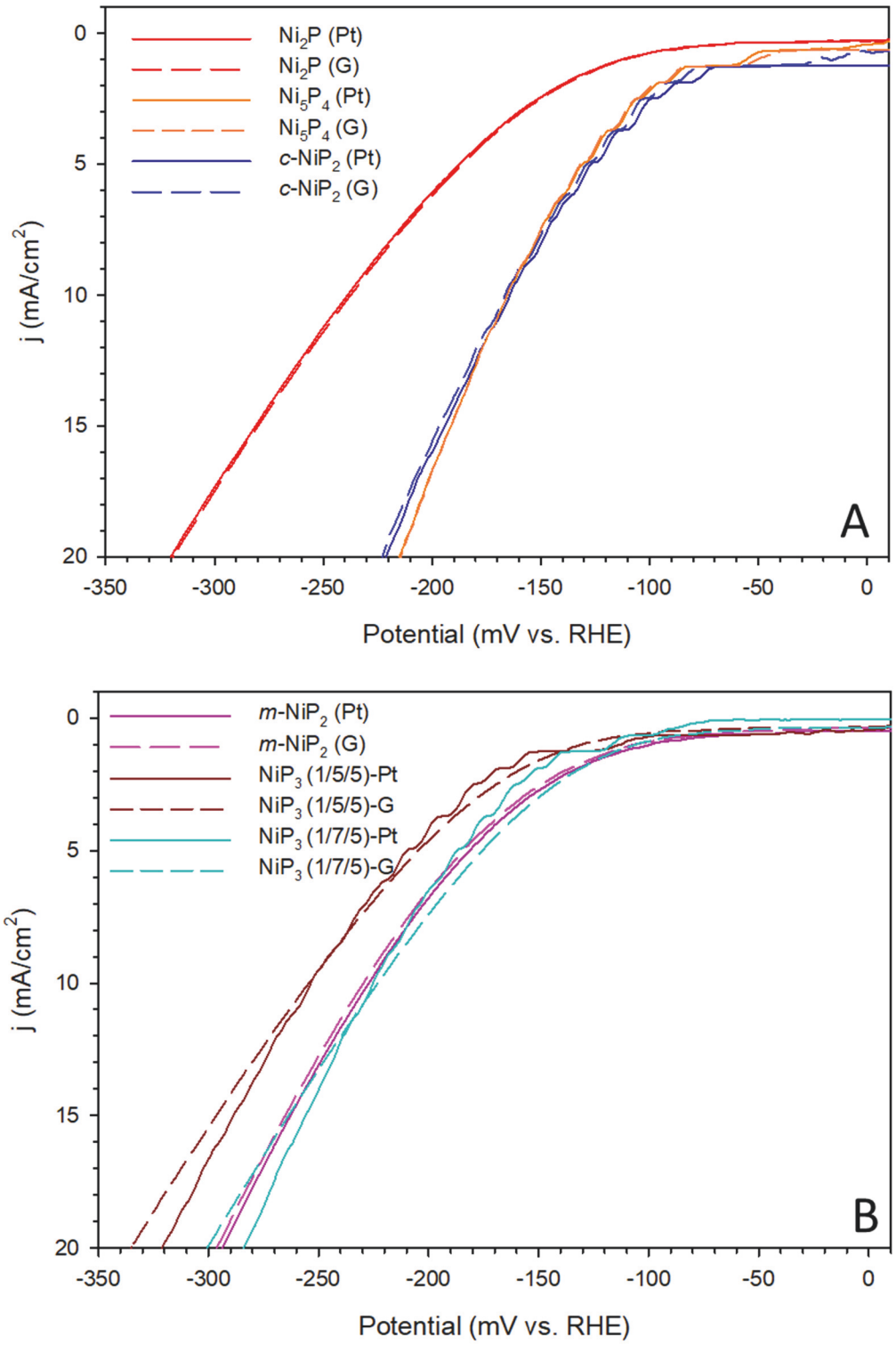

Figure S24. Representative LSV (iR uncompensated) overlay plots of HER results for (A) direct and (B) tin-flux assisted nickel phosphides in 0.5 M H_2SO_4 at 5 mV/s scan rate using platinum wire and graphite rod counter electrodes.

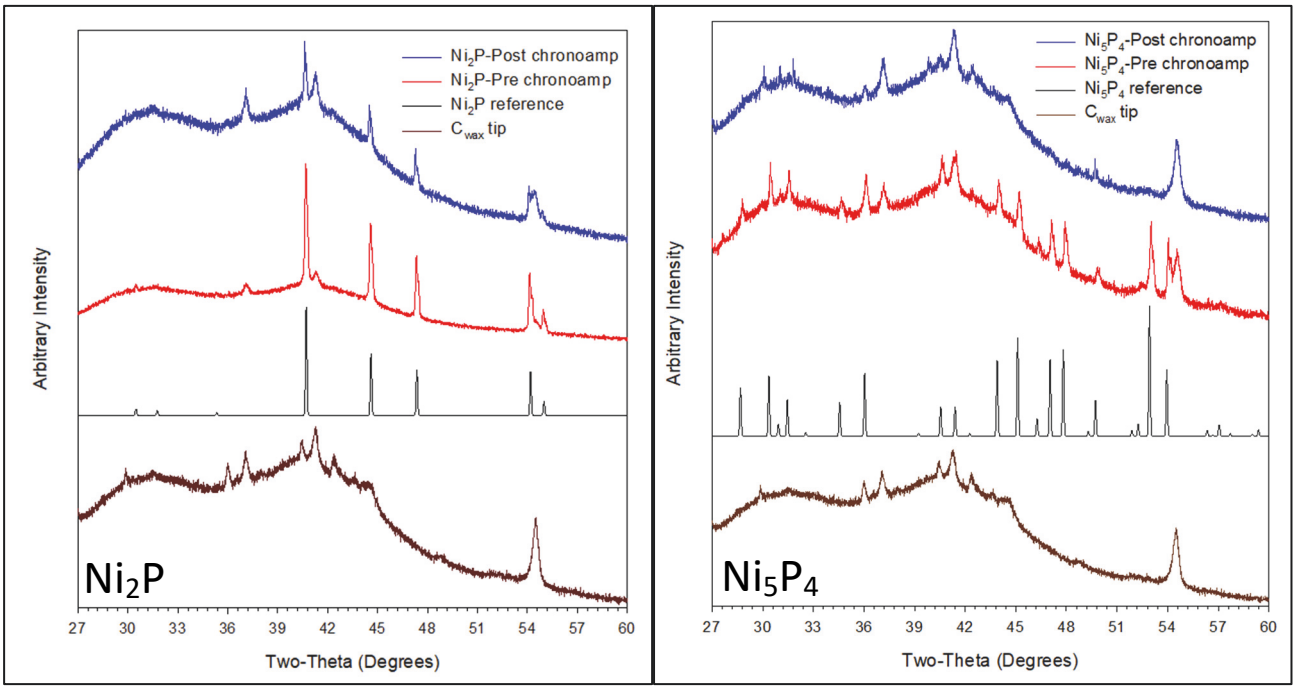

Figure S25. XRD results of metal-rich nickel phosphide materials embedded on C_{wax} tips before and after 18-hour constant potential chronoamperometry (CA) HER experiments. The reference patterns for each nickel phosphide catalyst and diffractogram for blank C_{wax} electrode tips are also shown.

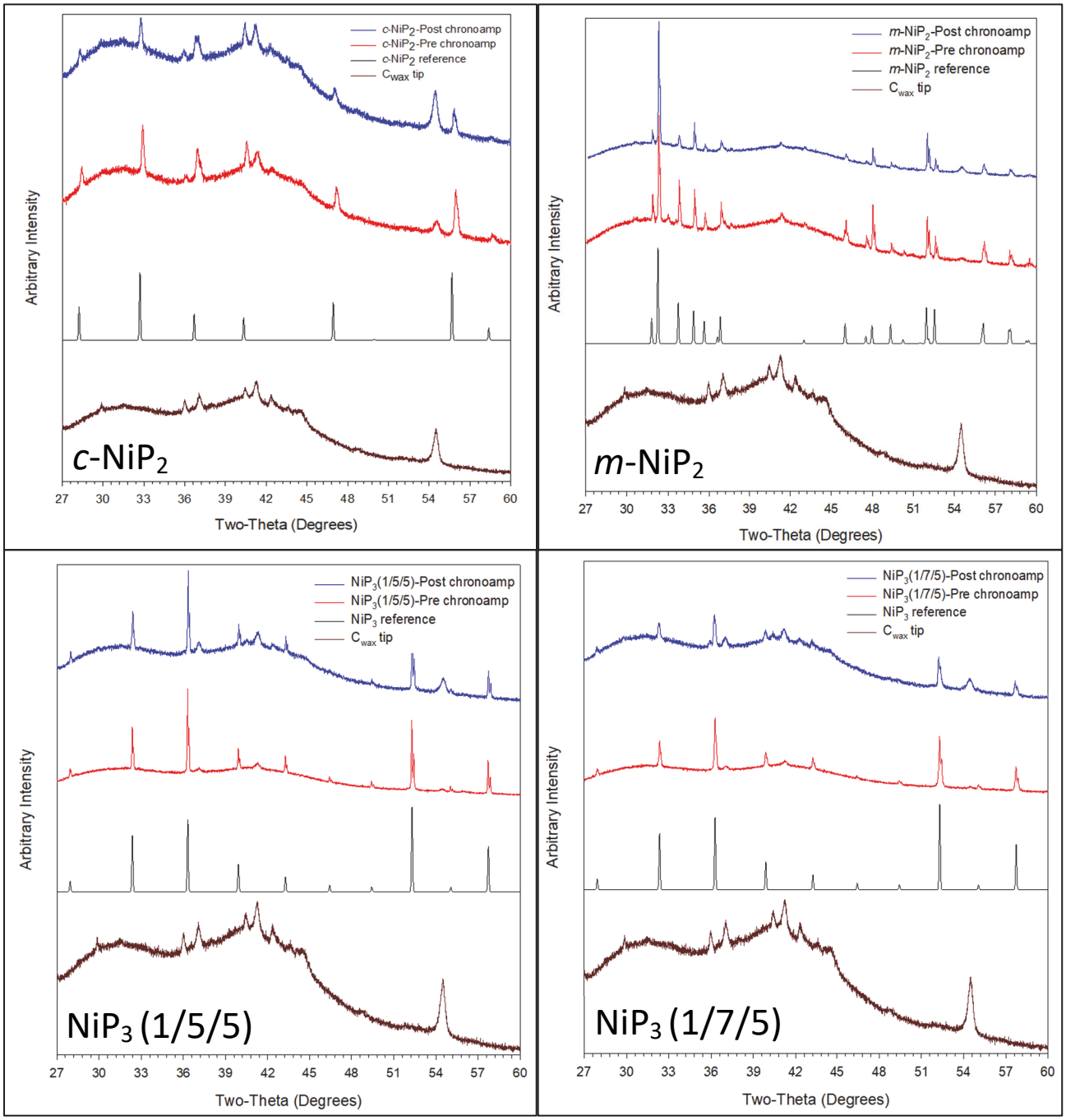

Figure S26. XRD results of phosphorus rich nickel phosphide materials embedded on C wax tips before and after 18-hour constant potential chronoamperometry (CA) HER experiments. The reference patterns for each nickel phosphide catalyst and diffractogram for blank C_{wax} electrode tips are also shown.

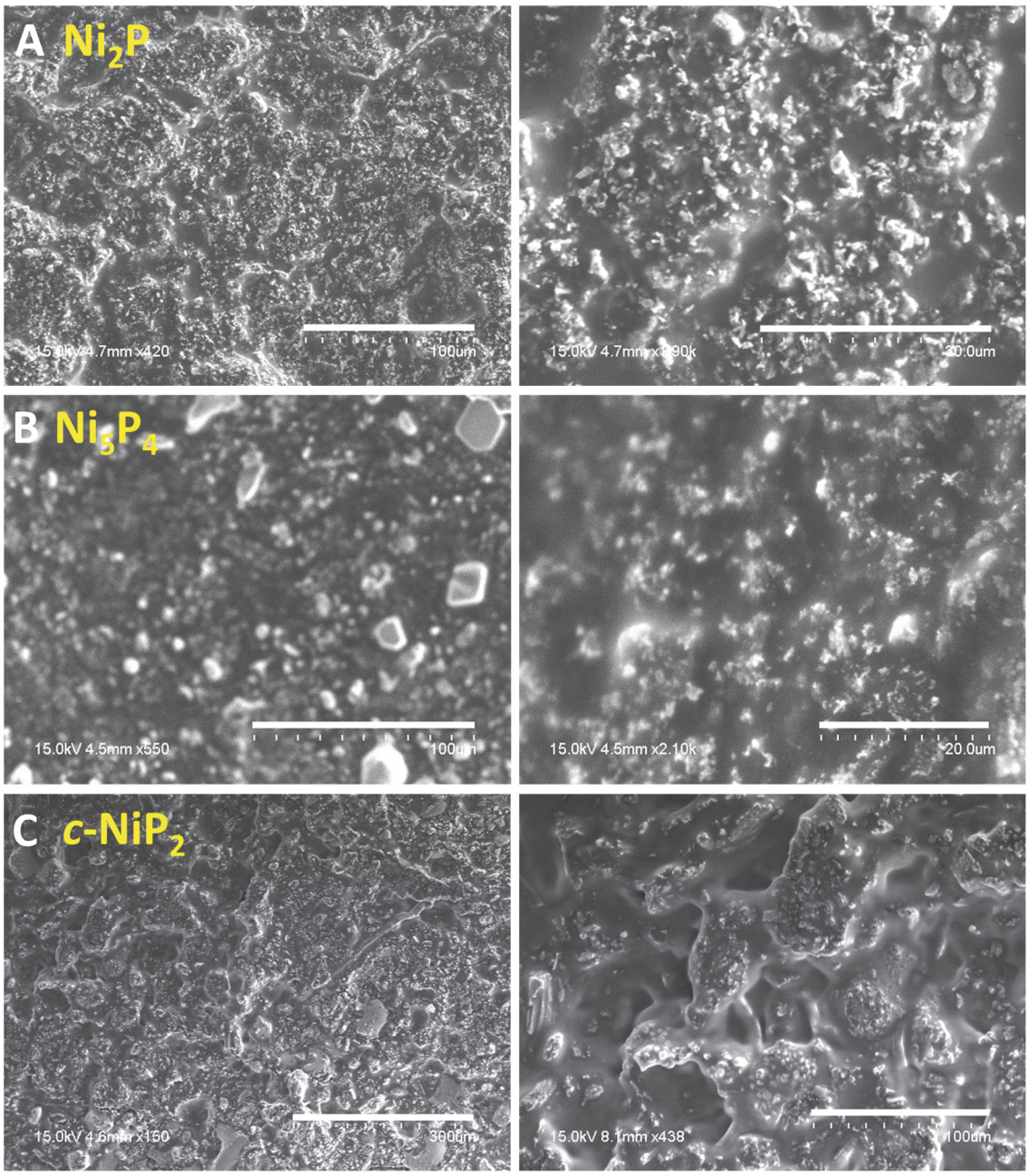

Figure S27. Scanning electron microscopy (SEM) images of nickel phosphide materials from direct reactions (A) Ni_2P (B) Ni_5P_4 (C) *c*-NiP_2 embedded on C_{wax} tips after 18-hour constant potential chronoamperometry (CA) HER experiments. The left and right columns show images at low and high magnifications respectively. The lengths of scale bars (left, right) are (A) 100 µm, 20 µm (B) 100 µm, 20 µm (C) 300 µm, 100 µm respectively.

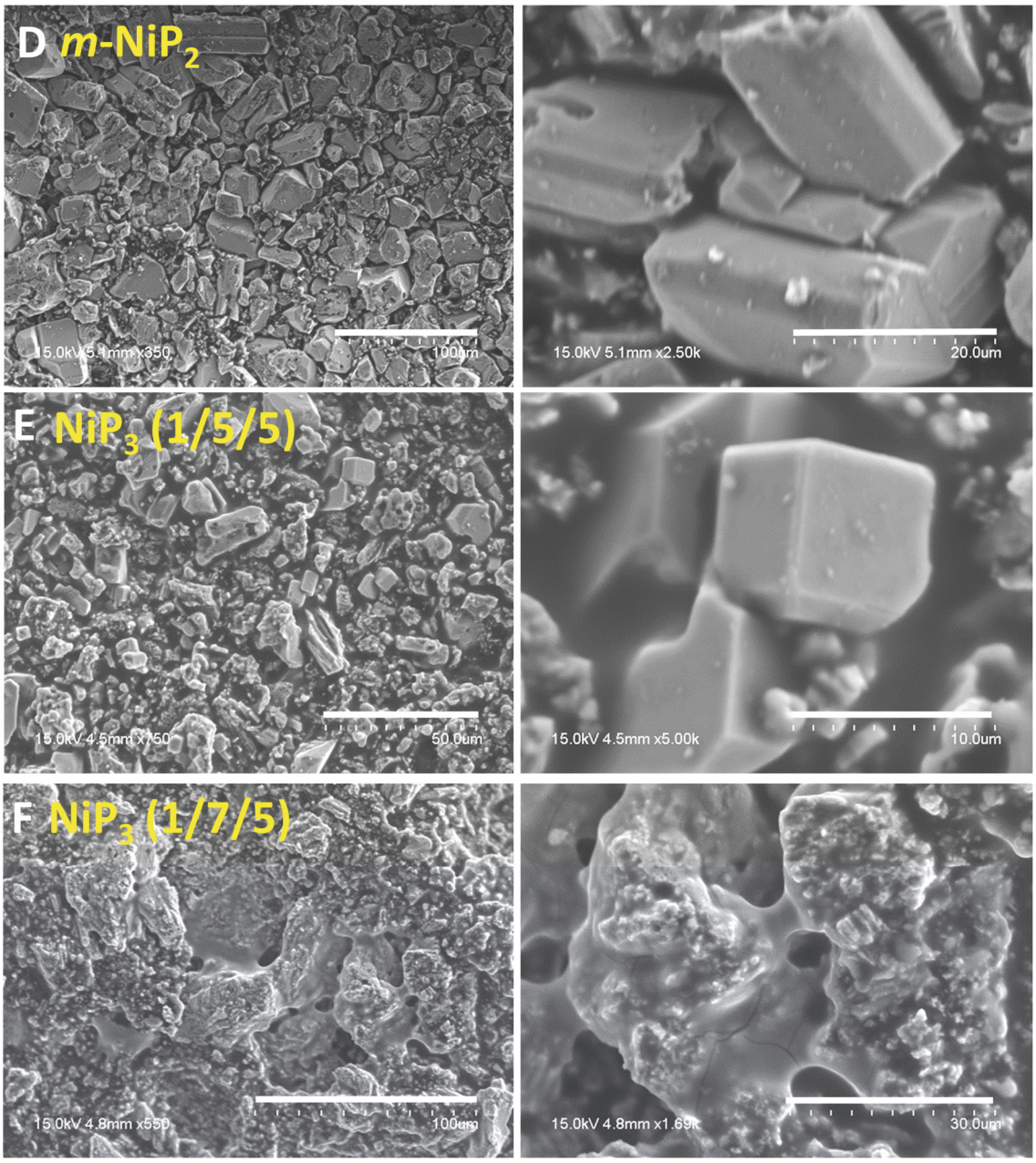

Figure S28. Scanning electron microscopy (SEM) images of nickel phosphide materials from tin-flux assisted reactions (D) *m*-NiP_2 and (E) NiP_3 (1/5/5) and (F) NiP_3 (1/7/5) embedded on C_{wax} tips after 18-hour constant potential chronoamperometry (CA) HER experiments. The left and right columns show images at low and high magnifications respectively. The lengths of scale bars (left, right) are (D) 100 µm, 20 µm (E) 50 µm, 10 µm (F) 100 µm, 30 µm respectively.

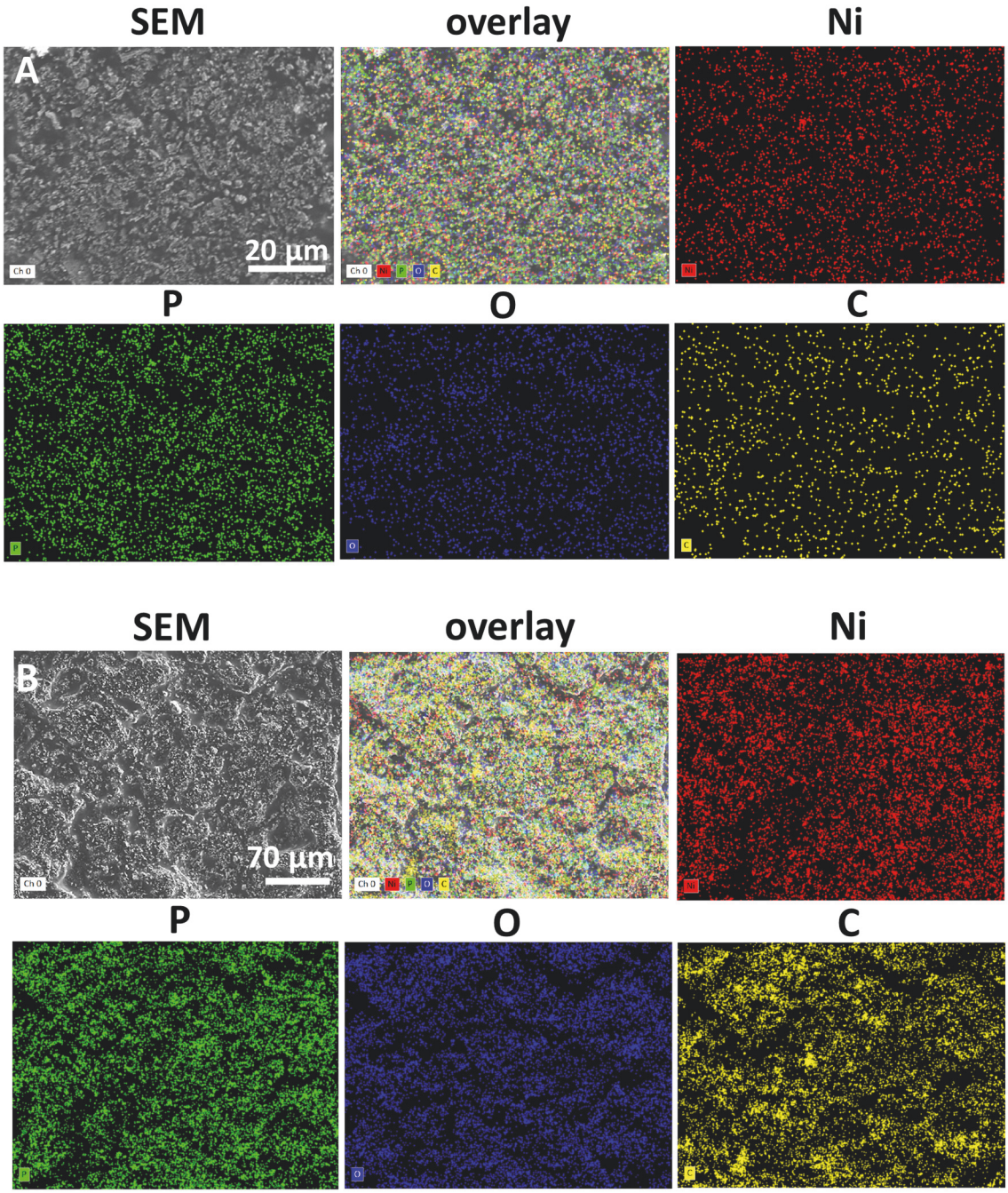

Figure S29. Elemental EDS map images of Ni_2P embedded on C_{wax} (A) before and (B) after 18-hour constant potential chronoamperometry (CA) HER experiments.

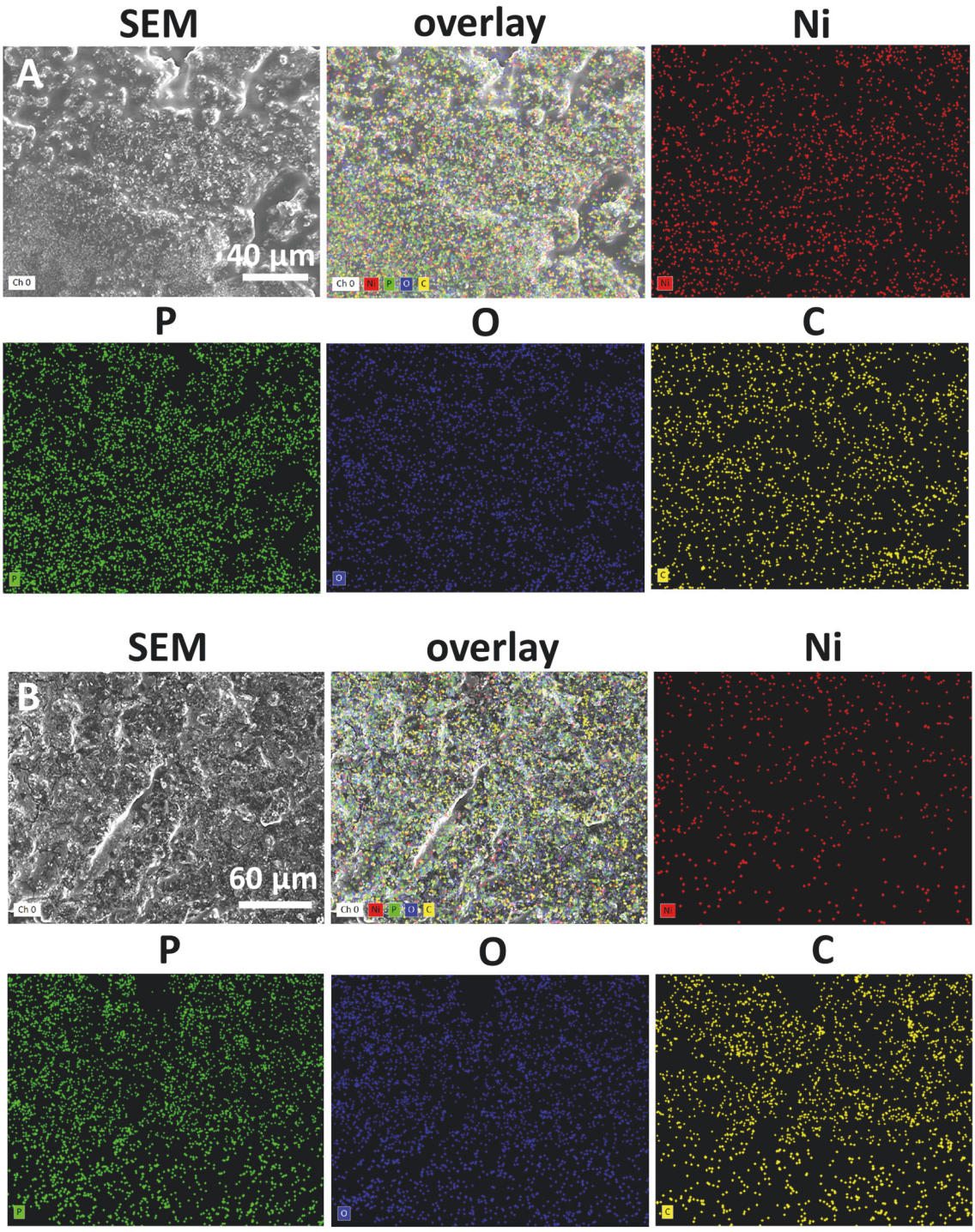

Figure S30. Elemental EDS map images of Ni_5P_4 embedded on C_{wax} (A) before and (B) after 18-hour constant potential chronoamperometry (CA) HER experiments.

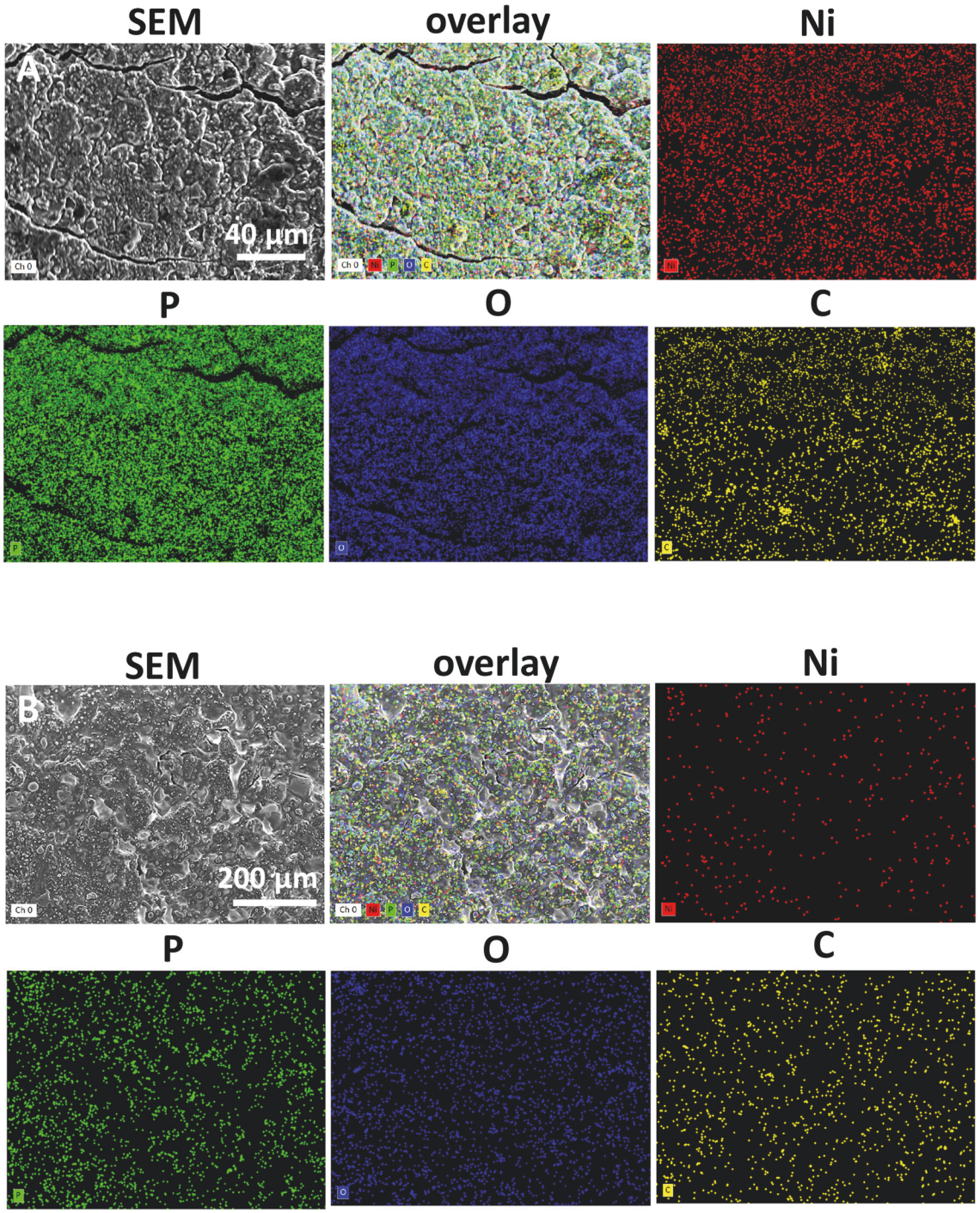

Figure S31. Elemental EDS map images of *c*-NiP_2 embedded on C_{wax} (A) before and (B) after 18-hour constant potential chronoamperometry (CA) HER experiments.

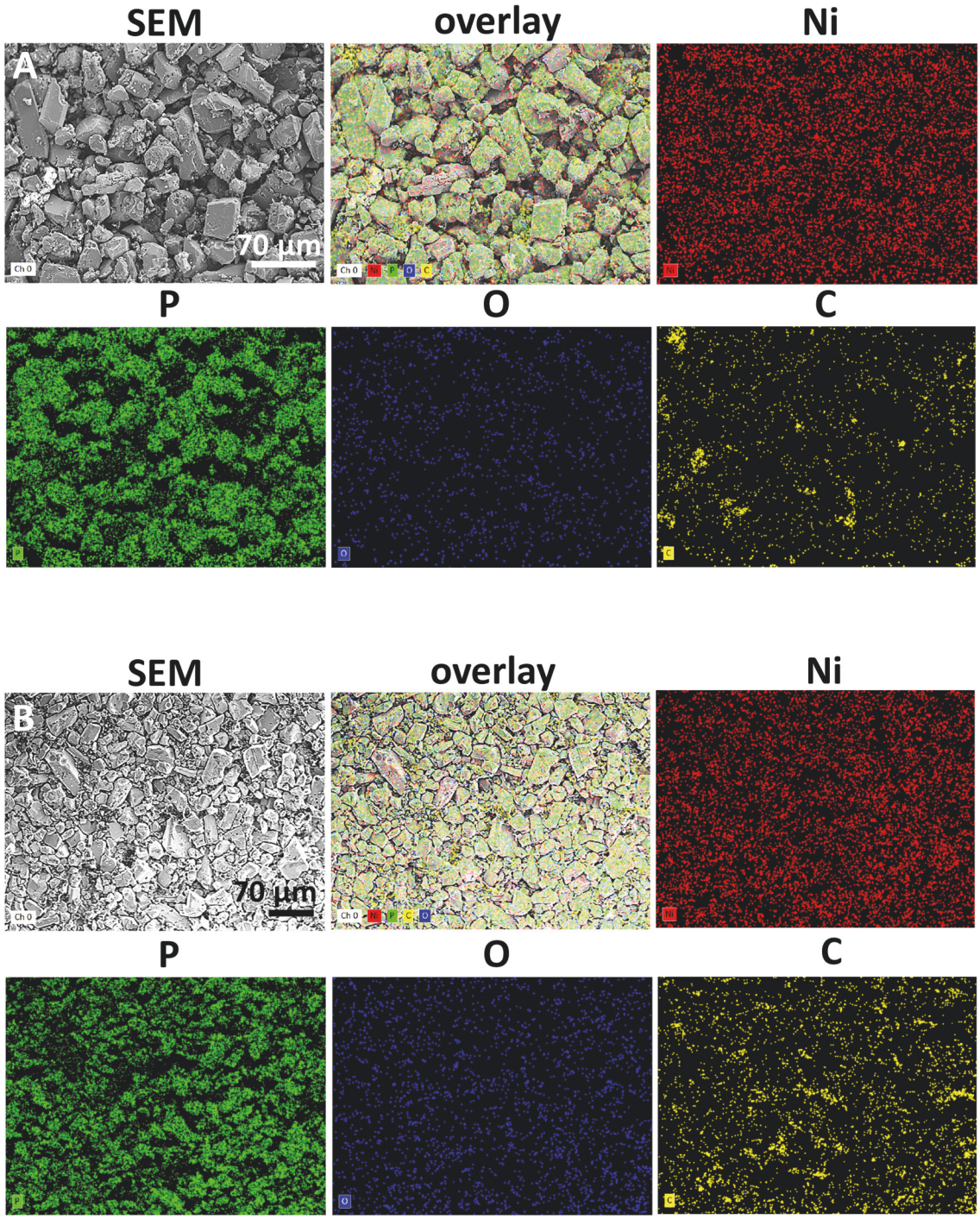

Figure S32. Elemental EDS map images of *m*-NiP_2 embedded on C_{wax} (A) before and (B) after 18-hour constant potential chronoamperometry (CA) HER experiments.

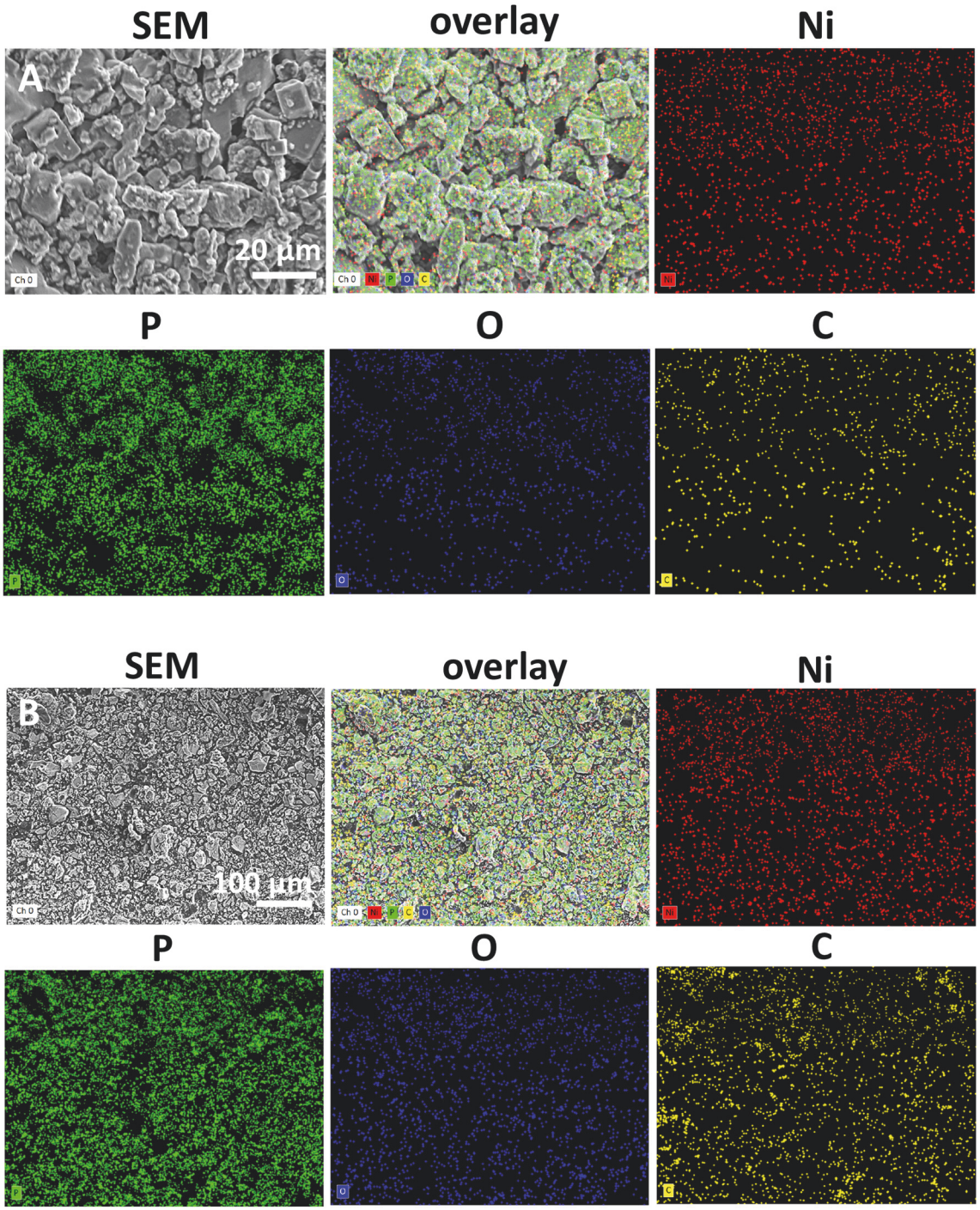

Figure S33. Elemental EDS map images of NiP_3 (1/5/5) embedded on C_{wax} (A) before and (B) after 18-hour constant potential chronoamperometry (CA) HER experiments.

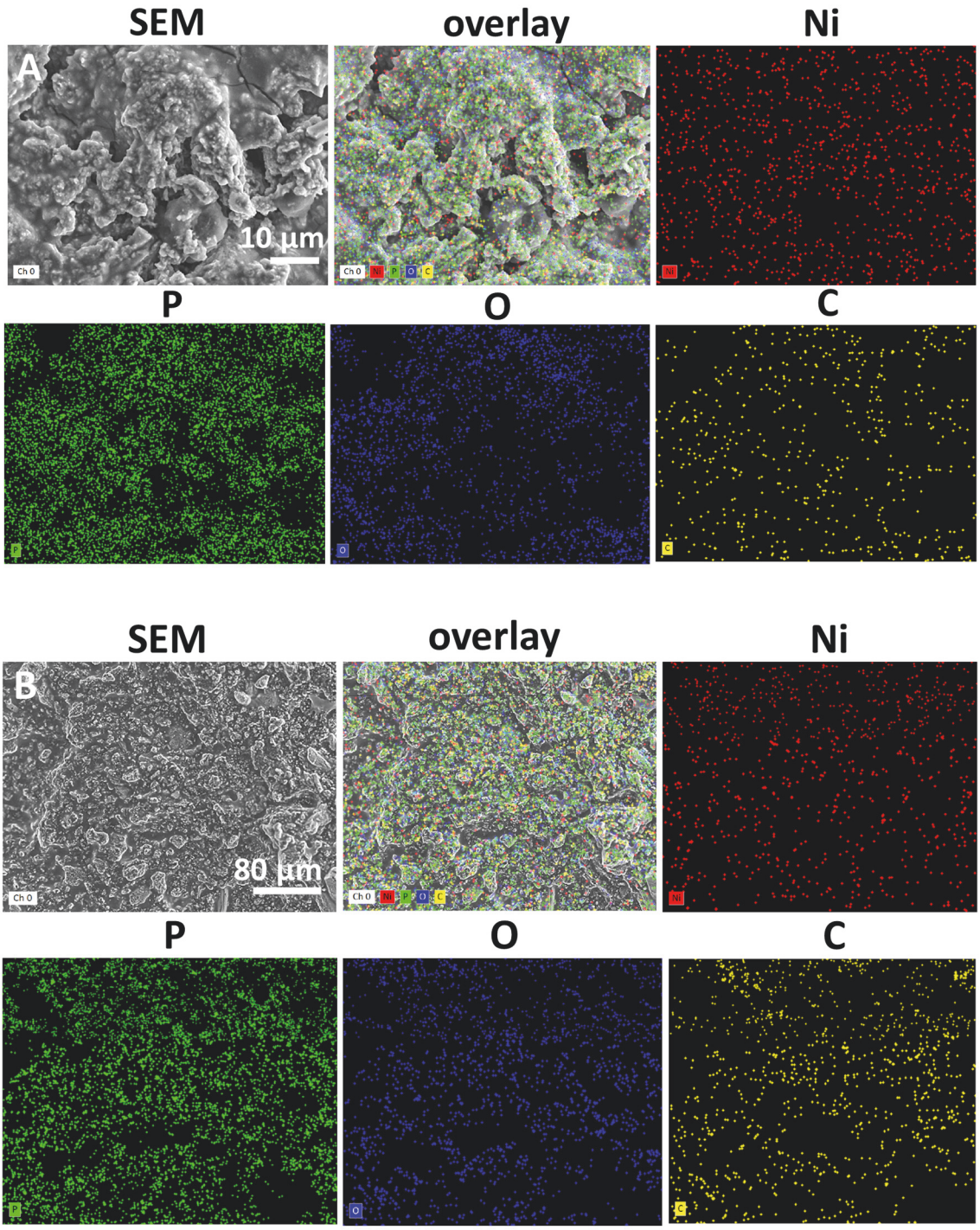

Figure S34. Elemental EDS map images of NiP_3 (1/7/5) embedded on C_{wax} (A) before and (B) after 18-hour constant potential chronoamperometry (CA) HER experiments.

Table S6. Summary of compositional EDS analysis of nickel phosphide materials embedded on C_{wax} tips after 18-hour constant potential chronoamperometry (CA) HER experiments. No detectable Sn signals or peaks were observed in EDS elemental maps or EDS analysis of both prior and post electrochemistry tips for tin-flux grown nickel phosphides (*m*-NiP_2, NiP_3).

Nickel phosphide	Ni (at%)	P (at%)	O (at%)	C (at%)	Atomic ratio of Ni: P: O
Ni_2P	7.8	3.2	15.7	73.3	1: 0.4: 2.0
Ni_5P_4	2.6	4.2	13.1	80.1	1: 1.6: 5.0
c-NiP_2	2.8	5.1	15.6	76.6	1: 1.8: 5.6
m-NiP_2	8.5	10.2	33.4	47.3	1:1.2: 3.9
NiP_3 (1/5/5)	5.0	10.8	31.8	52.4	1: 2.2: 6.4
NiP_3 (1/7/5)	5.0	10.6	31.4	53.1	1: 2.1: 6.3

REFERENCES

(1) Binnewies, M.; Milke, E. *Thermochemical Data of Elements and Compounds, Data Section N,* Weinheim, New York, p 700-743; **1999**. DOI: 10.1002/9783527619818.ch5m.
(2) *https://materialsproject.org/materials/mp-1920/*. (accessed 11/08/2022).
(3) *https://materialsproject.org/materials/mp-22619/*. (accessed 11/08/2022).
(4) Kühn, G.; Kubaschewski, O.; Alcock, C. B. *Metallurgical Thermochemistry. 5th ed. International Series on Materials Science and Technology, Vol. 24,* Pergamon Press Oxford, New York; **1979**. DOI: 10.1002/crat.19800150208.
(5) Naumkin, A. V. Kraut-Vass., A.; Gaarenstroom, S. W.; Powell, C. J. NIST X-ray Photoelectron Spectroscopy Database https://srdata.nist.gov/xps/Default.aspx (Date accessed: 06/10/2022). **2012**; Vol. Vol 20, Version 4.1.
(6) Owens-Baird, B.; Xu, J. Y.; Petrovykh, D. Y.; Bondarchuk, O.; Ziouani, Y.; Gonzalez-Ballesteros, N.; Yox, P.; Sapountzi, F. M.; Niemantsverdriet, H.; Kolen'ko, Y. V.; Kovnir, K. NiP2: A Story of Two Divergent Polymorphic Multifunctional Materials. *Mater. Chem.* **2019**, *31* (9), 3407-3418. DOI: 10.1021/acs.chemmater.9b00565.
(7) Ihsan-Ul-Haq, M.; Huang, H.; Cui, J.; Yao, S. S.; Wu, J. X.; Chong, W. G.; Huang, B. L.; Kim, J. K. Chemical interactions between red P and functional groups in NiP3/CNT composite anodes for enhanced sodium storage. *J. Mater. Chem. A* **2018**, *6* (41), 20184-20194, 10.1039/C8TA06841K. DOI: 10.1039/c8ta06841k.
(8) Tian, T.; Ai, L. H.; Jiang, J. Metal-organic framework-derived nickel phosphides as efficient electrocatalysts toward sustainable hydrogen generation from water splitting. *Rsc Adv* **2015**, *5* (14), 10290-10295. DOI: 10.1039/c4ra15680c.
(9) Kibsgaard, J.; Tsai, C.; Chan, K.; Benck, J. D.; Norskov, J. K.; Abild-Pedersen, F.; Jaramillo, T. F. Designing an improved transition metal phosphide catalyst for hydrogen evolution using experimental and theoretical trends. *Energy Environ. Sci.* **2015**, *8* (10), 3022-3029. DOI: 10.1039/c5ee02179k.
(10) Popczun, E. J.; McKone, J. R.; Read, C. G.; Biacchi, A. J.; Wiltrout, A. M.; Lewis, N. S.; Schaak, R. E. Nanostructured nickel phosphide as an electrocatalyst for the hydrogen evolution reaction. *J. Am. Chem. Soc.* **2013**, *135* (25), 9267-9270. DOI: 10.1021/ja403440e.

(11) Feng, L.; Vrubel, H.; Bensimon, M.; Hu, X. Easily-prepared dinickel phosphide (Ni2P) nanoparticles as an efficient and robust electrocatalyst for hydrogen evolution. *Phys. Chem. Chem. Phys.* **2014**, *16* (13), 5917-5921. DOI: 10.1039/c4cp00482e.
(12) Pan, Y.; Liu, Y. R.; Zhao, J. C.; Yang, K.; Liang, J. L.; Liu, D. D.; Hu, W. H.; Liu, D. P.; Liu, Y. Q.; Liu, C. G. Monodispersed nickel phosphide nanocrystals with different phases: synthesis, characterization and electrocatalytic properties for hydrogen evolution. *J. Mater. Chem. A* **2015**, *3* (4), 1656-1665. DOI: 10.1039/c4ta04867a.
(13) Zhou, Z.; Wei, L.; Wang, Y. Q.; Karahan, H. E.; Chen, Z. B.; Lei, Y. J.; Chen, X. C.; Zhai, S. L.; Liao, X. Z.; Chen, Y. Hydrogen evolution reaction activity of nickel phosphide is highly sensitive to electrolyte pH. *J. Mater. Chem. A* **2017**, *5* (38), 20390-20397. DOI: 10.1039/c7ta06000a.
(14) Zheng, H.; Huang, X.; Wu, Z.; Gao, H.; Dong, W.; Wang, G. Controlled Synthesis of 3D Flower-like Ni(2) P Composed of Mesoporous Nanoplates for Overall Water Splitting. *Chem. Asian J.* **2017**, *12* (22), 2956-2961. DOI: 10.1002/asia.201701255.
(15) Pan, Y.; Lin, Y.; Liu, Y. Q.; Liu, C. G. Size-dependent magnetic and electrocatalytic properties of nickel phosphide nanoparticles. *Appl. Surf. Sci.* **2016**, *366*, 439-447. DOI: 10.1016/j.apsusc.2016.01.143.
(16) Pan, Y.; Hu, W. H.; Liu, D. P.; Liu, Y. Q.; Liu, C. G. Carbon nanotubes decorated with nickel phosphide nanoparticles as efficient nanohybrid electrocatalysts for the hydrogen evolution reaction. *Mater. Chem. A* **2015**, *3* (24), 13087-13094. DOI: 10.1039/c5ta02128f.
(17) Kim, J. Y.; Park, H.; Joo, W.; Nam, D. H.; Lee, S.; Kim, H. G.; Ahn, I. K.; Kang, H. Y.; Lee, G. B.; Jung, I. H.; Kim, M. Y.; Lee, G. D.; Joo, Y. C. Predictive fabrication of Ni phosphide embedded in carbon nanofibers as active and stable electrocatalysts. *J. Mater. Chem. A* **2019**, *7* (13), 7451-7458. DOI: 10.1039/c9ta00455f.
(18) Jiang, P.; Liu, Q.; Sun, X. NiP2 nanosheet arrays supported on carbon cloth: an efficient 3D hydrogen evolution cathode in both acidic and alkaline solutions. *Nanoscale* **2014**, *6* (22), 13440-13445. DOI: 10.1039/c4nr04866k.
(19) Ledendecker, M.; Krick Calderon, S.; Papp, C.; Steinruck, H. P.; Antonietti, M.; Shalom, M. The synthesis of nanostructured Ni5 P4 films and their use as a non-noble bifunctional electrocatalyst for full water splitting. *Angew. Chem. Int. Ed.* **2015**, *54* (42), 12361-12365. DOI: 10.1002/anie.201502438.
(20) Owens-Baird, B.; Sousa, J. P. S.; Ziouani, Y.; Petrovykh, D. Y.; Zarkevich, N. A.; Johnson, D. D.; Kolen'ko, Y. V.; Kovnir, K. Crystallographic facet selective HER catalysis: exemplified in FeP and NiP2 single crystals. *Chem. Sci.* **2020**, *11* (19), 5007-5016. DOI: 10.1039/d0sc00676a.